July 2021

Thermoelectric Transport In Disordered Organic and Inorganic Semiconductors

Meenakshi Upadhyaya
University of Massachusetts Amherst

Thermoelectric Transport In Disordered Organic and Inorganic Semiconductors

Meenakshi Upadhyaya

THERMOELECTRIC TRANSPORT IN DISORDERED ORGANIC AND INORGANIC SEMICONDUCTORS

A Dissertation Presented

by

MEENAKSHI UPADHYAYA

Submitted to the Graduate School of the
University of Massachusetts Amherst in partial fulfillment
of the requirements for the degree of

DOCTOR OF PHILOSOPHY

May 2021

Electrical and Computer Engineering

THERMOELECTRIC TRANSPORT IN DISORDERED ORGANIC AND INORGANIC SEMICONDUCTORS

A Dissertation Presented

by

MEENAKSHI UPADHYAYA

Approved as to style and content by:

Zlatan Aksamija, Chair

Dhandapani Venkataraman, Member

Neal Anderson, Member

Christopher V. Hollot, Department Head
Electrical and Computer Engineering

DEDICATION

To my dad, whose support and encouragement made this possible. I wish he could have seen it through its completion.

ACKNOWLEDGMENTS

I would like to thank my doctoral advisor, Prof. Zlatan Aksamija for his constant guidance, insights and feedback that has helped me grow as a researcher and providing me with opportunities for professional and personal growth. The one thing that I am constantly reminded of is his enthusiasm to try new avenues which kept me motivated and energized even at low points when things were not going as expected. His depth of knowledge, passion for research, commitment to his work and students has been truly inspirational for me. I will be forever grateful for his support and understanding during difficult times and while I dealt with personal loss.

I want to extend my sincere gratitude to Prof. Dhandapani Venkataraman and Prof. Neal Anderson for serving on my committee and the valuable suggestions to improve my dissertation.

I am grateful to have had a very fruitful collaboration with Prof. Dhandapani Venkataraman and his graduate students, Connor Boyle and Michael Lu-Díaz in the Chemistry department. I would like to thank them for the many enriching discussions and for performing the experiments and contributing data for this dissertation. I am thankful to all the members of NanoEnergy and Thermophysics lab for the insightful discussions on research and my graduate course work, and all the helpful suggestions to improve my technical presentations.

I want to thank my mother and my spouse, Suhas Srinivasan for their enduring love and support, without which this would not have been possible, and a special thanks to my cousins and friends for always being there for me. I am thankful for all the growth opportunities and connections I made being a part of Graduate women

in STEM and College of Engineering Diversity Programs, and am grateful for the solidarity and support from the ECE PhD Women's group.

ABSTRACT

THERMOELECTRIC TRANSPORT IN DISORDERED ORGANIC AND INORGANIC SEMICONDUCTORS

MAY 2021

MEENAKSHI UPADHYAYA

B.E, VISVESVARAYA TECHNOLOGICAL UNIVERSITY

M.TECH, VELLORE INSTITUTE OF TECHNOLOGY

Ph.D., UNIVERSITY OF MASSACHUSETTS AMHERST

Directed by: Professor Zlatan Aksamija

The need for alternative energy sources driven by the escalating energy crisis has led to extensive research on optimizing the conversion efficiency of thermoelectric (TE) materials. TE efficiency is governed by the figure-of-merit (ZT) and it has been an enormously challenging task to increase ZT$>$ 1 with bulk materials, despite decades of research due to the interdependence of material properties. Most doped inorganic semiconductors have a high electrical conductivity and a moderate Seebeck coefficient, but ZT is still limited by their high lattice thermal conductivity. One approach to address this problem is to decrease the thermal conductivity by means of alloying and nanostructuring. Another approach is to consider materials with an inherently low thermal conductivity on account of their disordered structure such as polymers, and optimize their power factor through doping. In the first part of this dissertation, thermal transport in nanostructures of silicon-based Group-IV alloys is studied by employing the phonon Boltzmann transport equation formalism

with full phonon dispersion and a partially diffuse momentum-dependent specularity model for boundary roughness scattering. The results show thermal conductivity in Si-Ge nanostructures including thin films, superlattices (SLs), nanowires (NWs), and nanocomposites (NCs) to be well below their bulk counterparts, almost reaching the amorphous limit. Thermal transport in nanostructures is tunable by extrinsic boundary effects such as sample size in thin films, period thickness in SLs, length/diameter in NWs, and grain size in NCs. Additionally, boundary/interface properties, such as roughness, orientation, and composition, also play a significant role in thermal transport and offer additional degrees of freedom to control the thermal conductivity.

The latter part of the dissertation examines the effects of disorder on the TE properties of semiconducting polymers based on the Gaussian disorder model for site energies, while employing the Pauli's master equation approach to model hopping between localized sites. The effect of various manifestations of disorder, including positional disorder, energetic disorder, as well as correlation in both energy and wavefunction overlap distributions, on the electrical conductivity, Seebeck coefficient and Lorenz number is studied. Disorder leads to inherently different transport, and minimizing energetic disorder and correlation while increasing positional disorder results in a higher TE power factor.

Conjugated polymers need to be doped to increase charge carrier density and reach the electrical conductivity necessary for electronic and energy applications. While doping increases carrier density, Coulomb interactions between the dopant molecules and localized carriers, causes broadening and a heavy tail in the electronic density of states (DOS). It is shown that the width and shape of the DOS dictated to a large extent by the distribution of dopants, governs the trade-off relationship between electrical conductivity and Seebeck coefficient; a homogenous distribution of dopants leads to a narrow gaussian DOS and improved charge transport while a heterogenous distribution of dopants leads to a wide heave-tailed DOS with increased

energetic disorder. The long-range Coulomb interaction is much more pronounced in polymers than in inorganic semiconductors because of their low dielectric permittivity. It is shown that the dopant induced energetic disorder can be overcome by increasing the size of the dopants and the dielectric permittivity, improving charge screening and transport, resulting in a simultaneous increases in conductivity and the Seebeck coefficient. Doping is also more effective at higher dielectric permittivity as carriers contribute more readily to transport in the absence of the deep Coulombic tail of the DOS and reaching the peak power factor requires less doping.

TABLE OF CONTENTS

LIST OF FIGURES

Figure **Page**

CHAPTER 1

INTRODUCTION

1.1 Thermoelectrics: Background and Theory

The global need for sustainable energy sources has led to extensive research on more cost-effective and energy-efficient thermoelectric (TE) materials. TE devices can generate electricity from the application of a temperature gradient, or vice versa, through the Seebeck and Peltier effects. Most of the energy we use begins and ends as heat, with more than 60 quads being lost to the environment annually in the US alone [115]. TEs hold the key to efficient harvestation of thermal energy from waste heat in industrial processes and engines, to solar energy from parts of the solar spectrum which cannot be efficiently captured by photovoltaics. TE generators are solid-state devices with no moving parts, and they are silent, reliable, and scalable. Si-based thermoelectrics offer ease of integration with existing microelectronics, opening up the possibility for on-chip cooling and improved thermal management in ultra-scaled CMOS circuits [36, 144, 156]. However, their modest efficiency and relatively high cost have hampered their widespread adoption. Organic semiconductor based TEs offer advantages such as low cost due to inexpensive fabrication methods and large-area production, solubility in common solvents, and solution processing [153]. They are also potentially disposable and have lower potential for negative environmental impact [116], which makes them a very attractive choice for commercially viable TE applications [40, 66, 46]. However, both waste heat recovery and on-chip cooling require materials with high TE conversion efficiency in order to be competitive with

other technologies. TE conversion efficiency is given by the ratio between heat absorbed over the energy produced

$$\eta = \left(1 - \frac{T_C}{T_H}\right)\left(\frac{\sqrt{Z\bar{T}+1}-1}{\sqrt{Z\bar{T}+1}+\frac{T_C}{T_H}}\right), \tag{1.1}$$

where T_H and T_C are the absolute temperatures of the hot and cold sides of the system between which the temperature gradient is applied and the resulting heat flux is maintained while $\bar{T}$ is the average temperature inside the TE device.

Conversion efficiency is governed by the dimensionless figure-of-merit ZT, whereas, the maximum value achievable is determined by the Carnot limit. It is important to note that in Eq. 1.1 a small $T_H - T_C$ results in lower conversion efficiency, but only requires a small ZT to reach the maximum, whereas, a large $T_H - T_C$ results in higher efficiency, but at the expense of needing a larger ZT as shown in Fig. 1.1.

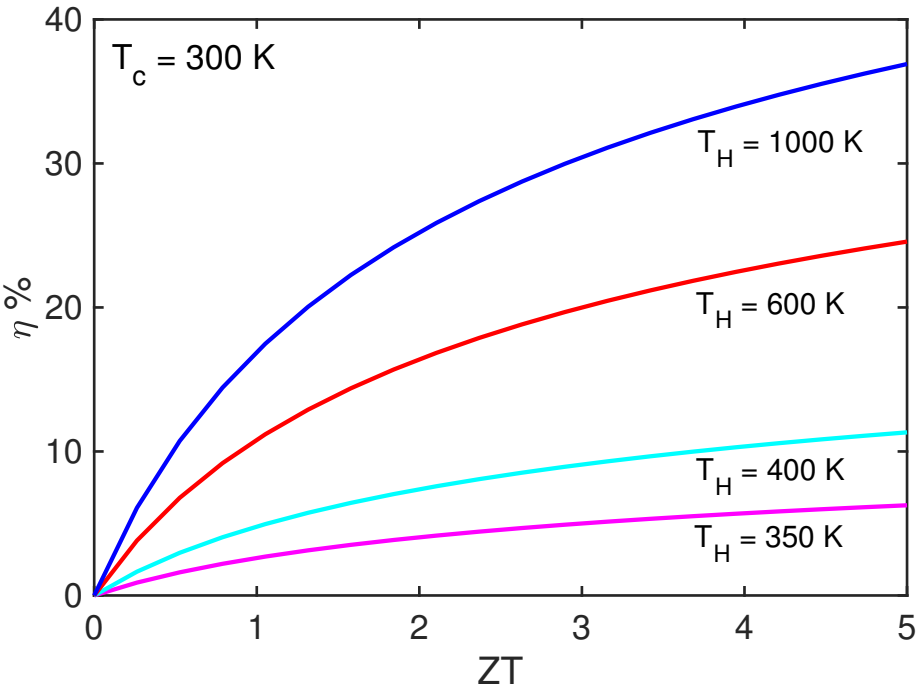

Figure 1.1. TE conversion efficiency η as a function of ZT with T_C=300 K and T_H=350, 400, 600, and 1000 K. As T_H increases, so does the Carnot limit, requiring a larger ZT to reach it.

ZT is given by,

$$ZT = \frac{\alpha^2 \sigma T}{\kappa} = \frac{\alpha^2}{L} \frac{\kappa_e}{\kappa_e + \kappa_l} \tag{1.2}$$

where α is the Seebeck coefficient, σ is the electrical conductivity, T is the absolute temperature, and $\kappa = \kappa_l + \kappa_e$ is the total thermal conductivity composed of electronic (κ_e) and lattice contributions (κ_l). The electronic component of thermal conductivity is related to the electrical conductivity through the Wiedemann-Franz law $\kappa_e = L\sigma T$ [54], where L is the Lorenz number.

1.2 Silicon based thermoelectrics

Most doped inorganic semiconductors have a high σ and a moderate Seebeck coefficient (α), but ZT is still limited by their high lattice thermal conductivity, which is mainly due to the lattice contribution from phonons, κ_{ph}. The lattice contribution typically dominates over that of the charge carriers, electrons or holes, κ_e, and provides the one independent property which can be tuned, at least to some extent, without adversely affecting the power factor ($\alpha^2\sigma$). Si in its bulk form has a thermal conductivity of 146 $\mathrm{Wm^{-1}K^{-1}}$ [61, 128] at room temperature and this limits the ZT to about 0.05 [107], almost two orders of magnitude below the value of ZT=3, which is considered desirable for solid-state TE devices to replace the conventional methods of cooling and power generation [122]. However, a more modest ZT of $1.5 - 2$ may suffice for kW-range applications such as vehicle heat recovery, car cooling/heating, and home co-generation [190].

It has been an enormously challenging task to increase ZT$>$ 1 with bulk materials despite decades of research due to the interdependence of material properties. Alloying is one approach that has been successful in improving the TE conversion efficiency of many bulk materials, including Si [17], where alloys of Si and Ge with varying composition have been typically used for TE conversion at high temperatures having ZT$>$ 1 around 900 K [166]. The improvement in ZT of bulk alloys comes pri-

marily from the order-of-magnitude reduction in the lattice thermal conductivity κ_{ph} caused by the dramatic increase in phonon scattering from the random mass variation present in the alloy. Semiconductor alloys often make good thermoelectrics because they closely resemble the phonon glass electron crystal (PGEC) concept [1]: they retain an ordered crystal structure but introduce disorder through mass variation. Mass disorder dramatically reduces lattice thermal transport while affecting electrons to a much lesser degree. However, the lattice thermal conductivity in $Si_{1-x}Ge_x$ alloys reaches a broad plateau for concentrations $0.2 < x < 0.8$ [128], limiting the amount of reduction in lattice thermal conductivity which can be achieved through alloying alone. This can be overcome by combining the effect of alloying with the use of low-dimensional nanostructures. The approach to maximizing ZT by utilizing low-dimensional nanostructures was first proposed theoretically by Hicks and Dresselhaus [68, 67, 45], which has led the way to numerous studies on $Si_{1-x}Ge_x$ alloy nanostructures, such as SiGe thin films [31], $Si/Si_{1-x}Ge_x$ superlattices [100, 99, 113, 8, 184], nanowires [86, 195, 98, 71, 181] and nanocomposites [78, 193, 5]. Reducing physical size of the conductor below some threshold, typically given by the phonon mean free path (MFP) in the bulk material, is expected to bring about a two-fold benefit: first is a significant decrease in the thermal conductivity resulting in an improvement of TE conversion efficiency [78, 135, 214]. The second is the increase in the electronic Seebeck coefficient and the resulting power factor (PF) due to the reduction in the dimensionality. However, there is still much speculation over the effect of quantum confinement on electrons and its effect on the PF as the physical thickness required to achieve sufficient confinement dips below 10 nm [156]. Nonetheless, reducing lattice thermal conductivity without significantly affecting the Seebeck coefficient or electrical conductivity can still dramatically increase the overall ZT so thermal conductivity engineering through nanostructuring should be pursued in its own right as a viable path toward improving TE conversion efficiency.

1.3 Polymers as thermoelectric materials

Another approach is to consider materials with an inherently low thermal conductivity on account of their disordered structure such as polymers, and thus do not require further processing such as nanostructuring to reduce it. Thermal conductivity in π-conjugated polymers such as poly(3-hexylthiophene) (P3HT), polypyrrole (PPY), polycarbazoles, polythiophenes, polyaniline (PANI) and poly(3,4-ethylenedioxythiophene) (PEDOT) [126, 216, 103, 46] is at least an order of magnitude lower than inorganic compounds, with lattice thermal conductivity typically <1 $\mathrm{Wm^{-1}K^{-1}}$ [87, 116, 108]. Conjugated polymers are poor electronic conductors for two principal reasons: their morphology has a significant disorder, and they do not have intrinsic free charge carriers. Therefore, they need to be doped, i.e., oxidized or reduced, to increase the density of free carriers and thus improve their electrical conductivity [35, 87]. These free carriers in the oxidized or reduced polymer impart electronic and optoelectronic properties of conjugated polymers that form the basis of organic electronics.

A long-standing problem in TEs has been to effectively decouple electrical conductivity from the Seebeck coefficient and control them independently as doping polymers in order to improve the electrical conductivity has the undesirable effect of significantly reducing their Seebeck coefficient to a range in the order of tens of $\mu\mathrm{VK^{-1}}$ [170], resulting in a trade-off between Seebeck and conductivity. Hence, precise control of the amount of doping is critical for obtaining the maximum power factor, and further progress of polymer TEs will rely on altering the trade-off between Seebeck and conductivity. Nonetheless, doping polymer blends with a minor additive component has been shown to simultaneously increase the electrical conductivity and Seebeck coefficient [170]. Also, polymer-CNT composites and organic-inorganic composite materials have been shown to possess higher ZT values due to increased electrical conductivity of these materials [211, 126, 178]. Further improvements by mixing with graphite/graphene, carbon nanotubes, or inorganic TE nanoparticles have also been

observed [40]. Doping PEDOT with counter ions has shown to increase the TE efficiency up to two orders of magnitude depending on the counter-ion size [39]. Recently, PEDOT:Tos with enhanced Seebeck coefficient of 210 μV, electrical conductivity of 70 Scm^{-1} with a resulting ZT$\sim$0.25 [25] and PEDOT:PSS with a PF of 469 $\mu\mathrm{Wm}^{-1}\mathrm{K}^{-2}$ and ZT$\sim$0.42 [87] has been reported, making them a viable alternative to inorganic materials.

When one end of a TE is heated, the charge carriers transport heat and move away from the hot junction to the colder end creating a voltage difference. In reverse, when a voltage is applied, the charge carriers transport heat from the cold end to the hot end. Thus, the transport of charge carriers is central to the function of thermoelectric devices. Polymer systems do not possess the long-range order found in their inorganic counterparts; they are inherently disordered and charge transport can be described as a hopping process. The design of efficient polymer TEs requires consideration of disorder in addition to optimizing the doping concentration. Progress in raising their conversion efficiency has been sporadic and severely hampered by the complexity of their thin film structure and a lack of systematic guidelines for materials discovery and improvement. For all these reasons, optimizing the properties of conjugated polymers for any application becomes empirically multivariate and complex. Simulation is a powerful tool to understand transport in these materials and investigate the effect of disorder on the TE performance of these materials.

1.4 Outline

We consider TE transport in both inorganic crystalline and organic disordered semiconductors. First, we employ alloying and nanostructuring as a means to reduce the thermal conductivity and consider four types of nanostructures with progressively more complex geometrical shape. All the relevant intrinsic scattering mechanisms spanning 3-phonon anharmonic umklapp and normal, isotope, impurity, and alloy

mass-difference are included. We use the full phonon dispersion calculated from the adiabatic bond charge model and we describe roughness scattering at the boundaries of the nanostructures through a momentum-dependent specularity parameter. We focus on SiGe alloys as the underlying material and demonstrate ways to utilize nanostructuring with the goal of reducing the lattice thermal conductivity in order to improve the figure-of-merit and increase the overall TE conversion efficiency. We begin in Ch. 2 with SiGe alloy thin-films and superlattices, where diffuse interface scattering results in highly anisotropic thermal transport, with conductivity below that of a random alloy. It is shown that thermal conductivity can be further minimized by growing short-period $Si/Si_{1-x}Ge_x$ SLs with the SiGe layer thicker than the Si one.

In Ch. 3, we study length-dependent thermal transport in SiGe nanowires (NWs). Calculation of the lattice thermal conductivity is based on solving the pBTE using the Monte Carlo (MC) technique to sample phonon mean-free-paths in the Si-Ge NW in order to fully capture the interaction between the strong alloy scattering inside the wire and partially diffuse roughness scattering at its boundaries. We show that phonons exhibit a mix of rare micron-long free flights, interspersed with diffuse scattering due to alloy mass disorder and interactions with the rough boundaries. Collectively, this leads to a heavy tailed distribution of phonon mean-free-paths (MFPs), typically found in Lévy walks [20, 14]. This unique feature fundamentally changes transport in Si-Ge NWs and causes superdiffusion, which is evidenced by a sub-linear $\kappa(L) \propto L^{1/3}$ length scaling over a broad range of wire lengths (10 nm$< L <$10 μm) and a complete absence of a direct ballistic-to-diffusive transition. Similarly, we find the time evolution of mean-square energy displacement to be superlinear ($\sigma^2(t) \propto t^{\beta}$, with β=1.34), confirming superdiffusive transport of phonons in Si-Ge NWs. Finally, we turn our attention to the geometrically most challenging case, which is that of nanocomposites, where the heterogeneous and complex structure of the nanocomposite is modeled based on the Voronoi tesselation and the phonon Boltzmann equation.

We find that thermal conductivity decreases with average grain size, analogous to the thickness dependence in superlattices; we then proceed to study the impact of grain size distribution and length dependence of thermal conductivity of the composite material.

In Ch. 4 - 6 we investigate the TE properties of disordered organic semiconductors employing a modified hoping based Gaussian disorder model (GDM), and we use Pauli's master equation (PME) approach to calculate the site occupational probabilities. In Ch. 4 we explore the effect of various manifestations of disorder on the TE properties of organic semiconductors. We show that stronger overlap between sites can improve the electrical conductivity without adversely affecting the Seebeck coefficient. Positional disorder aids the formation of new conduction paths with an increased probability of carriers in high energy sites, leading to an increase in electrical conductivity. In contrast, energetic disorder leads to increased energy gap between sites hindering transport and adversely affects conductivity, however, the increased energy gap also leads to a lower average site energy and a small increase in Seebeck coefficient. Consequently, positional correlation negatively affects conductivity, while correlation in energy has no effect on TE properties of polymers. Our results also show that the Lorenz number increases with Seebeck coefficient, largely deviating from the Sommerfeld value, in contrast to band conductors. The design of efficient polymer TEs requires consideration of both positional and energetic disorder, as well as the Lorenz number, in addition to optimizing the doping concentration.

In Ch. 5 we show that while doping increases carrier density, it causes broadening and a heavy tail in the otherwise Gaussian density of states (DOS) due to Coulomb interactions between the dopant and the polymer which is further enhanced with dopant clustering. We use a modified Gaussian phonon-assisted hopping model to include the effect of dopant clustering and find that the width and shape of the DOS is controlled by the distribution of dopants and are both critical to the relation-

ship between electrical conductivity and Seebeck coefficient. We fit experimentally determined iodine-doped P3HT and PDPP4T to our simulations and find that the changing size and shape of the heavy-tailed DOS distribution brought on by doping dictates the slope of the Seebeck vs. conductivity tradeoff curve. We conclude that reducing the dopant-carrier Coulomb interactions and minimizing dopant clustering can have a beneficial impact on conductivity, hence, precise control of the amount of doping and distribution of dopants are both critical for obtaining the maximum PF.

The charge-charge Coulomb interactions between the dopant and the polymer is much more pronounced in polymers than in inorganic semiconductors because of their low dielectric permittivity. In Ch. 6 we show that raising the dielectric constant of a polymer counteracts the dopant-induced broadening of the DOS and results in a simultaneous increase in the Seebeck coefficient and electrical conductivity. We find that dopant-induced the energetic disorder closely follows the Coulomb interaction energy with the nearest dopant. At low doping the carrier mobility first decreases with doping, due to the trap states in the tail of the DOS being filled first, followed by rapidly increasing at high doping levels. We relate the dopant-induced energetic disorder to a reduction in the Seebeck coefficient while deep traps in the heavy tail cause a collapse in conductivity. Increasing the dielectric constant from 3 to 12 nearly restores the intrinsic DOS, resulting in a large increase in the power factor. We also show the impact of dopant size on Coulombic disorder and mobility. Our results indicate that doped polymer composites with high dielectric permittivity are a fertile new avenue to decrease Coulomb interactions, improve charge transport in conjugated polymers, and develop high performance organic electronic materials.

CHAPTER 2

LATTICE THERMAL CONDUCTIVITY IN SIGE NANOSTRUCTURES

SiGe alloys with varying composition have long been employed in TE energy conversion applications, such as NASA radio-isotope TE generators, and have ZT>1 around 900 K [166]. The improvement in ZT is primarily from the order-of-magnitude reduction in the lattice thermal conductivity κ_{ph} due to the mass-difference phonon scattering induced by alloying. However, the lattice thermal conductivity in $Si_{1-x}Ge_x$ alloys reaches a broad plateau between $0.2 < x < 0.8$ [128], which limits the lowest conductivity achievable through alloying. The mass-difference scattering that dominates lattice transport in the alloy depends on the difference in atomic mass between Si and Ge, and the average mass in the alloy given by $M_{Si}(1-x) + M_{Ge}x$. Initially, increasing the Ge concentration moves the average further from the Si mass, resulting in an increase in the scattering rate; however, increasing the Ge concentration past a certain point (around x=0.2) comes at the expense of moving it closer to the increasingly large fraction of Ge atoms in the alloy, resulting in a broad plateau in thermal conductivity vs. composition [8]. Hence, additional methods of reducing the lattice thermal conductivity are required. Within this plateau, nanostructuring results in stronger decrement of thermal conductivity (3 to 5 times lower than the bulk) than variation in Ge composition, while outside the plateau, compositional variation dominates. Lattice thermal conductivity in nanostructures is dominated by scattering from the rough boundaries or interfaces between layers, even at room temperature. Therefore, boundary/interface properties, such as roughness, orientation, and composition, are expected to play a significant role in thermal transport and they offer

additional degrees of freedom to control the thermal conductivity in semiconductor nanostructured alloys. The objective is to use nanostructuring and alloying methods which have been proposed to boost ZT in order to improve conversion efficiency of semiconductors while staying within the limits of what is achievable through experimental approaches and fabrication.

2.1 Phonon transport model

Most theories that simultaneously capture both electron and phonon transport in crystalline solids employ the Boltzmann transport equation (BTE). The BTE theory can explain a broad range of relevant effects in bulk or homogeneous materials, including the dependence of the electrical conductivity, the thermal conductivity, and the Seebeck coefficient on temperature, impurity content, isotope scattering, and quantum confinement [27] and can be complementary to other methods, such as Molecular Dynamics (MD). We focus herein on the lattice thermal conductivity via the transport of phonons; by solving the time-independent phonon Boltzmann transport equation (pBTE) in its relaxation-time-approximation (RTA) form, the steady state distribution function can be obtained, which is then used to determine lattice heat conductivity. In steady-state, the time independent pBTE is given as [30]

$$\vec{v}_{\mathrm{BTE},\vec{q}} \cdot \vec{\nabla} N_{\mathrm{b},\vec{q}}(x,y,z) = -\frac{N_{\mathrm{b},\vec{q}}(x,y,z) - N^{0}_{\mathrm{b},\vec{q}}(T)}{\tau^{int}_{\mathrm{b}}(\vec{q})}. \tag{2.1}$$

As indicated in the pBTE, the steady-state phonon distribution $N_{b,q}(x,y,z)$ is a function of the phonon branch b, wave vector $\vec{q}$ and position in 3D space (x,y,z). Here τ^{int}_{q} is the relaxation time due to all the intrinsic scattering mechanisms occuring in the interior of the material, including both resistive umklapp and non-resistive normal anharmonic phonon-phonon, isotope, impurity, and alloy mass difference interactions. τ^{int}_{q} can be obtained using the standard single-mode RTA from elasticity theory [138]

or from first principles, which typically leads to a quadratic [198] or cubic [48] frequency dependence of the anharmonic scattering rates in the long-wavelength limit. The equations hold for each branch, and inter-branch scattering is included in $\tau_{\mathrm{b}}^{int}(\vec{q})$. In the calculation of relaxation time $\tau_{\mathrm{b}}^{int}(\vec{q})$ for a phonon in branch b and with wave vector $\vec{q}$, we consider normal (N) and umklapp (U) three-phonon scattering, impurity (I, if present through doping or defects), and mass-disorder scattering (Mass) with branch and momentum dependent relaxation times $\tau_{\mathrm{b,N}}(\vec{q})$, $\tau_{\mathrm{b,U}}(\vec{q})$, $\tau_{\mathrm{b,I}}(\vec{q})$, and $\tau_{\mathrm{b,Mass}}(\vec{q})$ respectively. The total intrinsic relaxation time is given by

$$\frac{1}{\tau_{\mathrm{b}}^{int}(\vec{q})} = \frac{1}{\tau_{\mathrm{b,N}}(q)} + \frac{1}{\tau_{\mathrm{b,U}}(q)} + \frac{1}{\tau_{\mathrm{b,I}}(q)} + \frac{1}{\tau_{\mathrm{b,Mass}}(q)}. \tag{2.2}$$

When two materials are combined into an alloy, in this case $\mathrm{Si}_{1-x}\mathrm{Ge}_x$, variation in the local atomic mass leads to perturbations of lattice waves, which results in strong mass-difference scattering of phonons. In alloys, mass-disorder scattering will have three components: alloying, isotopic mass variation, and the small local strain field induced by variations in the atomic species (Si or Ge). The scattering strength will be proportional to the total fraction of mass-disordered constituents [30]

$$\Gamma_{\mathrm{Mass}}(x) = \Gamma_{\mathrm{Alloy}}(x) + \Gamma_{\mathrm{Iso}} + \Gamma_{\mathrm{Strain}}(x). \tag{2.3}$$

The alloy mass-difference constant is defined as [3]

$$\Gamma_{\mathrm{Alloy}} = \sum_i f_i (1 - M_i/\bar{M})^2, \tag{2.4}$$

where f_i is the proportion of material i with mass M_i, while the average mass is $\bar{M} = \sum_i f_i M_i$ [138]. The strength of the alloy mass-difference scattering has a quadratic dependence on the ratio between the masses of constituent atoms (M_i) and the average

alloy mass ($\bar{M}$) in Eq. 2.4. In the present case of $Si_{1-x}Ge_x$ alloys, the mass disorder depends on the Ge fraction.

$$\Gamma_{\text{Alloy}}(x) = x(1-x)\frac{(M_{\text{Ge}} - M_{\text{Si}})^2}{(xM_{\text{Ge}} + (1-x)M_{\text{Si}})^2}. \tag{2.5}$$

The primary driver of thermal conductivity reduction from pure Si or Ge to the SiGe alloy is the quadratic dependence on the Ge concentration in alloy mass-difference $\Gamma_{\text{Mass}}(x)$. The energy dependence of the alloy scattering rate follows a Rayleigh-like ($\tau^{-1} \propto \omega^4$) trend and is calculated from [171, 124]

$$\frac{1}{\tau_{\text{Mass}}(\omega)} = \frac{\pi}{6} V_0 \Gamma_{\text{Mass}} \omega^2 \, D(\omega), \tag{2.6}$$

where V_0 is the volume per atom and $D(\omega)$ is the vibrational density of states per unit volume [56]. The total energy dependent vibrational density of states is given by a sum over all phonon branches b

$$D(\omega) = \sum_{\text{b}} \int \frac{d\vec{q}}{(2\pi)^3} \delta\left[\omega - \omega_{\text{b}}(\vec{q})\right]. \tag{2.7}$$

The volume integral of the energy-conserving delta function over the whole first Brillouin zone (BZ) is calculated from the full phonon dispersion using the extrapolation method of Gilat and Raubenheimer [60]. In this method, the BZ is discretized and the area of the intersection between the constant-energy surface described by the delta function $\delta\left[\omega - \omega_{\text{b}}(\vec{q})\right]$ and each discretization cube is calculated. Then the areas are divided by the gradient of the dispersion and summed [59, 58].

The contribution due to isotopic variation in each of the constituent materials can be obtained by combining the isotope constants for each pure material as

$$\Gamma_{\text{Iso}}(x) = \frac{(1-x)\Gamma_{\text{Si}} M_{\text{Si}}^2 + x\Gamma_{\text{Ge}} M_{\text{Ge}}^2}{(xM_{\text{Ge}} + (1-x)M_{\text{Si}})^2}, \tag{2.8}$$

where the pure Si and Ge isotope scattering constants Γ_{Si} and Γ_{Ge} were taken from Ref. [138]. An additional component to alloy scattering arising from the strain field due to the difference in lattice constants of pure Si and Ge and their alloys has been proposed. The contribution due to strain is then given by [3]

$$\Gamma_{\mathrm{Strain}}(x) = \epsilon x(1-x)\frac{\left(a_{\mathrm{Ge}} - a_{\mathrm{Si}}\right)^2}{a_{\mathrm{SiGe}}^2(x)}, \tag{2.9}$$

where $a_{\mathrm{SiGe}}(x)$ is the composition-dependent alloy lattice constant, taken in the virtual crystal approximation, including bowing [151]. The empirical strain parameter is taken to be $\epsilon = 39$ [2]. It is estimated on the basis of the impurity model [91] and is in good agreement with experimental results for SiGe alloys. For most values of Ge concentration x, the strain contribution $\Gamma_{\mathrm{Strain}}(x)$ is found to be much smaller than the mass-difference component.

The resistive anharmonic phonon-phonon scattering rate was calculated for dielectric crystals as [138]

$$\tau_{\mathrm{b,U}}^{-1}(\vec{q}) = \frac{\hbar\gamma_{\mathrm{b}}^2}{\overline{M}\Theta_{\mathrm{b}}\bar{v}_{\mathrm{b}}^2}\omega_{\mathrm{b}}^2(\vec{q})Te^{-\Theta_{\mathrm{b}}/3T}, \tag{2.10}$$

where the speed of sound $\bar{v}_{\mathrm{b}}$ of each branch b is determined from the average slope of its dispersion curve near the Γ point, and $\overline{M}$ is the average atomic mass. The Grüneissen parameter γ_{b} was obtained for each branch from the phonon dispersion and has the value of 1.1 for the longitudinal acoustic branch and -0.6 for the two transverse acoustic branches. The expression in (2.10) contains the exponential term $e^{-\Theta_{\mathrm{b}}/3T}$ in the temperature dependence, which controls the onset of resistive umklapp scattering for each phonon branch through the branch-specific Debye temperatures Θ_λ, which were obtained from [165]

$$\Theta_{\mathrm{b}}^2 = \frac{5\hbar^2}{3k_B^2}\frac{\int \omega^2 D_{\mathrm{b}}(\omega)d\omega}{\int D_{\mathrm{b}}(\omega)d\omega}, \tag{2.11}$$

where the vibrational density of states (vDOS) $D_{\mathrm{b}}(\omega) = \sum_{\vec{q}} \delta\left[\omega - \omega_{\mathrm{b}}(\vec{q})\right]$ was calculated for each phonon branch b from the full dispersion, as described previously. This way, the temperature dependence of the contribution from each phonon branch to the total thermal conductivity is correctly represented.

In the bulk case, the crystal is assumed infinite and uniform. The distribution is only a function of temperature and in the absence of boundaries and interfaces, the solution of the pBTE equation is simply given by

$$n_{\vec{q}} = \tau_{int.}(\vec{q})\vec{v}_{\vec{q}} \cdot \nabla_{\vec{r}} T \frac{\partial N^0_{\vec{q}}(T)}{\partial T}. \tag{2.12}$$

In contrast, boundaries and interfaces play an important role in the solution of pBTE in nanostructures. Hence, in nanostructures, an extrinsic relaxation rate $\tau^{-1}_{\mathrm{b,B}}(\vec{q})$ due to boundary-roughness scattering is added. Each time a phonon reaches the boundary, the probability of it not being scattered by the roughness is captured through the momentum-dependent specularity parameter $0 < p(\vec{q}) < 1$ given by

$$p(\vec{q}) = \exp\left(-4\Delta^2 q^2 \cos^2\Theta\right), \tag{2.13}$$

with Δ being the rms boundary roughness (typically $0.1 < \Delta < 1$ nm, depending on sample quality and processing) and Θ being the angle between the direction of propagation of the phonon wave and the boundary normal. The specularity parameter allows us to capture both the magnitude and the angle dependence of the scattering and distinguish between the contribution to the heat flux from phonons travelling into the boundary (small Θ, hence smaller $p(\vec{q})$ and more scattering) and phonons travelling parallel to the boundary (large Θ and larger $p(\vec{q})$, leading to less scattering). The specularity parameter is used in solving the pBTE as a boundary condition, with $[1 - p(q)]$ giving the fraction of the incoming phonons which are scattered randomly.

As boundary scattering is a momentum-randomizing elastic process, the scattered phonons will carry zero heat flux, so they can be represented by the equilibrium Bose-Einstein distribution, leading to a boundary condition of the form

$$N_{\mathrm{b}}(\vec{q})^{+} = p(\vec{q})N_{\mathrm{b}}(\vec{q})^{-} + [1 - p(\vec{q})]\, N^{0}_{\mathrm{b},T}(\vec{q}). \tag{2.14}$$

with "+" and "-" representing the solution before reaching and after leaving the boundary, respectively, and $N_0(\vec{q})$ is the equilibrium Bose-Einstein phonon distribution of phonon mode $\vec{q}$ in branch b. The boundary scattering rate for a film of thickness H is then obtained as [8]

$$\tau^{-1}_{\mathrm{b,B}}(\vec{q}) = \frac{\upsilon_{\mathrm{b},\perp}(\vec{q})}{H} \frac{F_p(\vec{q},H)}{1 - \frac{\tau^{int}_{\mathrm{b}}(\vec{q})\upsilon_{\mathrm{b},\perp}(\vec{q})}{H} F_p(\vec{q},H)}, \tag{2.15}$$

where a mode-dependent scaling factor $F_p(\vec{q},H)$ is given by

$$F_p(\vec{q},H) = \frac{[1 - p(\vec{q})]\,\{1 - \exp[-H/\tau^{int}_{\mathrm{b}}(\vec{q})\upsilon_{\mathrm{b},\perp}(\vec{q})]\}}{1 - p(\vec{q})\exp[-H/\tau^{int}_{\mathrm{b}}(\vec{q})\upsilon_{\mathrm{b},\perp}(\vec{q})]}. \tag{2.16}$$

This formulation of interface scattering allows for the rates of internal (intrinsic) and boundary roughness scattering to be added together, despite their interdependence [180]. The factor given by Eq. (2.16) encapsulates the competition between boundary and internal scattering: the effective strength of boundary scattering will depend on the relative strength of the competing internal scattering mechanisms.

The full thermal conductivity tensor $\kappa^{\alpha\beta}$ is calculated as a sum over all phonon momenta and branches

$$\kappa^{\alpha\beta}(T) = \sum_{\mathrm{b}} \sum_{\vec{q}} \tau_{\mathrm{b}}(\vec{q}) C_{\mathrm{b}}\,(\vec{q},T)\, \upsilon^{\alpha}_{\mathrm{b}}(\vec{q})\upsilon^{\beta}_{\mathrm{b}}(\vec{q}), \tag{2.17}$$

where $\tau_{\mathrm{b}}(\vec{q})$ is the total phonon relaxation time, [for a bulk sample, $\tau_{\mathrm{b}}(\vec{q}) = \tau_{\mathrm{b,Internal}}(\vec{q})$ from Eq. (2.2)]. In the multi-layer SL structure, there is an additional contact

scattering term due to ballistic limits on the phonon mean free path imposed from the ends of the sample and given by $\tau_{\mathrm{b,C}}^{-1}(\vec{q}) = \upsilon_{\mathrm{b},\parallel}/L$ [12]. Phonons obey Bose-Einstein statics so their equilibrium distribution is given by the Bose-Einstein distribution function. The phonon heat capacity per mode $C_{\mathrm{b}}(\vec{q},T)$ is consequently given by

$$C_{\mathrm{b}}(\vec{q},T) = \frac{[\hbar\omega_{\mathrm{b}}(\vec{q})]^2}{k_B T^2} \frac{e^{(\hbar\omega_{\mathrm{b}}(\vec{q})/k_B T)}}{\left[e^{(\hbar\omega_{\mathrm{b}}(\vec{q})/k_B T)} - 1\right]^2}. \tag{2.18}$$

All the phonon branches have to be considered in the calculation of heat transport [92], although optical branches represent standing waves with very low group velocities and hence contribute comparatively little to the overall thermal transport relative to their acoustic counterparts. Despite this, in some nanostructures with strong boundary scattering, the contribution from the acoustic branches decreased to the point that the optical phonons, which do not scatter as often from boundaries due to their low group velocity, can make a non-negligible contribution [176].

The $\upsilon_{\mathrm{b}}^{\alpha,\beta}(\vec{q})$ are the components of phonon velocity vector calculated from the full phonon dispersion based on Weber's adiabatic bond charge (ABC) model [200]. The ABC model includes interactions between ions, bond charges, bond bending, and long-range electrostatic interactions, and has been shown to reproduce measured phonon vibrational frequencies in virtually all Group-IV [201, 155], III-V [169, 155], and II-VI [147] semiconductors with excellent accuracy. It has also recently been re-parametrized from first principles [38]. The ABC phonon dispersions for Si can be found in Refs. [6], and for Ge in Refs. [201, 155]. Vibrational properties of $Si_{1-x}Ge_x$ alloys, including phonon dispersion and velocity, are calculated in the virtual crystal approximation (VCA) [2], which has been shown to accurately capture the phonon modes of random alloys [97]. VCA is applied to Si_xGe_{1-x} by replacing the mass-disordered lattice by an ordered virtual crystal with randomly distributed atoms of constituent materials. The full phonon dispersion allows accurate treatment of the

inherent anisotropy which arises out of the combination of phonon focusing and the momentum-dependent boundary-roughness scattering.

2.2 Lattice thermal conductivity in SiGe alloy thin films

The calculated thermal conductivity of bulk and thin-films as a function of varying Ge composition is shown in Fig. 2.1(a). The strong quadratic dependence on germanium concentration dominates the variation in thermal conductivity. In addition, effect of nanostructuring in reducing thermal conductivity is observed in thin films. Our results are in agreement with experiemental data by Cheaito et al. [31]. In the composition range of $0.2 < x < 0.8$ thermal conductivity quickly decreases with increasing germanium composition and then it reaches an almost flat plateau. Additionally, inside the plateau region, changing the thickness has a much greater effect on thermal conductivity than variation of Ge composition, while outside the plateau, compositional variation dominates. As the film thickness decreases, alloying induces smaller changes in the thermal conductivity as size effects begin to dominate. Significant reduction in the thermal conductivities of thin films are observed as compared to bulk, which is due to boundary scattering of the long wavelength phonons which are the primary thermal carriers. Consequently, for minimum thermal conductivity, we want to have composition inside the plateau region in combination with nanostructuring well below the bulk limit.

A similar alloy reduction for $Al_xGa_{1-x}N$ alloys at high temperature using the virtual crystal approximation has been shown by Liu et al. [111]. Their model demonstrated the dependence of thermal conductivity on Al fraction which results in homogeneous plateau, in which the strongest composition dependence occurs at very low or very high Al mass fraction, as a result the strongest reduction of thermal conductivity is achieved when Al or Ga mass fraction is between 0.1 and 0.9. A similar trend is observed in our model for Si_xGe_{1-x} alloy, as shown in Fig. 2.1(a).

More specifically, the thermal conductivity reduces from 200 W/mK for Al_1Ga_0N to 50 W/mK for $Al_{0.9}Ga_{0.1}N$ and 20 W/mK for $Al_{0.5}Ga_{0.5}N$, about a factor of 10 decrease in conductivity for the 50% GaN case; the reduction in conductivity is much higher in SiGe alloys, about a factor of 18, as the conductivity reduces from 146 W/mK for Si_1Ge_0 to 8 W/mK for $Si_{0.8}Ge_{0.2}$.

Fig. 2.1(b) is complementary to Fig. 2.1(a) as it shows that decreasing film thickness results in reduction of thermal conductivity. Our results are again compared to and in agreement with experimental data by Cheaito et al. [31]. For example, for a SiGe layer with 20% Ge concentration, thickness of 39 nm, and boundary roughness of 0.35 nm, the calculated thermal conductivity is 1.83 W/mK, which is also in agreement with the experimental data. The interesting crossover behavior in the $x = 0.8$ (largest Ge composition) is caused by the lower phonon velocity of germanium which leads to a smaller thermal conductivity in the limit of ultra-thin samples. In Fig. 2.1(c), the calculated thermal conductivity of $Si_{1-x}Ge_x$ thin films is plotted against sample thickness for different boundary roughness, showing reduction in conductivity with decreasing film thickness. The behavior of thermal conductivity as the thickness is reduced to the sub nanometer regime depends on the model and the assumptions therein. Cahill's minimum thermal conductivity model [29] implies that the scattering rate has an upper bound which is reached when the phonon lifetime equals one period of vibration. Hence the upper bound on the scattering rate is given by $\tau_{max}^{-1} = \omega/\pi$. Including this maximum scattering rate given by Cahill's minimum thermal conductivity model allows us to reproduce the experimental values for amorphous Si (1 W/mK) and Ge (0.6 W/mK). Setting this upper bound on the phonon scattering rate leads to thermal conductivities which converge to the values given by the minimum conductivity model, as shown by solid lines in Fig. 2.1(d).

In the completely diffuse limit (p=0), the boundary scattering rate is proportional to thickness, and the conductivity scales linearly with thickness. If the boundary scat-

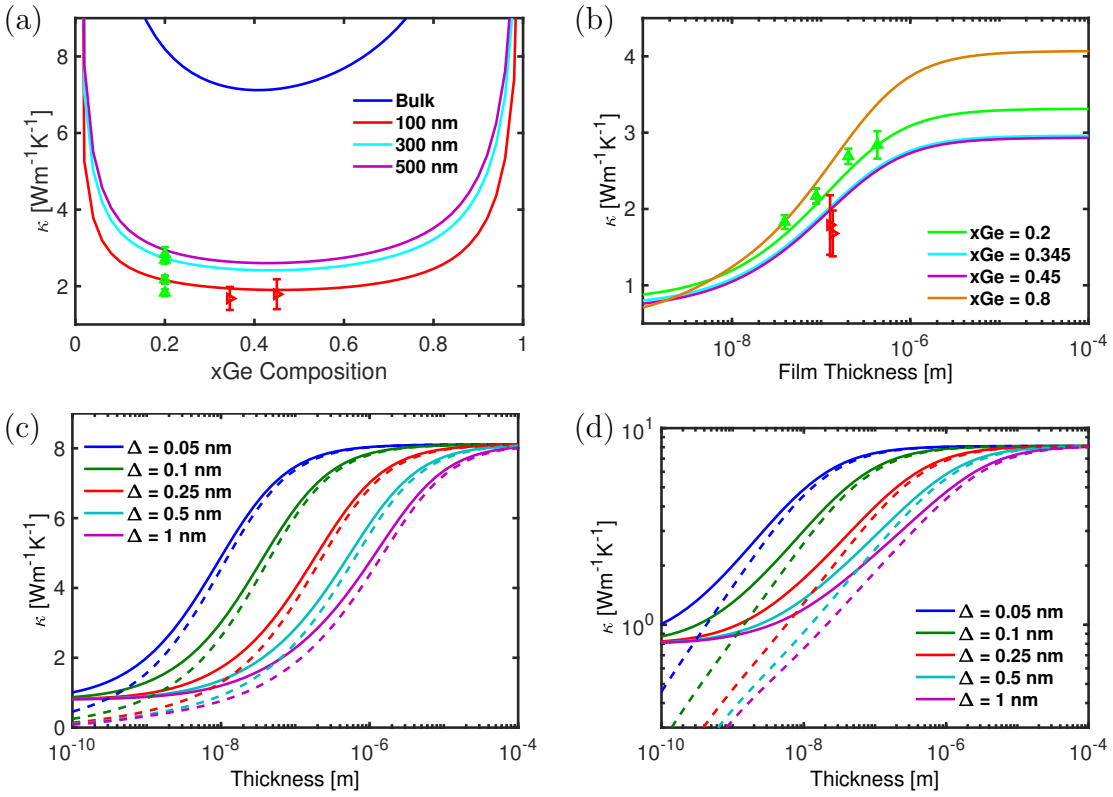

Figure 2.1. (a) Thermal conductivity as a function of Ge composition is plotted for bulk and $Si_{1-x}Ge_x$ thin-films of 100, 300, and 500 nm thichness at room temperature. The symbols correspond to experimental data on the thickness series (upward triangles) and composition series (rightward triangles) by Cheaito et al. [31]. The plot demonstrates strong quadratic dependence on the Ge composition with a plateau between $0.2 < x < 0.8$. (b) Thermal conductivity of $Si_{1-x}Ge_x$ alloy is plotted versus film thickness for four different germanium composition values of 0.2, 0.345. 0.45, and 0.8 at room temperature. The symbols correspond to experimental data on the thickness series (upward triangles) and composition series (rightward triangles) by Cheaito et al. Decreasing the film thickness causes significant reduction in the thermal conductivity for different compositions.(c) Thermal conductivity of $Si_{1-x}Ge_x$ alloy is plotted versus film thickness for five different roughness values of 0.05, 0.1, 0.25, 0.5, and 1 nm at room temperature for germanium composition of 0.2. The solid lines represent the conductivity tending to the amorphous limit and the dashed lines show the conductivity scaling with thickness below the amorphous limit. Increasing the roughness yields a gradual reduction in thermal conductivity, starting as the film thickness dips below 10 μm and reaching the amorphous limit as the thickness approaches the nanometer scale. (d) The same plot on a log-log scale to show the conductivity scaling linearly with thickness below the amorphous limit (dashed lines). Taken from Ref. [184].

tering rates are allowed to scale with decreasing thickness above τ_{max}^{-1}, then thermal conductivity gradually dips below the minimum value predicted by the minimum thermal conductivity model, often referred to as the amorphous limit, as shown by dashed in Fig. 2.1(d). In that case, the trends are in agreement with recent measurements below the amorphous limit by Feser et al. [51]. More generally, this model connects the boundary specularity $p(\vec{q})$ with roughness and finds that specularity depends exponentially on the rms roughness Δ; when thickness is reduced to the point that boundary roughness becomes comparable to the thickness, the exponential dependence of conductivity on roughness becomes more prominent and the conductivity would tend to zero at a slower rate than the linear dependence predicted by the completely diffuse model. Hence, the dependence of the thermal conductivity on thickness would also include the consideration of roughness and the amorphous limit is reached when both roughness and thickness become comparable to the unit cell size (0.543 nm in Si). In addition to the thickness dependence, increasing the boundary roughness also produces a reduction in thermal conductivity due to increased boundary scattering, as indicated in Fig. 2.1(c), more emphasized in thin films before saturation is reached at large thickness values. Increasing the boundary roughness yields a reduction in thermal conductivity, more emphasized in larger samples as at smaller scales the conductivity is already limited by the size of the sample and increasing the boundary scattering will not reduce it further.

2.3 Lattice thermal conductivity in SiGe superlattices

SiGe SLs are bi/multi-layered structures composed of regular alternating layers of Si, Ge or SiGe of varying composition, wherein the individual thickness of each layer is on the order of a few nanometers to several tens of nanometers. SLs have been found both experimentally and theoretically to have thermal conductivity below that of bulk $Si_{1-x}Ge_x$ alloys due to the combined effect of alloying and quantum

confinement of particles due to nanostructuring [100, 99, 113, 8, 184]. Bismuth-based SLs have been reported to possess very high figures of merit of around 2.6 [186]. The impact of SL structure on lattice thermal conductivity has been attributed to a number of effects such as modification of the phonon spectrum, phonon localization, and scattering of phonons at the rough interfaces. Thermal conductivity of Si/Ge SL samples was measured to be lower than that of the corresponding alloy films [72], while in other materials, such as GaAs/InAs and bismuth-based SLs, the thermal conductivity was measured to be higher than that of the alloy film having equivalent overall composition. Initial research on lattice thermal conductivity in superlattices was concentrated on lattice dynamics and the effect of periodicity on the phonon velocity [73], but measured values of thermal conductivity could not be accounted for entirely by considering reflections at interfaces and reduction in phonon velocity due to confinement, measurements indicated an increase in thermal conductivity with increasing period thickness, conflicting the expected trend due to intrinsic effects [32].

Thermal transport in semiconductor SLs can be separated into two main directions based on symmetry: one being parallel to the plane of the layers, called the in-plane transport [85] and the other being perpendicular, called the cross-plane transport. The cross-plane direction is typically of much more interest for TE applications due to its lower lattice thermal conductivity [27, 28]. In SLs with small period thickness, phonons are scattered by atomic-scale roughness present at the boundaries between successive layers. Roughness scattering is especially prominent in the cross-plane lattice thermal conductivity, which is governed by extrinsic rather than intrinsic effects [32, 164, 207]. This is particularly true for Si/Ge and $Si/Si_{1-x}Ge_x$ SLs, where the large mismatch between lattice constants and other material properties can lead to significant imperfections and appreciable roughness at the interfaces between layers, typically having several monolayers (ML, where 1 ML$\approx$0.13 nm) of roughness between the dissimilar layers in the SL [72]. Therefore, interface properties, such as roughness

[125], transport direction and crystal orientation [6], in addition to alloy composition [44], are expected to play a significant role in thermal transport. They offer additional degrees of freedom to control the thermal conductivity in semiconductor nanostructures based on SLs, thereby opening up possibilities for further enhancement of the TE figure-of-merit through the reduction in lattice thermal conductivity.

Inside each layer of superlattice, every time the phonon reaches the boundary of that layer, one of two things must happen: the phonon will either continue traveling unscattered to the neighboring layer; this occurs in the case of a specular interaction, with probability given by the momentum-dependent specularity parameter $p(\vec{q})$, given earlier in Eq. (2.13). In the alternate case, called the diffuse case, the phonon will be scattered in a random direction with probability $1-p(\vec{q})$. The addition of boundaries in one of the crystal directions breaks the symmetry and increases the anisotropy of the thermal transport between the direction of transport and the direction normal to the boundaries. In general, since the boundary scattering rate for each phonon mode depends on the angle between its group velocity and the boundary normal, phonons interacting with the boundaries at low angles of incidence will undergo fewer and more specular collisions, thereby contributing more to transport in the direction parallel to the boundaries and increasing the anisotropy.

Once the thermal conductivity tensor κ for each of the two alternating layers is obtained, it can be decomposed into the two primary in-plane and cross-plane components. Owing to the cubic crystal symmetry of the underlying lattice, the tensor is diagonal. However, the diagonal components are not all equal due to the periodic SL structure breaking the rotational symmetry. From the full thermal conductivity tensor Eq. (2.17), we can compute thermal conductivity by projecting it along any direction as $\kappa^{\alpha\beta} = \hat{n}^{\alpha}\kappa\hat{n}^{\beta}$ with $\hat{n}$ being the unit vector along the direction of transport [7]. Subsequently, the conductivities of the two repeating layers in the SL will be combined in series for cross-plane transport and in parallel for in-plane transport;

however, the cross-plane direction also has a small additional component of thermal resistance due to the acoustic mismatch between the layers, which adds a Kapitza resistance in series with the individual layers themselves

$$\begin{aligned} \kappa_{\text{in-plane}} &= \frac{L_1\kappa_1^{xx} + L_2\kappa_2^{xx}}{L_1 + L_2} \\ \kappa_{\text{cross-plane}} &= \frac{L_1 + L_2}{\frac{L_1}{\kappa_1^{yy}} + \frac{L_2}{\kappa_2^{yy}} + \frac{1}{\sigma_1^{AIM}} + \frac{1}{\sigma_2^{AIM}}}. \end{aligned} \tag{2.19}$$

The acoustic impedance mismatch (AIM) term has been found to add only a minor correction to the overall thermal conductivity in the extreme case of a Si/Ge SL, and even smaller in alloy-based SLs due to smaller mismatch when both layers are composed of SiGe alloys [8].

The additional scattering of phonons at the imperfect interfaces separating the SL layers leads to a two orders-of-magnitude reduction in thermal conductivity compared to bulk in Si/Ge SLs (Figs. 2.2(a) and 2.2(b)). The resulting thermal conductivity is lower than that of a $Si_{1-x}Ge_x$ alloy with the same proportions of Si and Ge in agreement with [175]. This can be attributed to the additional boundary roughness scattering of phonons, especially the low-energy (long wavelength) acoustic phonons which are not strongly scattered by the Rayleigh-like mass-disorder scattering, given previously in Eq. (2.6). The lowest thermal conductivity is achieved when each of the layers is an alloy, which requires that the two layers are made up of different alloy compositions. In such a SL, thermal conductivity reaches almost to the amorphous limit due to the combined effect of strong mass-difference scattering internal to the alloy layer and roughness scattering at the boundaries between the alloy layers, seen in Figs. 2.2(c) where both the layers are $Si_{1-x}Ge_x/Si_{1-y}Ge_y$ alloys with different composition of x=0.2 and y=0.8. In SLs, both period thickness and total length play an important role; however, total sample thickness is only significant when the rough-

ness is small and the phonon MFPs are not interrupted by the roughness scattering at the layer boundaries before they can reach the sample ends, as shown for both pure Si/Ge (Fig. 2.2(b)) and alloy SLs (Fig. 2.2(d)). The dependence on both sample and period thickness is more pronounced in pure Si/Ge SLs where the absence of alloy mass disorder implies that the thermal conductivity reaches the bulk limit in thick samples.

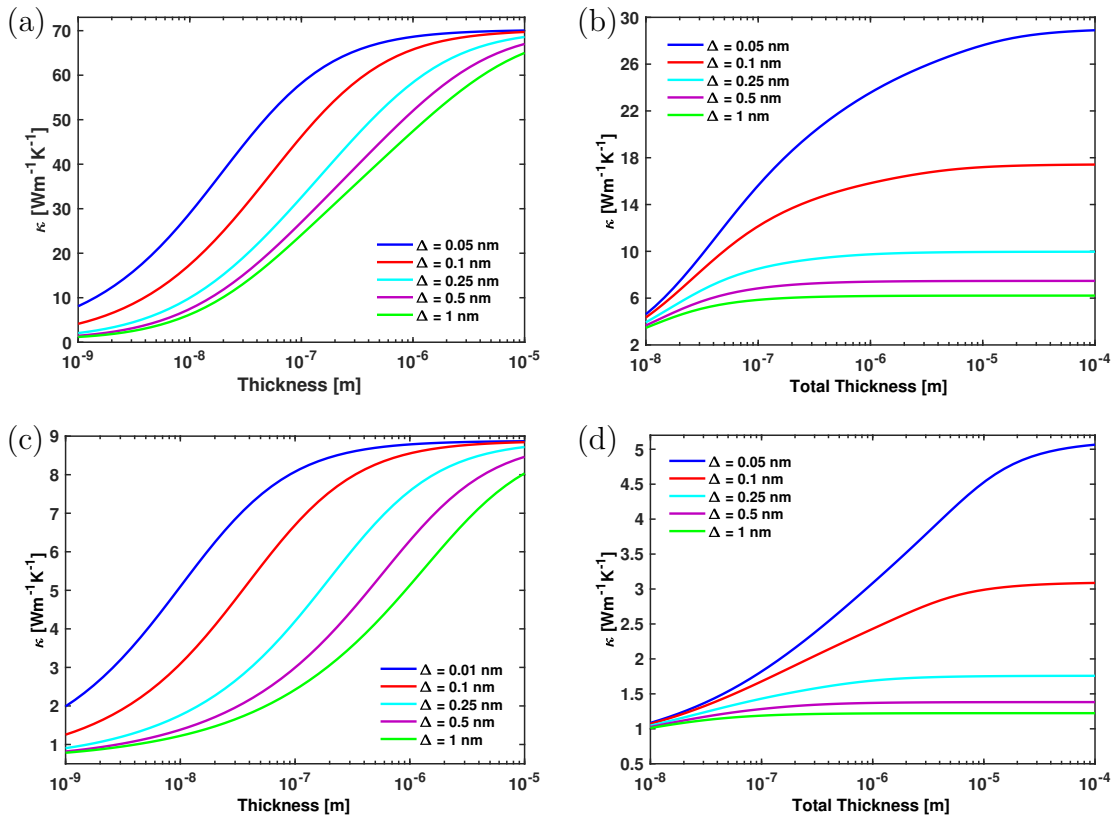

Figure 2.2. Room temperature cross plane thermal conductivity of a Si/Ge SL vs. (a) SL bi-layer period thickness with fixed total sample thickness of 200 μm and (b) total sample thickness with fixed period thickness of 10 nm. Cross plane thermal conductivity of a $Si_{0.8}Ge_{0.2}/Si_{0.2}Ge_{0.8}$ as a function of (c) bi-layer period thickness with total sample thickness of 200 μm and (d) total sample thickness with period thickness of 10 nm, for five different boundary roughness values of 0.05 nm, 0.1 nm, 0.25 nm, 0.5 nm, and 1 nm. Increasing the boundary roughness yields further reduction in thermal conductivity. Taken from Ref. [184].

Fig. 2.3(a) and Fig. 2.3(b) show the in-plane conductivity for the Si/Ge and $Si_{0.2}Ge_{0.8}/Si_{0.8}Ge_{0.2}$ SLs. The in-plane thermal conductivity is higher due to the reduced effect of the boundry roughness scattering, which is more emphasized as the thickness of the individual layers is reduced. The inset figures show the anisotropy ratio (in-plane/cross-plane conductivity), which has the highest value at small layer thickness and saturates to a value of around 1.3 as the layer thickness is increased above 1μm.

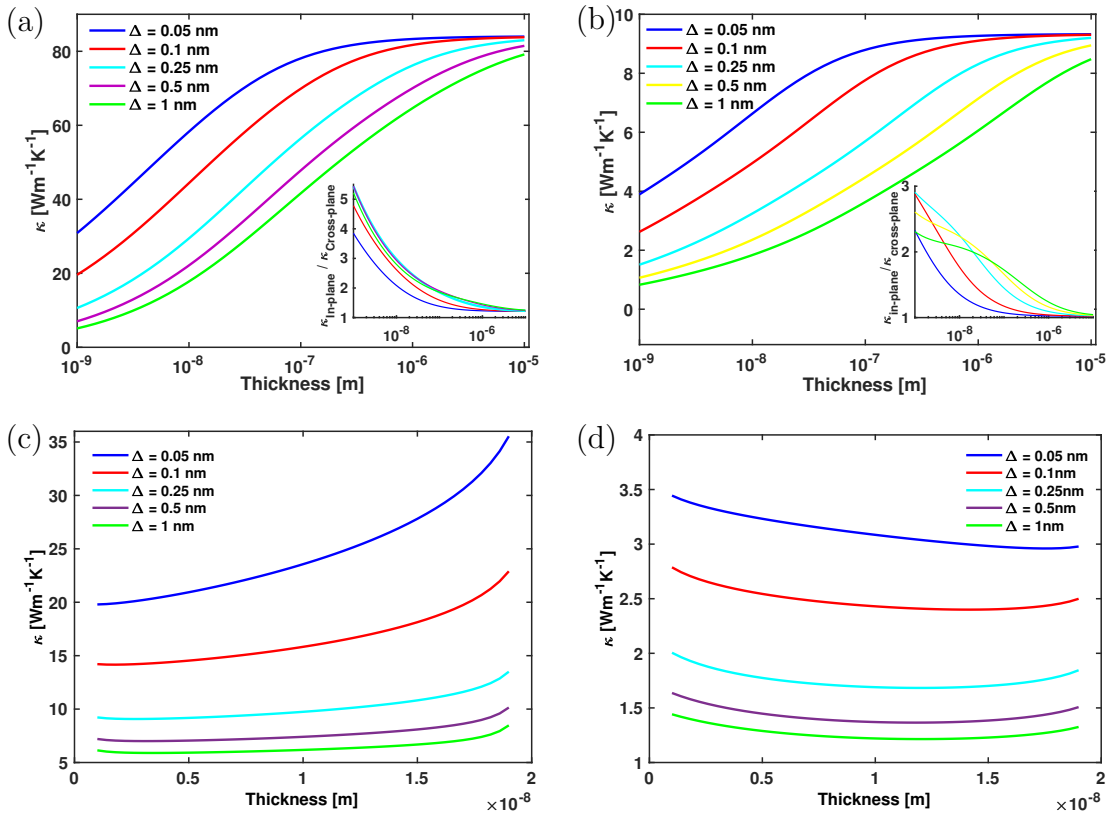

Figure 2.3. Room temperature in-plane thermal conductivity of (a) Si/Ge and (b) $Si_{0.8}Ge_{0.2}/Si_{0.2}Ge_{0.8}$ SL. Results are plotted as a function of bi-layer period thickness for five different boundary roughness values of 0.05 nm, 0.1 nm, 0.25 nm, 0.5 nm, and 1 nm (the total sample thickness is 200 μm). (Inset) The anisotropy ratio as a function of total sample thickness showing increasing anisotropy as thickness is reduced. Room temperature lattice thermal conductivity of (c) Si/Ge and (d) $Si_{0.8}Ge_{0.2}/Si_{0.2}Ge_{0.8}$ bi-layers with the period thickness fixed at 20 nm. The total sample thickness is 200 μm, while the thickness of the first layer is varied from 0 to 20 nm. Taken from Ref. [184].

Varying the relative thickness of the two layers, while keeping both period and total sample thicknesses fixed at 20 nm and 200 μm, respectively, shows that the lowest thermal conductivity occurs when the Si layer is thinner than the Ge layer in pure Si/Ge SLs (Fig. 2.3(c)). This is due to the lower intrinsic thermal conductivity of Ge ($\kappa \cong 56$ $\mathrm{Wm^{-1}K^{-1}}$ at room T [61]). In contrast, alloy SLs have lower thermal conductivity when the Si-heavy layer (with x=0.2 of Ge) is dominant (thicker) and the second Ge-heavy layer (with y=0.8) is thinner, as shown in Fig. 2.3(d). This is again caused by the layer possessing lower thermal conductivity being preferred; in the alloy case, it is predominantly the Si layer which has lower conductivity (as seen from the asymmetry of the curves toward the Si side in Fig. 2.1(a), especially in the bulk case) due to the smaller Si mass being further from the alloy average than the heavier Ge mass, causing more mass-disorder scattering, as defined in Eq. (2.5). Hence, composition must be precisely taken into account when designing SiGe SLs for TE applications because the lattice thermal conductivity will in general be minimized by making the layer with lower thermal conductivity thinner; for example, in a SL where only one layer is composed of an alloy (while the other is either pure Si or pure Ge), the non-alloy layer should be made as thin as possible in order to emphasize the contribution from the roughness scattering, while the alloy layer can be made thicker since the mass-disorder will keep its conductivity low. The quantum dot superlattice system measured in [160] and [13] has alternating layers of silicon and SiGe quantum dots which are around 1-2 nm thick. The diameter of these dots is smaller than the average phonon mean free path and they form very efficient scattering sites. In our model we can treat this as layers of silicon separated by very rough boundaries, with 20 nm thick Si layers and boundary roughness of 1.2 nm the thermal conductivity is 12.1 W/mK, very close to the measured value of 11 W/mK with 20 nm Si layer and quantum dot layer of 1.2 nm.

2.4 Conclusion

This chapter describes the lattice thermal conductivity in nanostructured SiGe alloys, including thin films and SLs. We solve the pBTE with the full phonon dispersion and a momentum-dependent specularity model for boundary roughness scattering, that effectively captures the interplay between intrinsic and interface scattering mechanisms. There's an order-of-magnitude reduction in thermal conductivity due to alloying, and further decrease is achieved in nanostructures, with conductivity nearing the amorphous limit. Thermal conductivity is optimized in SLs by reducing the overall thickness of the superlattice period, increasing the roughness of the interfaces, and either introducing alloying into both layers of the superlattice or minimizing the thickness of the pure layer in Si-alloy superlattices. The results demonstrate tunablity of thermal transport through boundary and interface properties including structure size, roughness, and composition, that are relevant to guiding the design of nanostructured SiGe alloys for TE applications.

CHAPTER 3

THERMAL CONDUCTIVITY IN SIGE NANOWIRES AND NANOCOMPOSITES

As seen in the previous chapter, alloy scattering combined with boundary scattering leads to an enormous reduction in thermal conductivity which is expected to lead to an improvement in ZT. The increase in ZT observed in thin Si wires [69] is due to the reduction of lattice thermal conductivity arising from the strong scattering of phonons with roughness at the boundaries of the wires [125]. Theoretical calculations predicted that the reduction of thermal conductivity due to alloy scattering combined with the effect of boundary scattering could lead to even more dramatic improvements of ZT in SiGe-based nanowires (SiGe NWs) [161]. Subsequent MD simulations showed that, while the maximum reduction of thermal conductivity in bulk SiGe alloys exceeds one order of magnitude, the reduction in alloy NWs is only a factor of 5 [33]. Several measurements of thermal conductivity in thin SiGe NWs with rough boundaries were performed [88, 209, 98] and confirmed the weak diameter dependence of thermal conductivity in SiGe NWs, indicating that thermal transport was dominated by alloy (mass-difference) scattering, even at low Ge concentrations. Hsiao et al. studied length dependence in SiGe NWs and found a linear trend, attributed to ballistic transport, with a clear transition to diffusive regime at lengths exceeding 8.3 μm [71]. In bulk SiGe alloys, on the other hand, Vermeersch et al. [188] have argued that the phonon transport, on time scales up to 2 ns, shows clear signs of superdiffusion; a form of diffusion in which the mean square displacement is no longer a liner function of time, it is >1.

Semiconductor NWs are typically grown using the VLS procedure [102], producing a circular geometry which leads to the usual Casimir limit $\tau_B^{-1} \propto v_s/D$ in the case where boundary scattering is independent of angle [205]. However, no closed-form solution to the BTE can be found for the case where there are both partially specular boundary scattering and strong internal (umklapp+alloy+defect) scattering present [204], and Mathiessen's rule is often used to combine the rates due to boundary scattering with the intrinsic mechanisms [195]. The closed-form solution used in the planar (membrane or thin film) case [8, 159] is not valid here because the distance from each point on the interior of the circular wire to the rough surface depends on both the angle (determined by the phonon group velocity vector) and the point of origin, in contrast to the planar case. In addition, the specularity of the boundary depends not only on the roughness, but also on the angle of incidence between the phonon and the local boundary normal [6, 167].

To overcome these challenges, we study thermal transport in SiGe NWs using the phonon Monte Carlo (pMC) technique, which has been widely used to solve the phonon Boltzmann transport equation (pBTE) [129, 34, 94, 76, 149, 143, 148]. The pMC allows us to sample the phonon lifetimes [130] and find the combined phonon lifetime in the presence of both intrinsic scattering (from anharmonic phonon-phonon and mass difference interactions inside the wire) and partially diffuse boundary scattering at the rough surface in circular wires [125]. We capture the anisotropy of thermal transport in SiGe NWs [104] due to phonon focusing effects [6], by expanding the pMC algorithm to include the full phonon dispersion [93, 131]. We use Weber's Adiabatic Bond Charge model [202] to efficiently compute the full phonon dispersion of bulk Si and Ge, and then combine them in the virtual crystal approximation (VCA). This approach has been shown to accurately capture the vibrational frequencies and group velocities of phonons in the alloy [97], as well as the thermal conductivity over a broad range of compositions [184, 84].

3.1 Phonon Monte Carlo model

In the phonon Monte Carlo algorithm, an ensemble of phonons is initialized according to the Bose-Einsten distribution [130]. Then the free-flight time until scattering of each phonon is determined by first selecting a random number $r_{int.}$, uniformly distributed between 0 and 1, and sampling the lifetime according to $t_{int.} = -ln(r_{int.})\tau_{int.}(\vec{q})$ [127]. We find the combined lifetime with both intrinsic scattering (from anharmonic phonon-phonon and mass-difference interactions inside the wire) and partially diffuse boundary scattering at the rough boundary in circular wires. The phonon lifetime $\tau_{int}(\vec{q})$ combines all the intrinsic scattering mechanisms, including anharmonic three-phonon interactions, impurity, isotope, and alloy mass-difference scattering. The resistive umklapp phonon-phonon scattering rate is calculated in the general approximation for dielectric crystals given in Eq.2.10 and the scattering from mass differences due to the presence of mass variation in the alloy from Eq. 2.6 (the details of which have been described in Sec. 2.1). Once the phonon free-flight time is determined, each phonon travels along the propagation direction given by its group velocity $\vec{v}_g(\vec{q})$, until scattering at the end of the "free flight" at $t_{int.}$ or until it encounters a boundary or contact, whichever occurs first. The boundary roughness scattering is characterized through a momentum-dependent specularity [167] $p(\vec{q}) = \exp(-\langle\phi^2\rangle)$, where $\phi(\vec{q},\vec{r}) = 2\vec{q}\cdot\hat{s}z(\vec{r}) = 2qz(\vec{r})\cos\Theta_B$ is the phase difference between the incoming wave and the outgoing specularly reflected wave at point $\vec{r}$. The surface normal unit vector at this point $\vec{r}$ is $\hat{s}$. We assume that the surface height $z(\vec{r})$ is a random function of position on the rough boundary $\vec{r}$ with a Gaussian distribution, so that $\langle z\rangle = 0$ and $\langle z^2\rangle = \Delta^2$, where Δ is the rms height of the surface roughness [63]. When a phonon reaches the rough boundary, another random number $r_{spec.}$ again uniformly distributed between 0 and 1, is used to select between a specular (mirror-like reflection about the surface normal $\hat{s}$) and a diffuse (direction after leaving surface is randomized) scattering. If $r_{spec.} < p(\vec{q})$, then the boundary interaction is specular

and the phonon is simply reflected at the boundary by flipping its momentum about the boundary normal $\vec{q}_{final} = \vec{q}_{init.} - 2\vec{q}_{init.} \cdot \hat{s}$. Otherwise, the interaction is diffuse: the phonon path is terminated and the boundary scattering time t_B is recorded as the time at which the diffuse scattering occurred and the process is restarted. We also capture the quasi-ballistic contribution arising from phonons which reach the contacts (at time t_C) before scattering internally or at the boundaries. When all the phonon flights are terminated in either internal or boundary scattering or at a contact, thermal conductivity is computed from the average

$$\kappa = \frac{1}{N_{\vec{q}} N_i} \sum_{\vec{q},i} v_g^2(\vec{q}) \min\{t_{int.}, t_B, t_C\} C(T, \vec{q}) \tag{3.1}$$

where $C(T, \vec{q})$ is the modal volumetric heat capacity [130] and $N_{\vec{q}}$, N_i are the number of phonons and iteration in the simulation, respectively, both being typically 100,000.

3.2 Results and Discussion

Fig. 3.1 shows a comparison of our calculated results to the experimentally measured thermal conductivities reported in Ref. [98] for wire diameters below 100 nm and alloy composition ranging from 6% Ge (Fig. 3.1(a)) to 86% Ge in (Fig. 3.1(h)). The Monte Carlo simulation results are shown in dashed lines and symbols while the solid lines represent the thermal conductivity from the solution of the BTE in the RTA including boundary scattering. In Fig. 3.1, κ_e is the electronic and κ_{ph} is the phononic contribution to thermal conductivity. The MC model is in close agreement with the RTA model, which has been validated in Ch. 2. Also, our results reproduce the experimental values closely across a wide range of temperatures, diameters, and compositions, with some discrepancy at the highest Ge composition, which may be attributed to the presence of contact resistance, not included in our model.

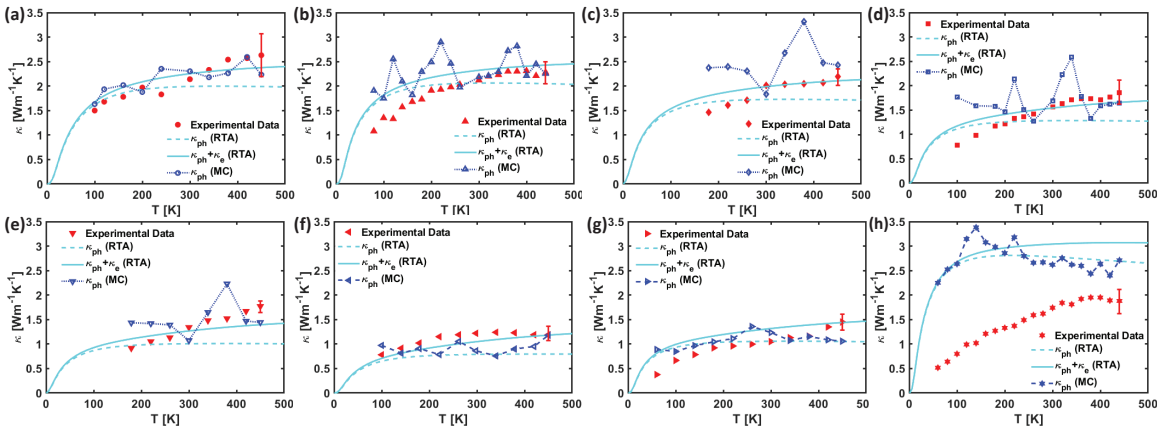

Figure 3.1. Thermal conductivity vs. temperature for different wire configurations. a length=5.7 μm, diameter=56 nm and 6% Ge, (b) length=6.3 μm, diameter=97 nm and 8% Ge, (c) length=5.6 μm, diameter=45 nm and 10% Ge, (d) length=5 μm, diameter=62 nm and 19% Ge, (e) length=11.6 μm, diameter=26 nm and 26% Ge, (f) length=5.3 μm, diameter=26 nm and 27% Ge, (g) length=5.2 μm, diameter=65 nm and 41% Ge, (h) length=6.2 μm, diameter=161 nm and 86% Ge showing a comparison of results computed based on our RTA (cyan line) and MC (blue $-\circ-$) model to experimental values (red $\bullet$) reported in Ref. [98]. Taken from Ref. [181].

3.2.1 Diameter and roughness dependence

Fig. 3.2(a) depicts the thermal conductivity vs. diameter for NWs of different lengths and surface roughness Δ. The results were computed for NWs with 20% Ge concentration at room temperature. The conductivity shows an almost linear diameter dependence at intermediate diameter values for pure Si [205], where boundary scattering is dominant. The deviation from this linear dependence increases with alloying. Alloy scattering rate follows a Rayleigh-like trend ($\tau_M^{-1} \propto \omega^4$ because $g(\omega) \propto \omega^2$ in the long-wavelength regime) and suppresses the contribution of higher-frequency phonons to thermal conductivity, whereas the low-frequency (long-wavelength) phonons remain nearly unaffected.

The high-frequency phonons tend to undergo a more diffuse scattering at the boundaries causing a stronger diameter dependence seen in Si NWs, whereas the low frequency phonons undergo a more specular boundary scattering and have smaller

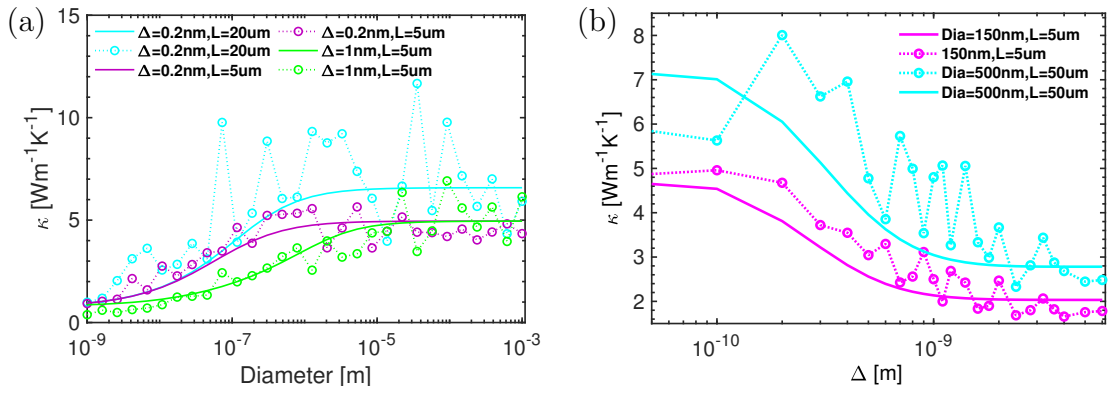

Figure 3.2. (a) Thermal conductivity is plotted as a function of the wire diameter. The diameter dependence is weak due to strong intrinsic scattering. Solid lines represent the BTE results and dashed lines represent Monte Carlo results. (b) Thermal conductivity is plotted as a function of surface roughness. For Δ values of 1 Åor less, the conductivity is unaffected and it steadily decreases as the roughness is increased, without any further significant decrease beyond 1 nm. Taken from Ref. [181].

diameter dependencies, indicating that it is the mid-range phonons that cause the weak diameter dependence in SiGe NWs. Surface roughness dependence of thermal conductivity is shown in Fig. 3.2(b). There is a steady decrease in conductivity with an increase in surface roughness up to 1 nm due to more diffuse boundary scattering, but further increase in roughness does not further reduce the conductivity, which saturates to a value much lower than in pure Si NWs. However the reduction in conductivity due to increased diffuse boundary scattering in SiGe NWs is not as effective as in pure Si NWs, primarily in thin wires where boundary scattering is dominant, due to the supression of the high frequency phonons by alloy scattering. For a pure Si NW of 10 nm diameter and 100 nm length, we calculated a 75% reduction in conductivity when surface roughness was increased from 0 to 1 nm, whereas the reduction is about 52% for a SiGe NW of the same dimension.

3.2.2 Length dependence: ballistic and diffusive contributions

Next, we study the dependence of thermal conductivity on the length and composition of the NW. Fig. 3.3(a) shows the dependence of thermal conductivity from

pMC simulations on NW length. The dashed lines and symbols are the Monte Carlo results, while solid lines are the deterministic solution of the pBTE in the RTA, shown for comparison, and they are in close agreement. We observe a gradual change in thermal conductivity with length, as seen in Fig. 3.3(a), with the crossover to purely diffusive transport only occurring at lengths exceeding 10 μm, far in excess of the average phonon MFP and in agreement with measurements [71]. Alloying suppresses most of the high frequency phonons while the low frequency phonons possess very long MFPs, allowing them to travel several microns without being scattered internally. However, even at very small NW lengths, we do not observe the linear trend in the length dependence that would be characteristic of ballistic transport; instead, we find in Fig. 3.3(a) that the conductivity scales as $L^{1/3}$.

We plot the running exponent of our results, defined as $\alpha(L) = d\ln\kappa(L)/d\ln L$ [157], in Fig. 3.3(b) and observe that all SiGe NWs follow the same trend regardless of diameter, with $\alpha < 0.4$ even when L <10 nm. In contrast, short Si NWs reach the fully ballistic regime (characterized by α=1). The $\alpha \approx 0.33$ behavior has been observed in many momentum-conserving systems [42], including 1-dimensional chains [101, 121], alloy thin films [187], and, over a much narrower range of lengths, even thin Si NWs [208]. However, the upper limit of length at which we still observe exponent $\alpha \approx 1/3$ depends on boundary scattering: in a rough wire (Δ=1 nm), the exponent reduces to the diffusive α=0 at a shorter length than in a smooth wire (where Δ=0.2 nm). Diffuse boundary scattering limits the longest MFP and thus results in a more uniform MFP distribution. Hence boundary scattering affects the range of length over which we observe $\alpha = 1/3$ but not the length-scaling exponent α. Alloy scattering, on the other hand, results in an intrinsically different mode of transport having a broader range of MFPs with very few purely ballistic phonons.

In order to shed further light on the origin of the $\kappa(L) \propto L^{1/3}$ length dependence, we first compare it to the ballistic-to-diffusive transition picture suggested by the

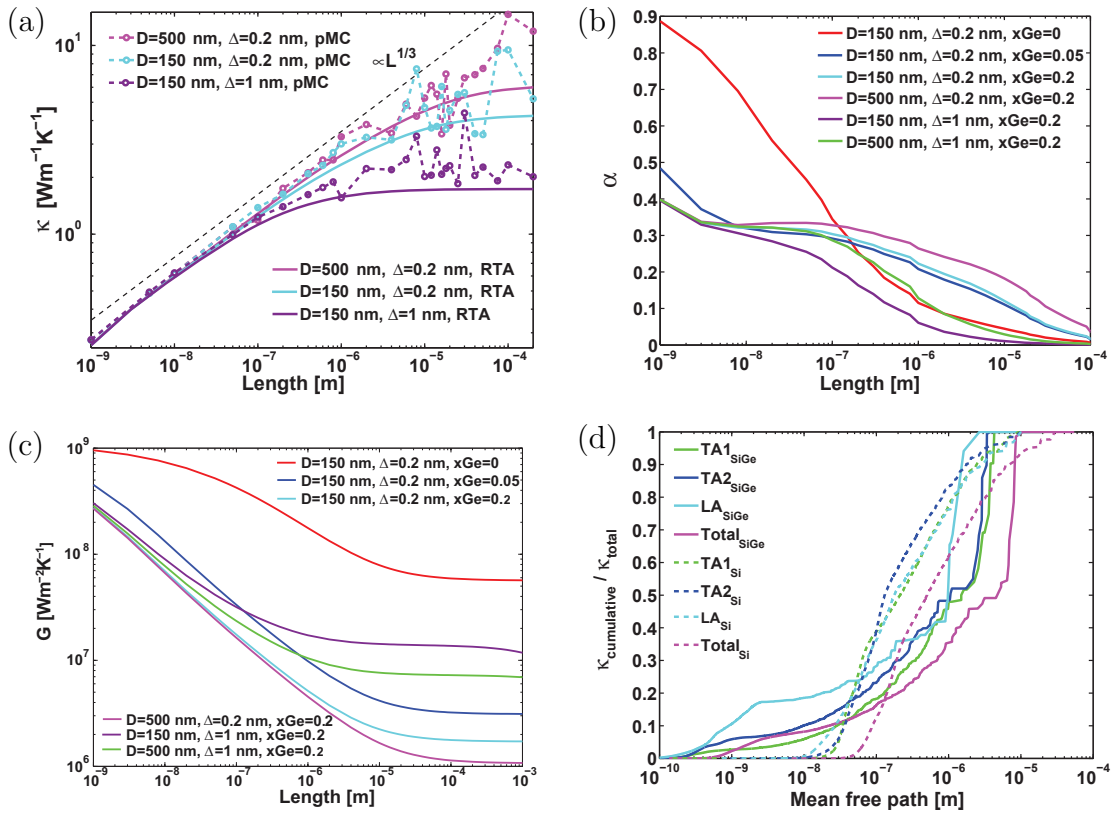

Figure 3.3. (a) Thermal conductivity as a function of length. The solid lines represent the RTA and dashed lines represent the MC results. The conductivity exhibits a $L^{1/3}$ behavior and gradually transitions into the diffusive regime at lengths exceeding 10 μm. (b) Exponent of length dependence α as a function of length. In SiGe NWs, $0.3 < \alpha < 0.4$ over a broad range of lengths, indicating non-diffusive transport. (c) Thermal conductance G, as a function of length in Si and alloy NWs of varying diameter, roughness, and composition. (d) Cumulative thermal conductivity as a function of the phonon MFP for the three acoustic branches and their sum in bulk Si (dashed lines) and $Si_{0.5}Ge_{0.5}$ alloy (solid lines), showing the broad range of MFPs in SiGe alloy. Taken from Ref. [181].

linear trend in the experimental data [71]: we take the total resistance in the wire as a sum of the ballistic (G_{Bal}^{-1}) and diffusive (L/κ_{diff}) resistances [12], which results in

$$\kappa(L) = \left(\frac{1}{LG_{Bal}} + \frac{1}{\kappa_{diff}} \right)^{-1}, \tag{3.2}$$

where $\kappa(L)$ is the length dependent conductivity, L is the length of the NW, and κ_{diff} is the conductivity in the diffusive ($L \to \infty$) limit. Since $\kappa(L)$ and κ_{diff} are

known (Fig. 3.3(a)), we can rearrange Eq. 3.2 to calculate the ballistic conductance G_{Bal} for different NW lengths. The ballistic conductance G_{Bal} of Si is equal to 10^9 $Wm^{-1}K^{-1}$ [127]. As seen in Fig. 3.3(c), when wire length is below 10 nm (much smaller than the MFP in bulk Si) the ballistic conductance of Si NWs plateaus at 10^9 $Wm^{-1}K^{-1}$, matching the theoretical value; in contrast, the conductance in ultrashort SiGe NWs is only $\approx 2 \times 10^8$ $Wm^{-1}K^{-1}$, about 20% of the ballistic conductance. We also observe that no more than a small fraction of the ballistic conductance is present in SiGe NWs at any length, regardless of diameter and roughness. Hence, transport in alloy NWs is never predominantly ballistic, indicating that the direct ballistic-to-diffusive crossover picture is incomplete. The fraction of ballistic conductance reduces as length increases but about 1% is still present at lengths exceeding 10 μm.

The unique properties of alloy nanostructures can be partly analyzed through the prism of the conductivity vs. MFP plot, shown in Fig. 3.3(d). We observe a much broader range of MFPs contributing to transport in alloys than in pure Si. There is a large relative contribution to thermal conductivity made by phonons having large MFPs, primarily found in the low-energy range of the acoustic phonon branches where both mass disorder (alloy) and anharmonic scattering rates are low, while the boundary scattering is more specular, owing to the large wavelength (small q) of phonons in this range. We conclude that in the SiGe alloy, most phonons have very short MFPs and conseqeuntly they make a relatively small contribution to thermal conductivity, while fewer phonons have very long MFPs exceeding one micrometer, but they make a substantial contribution to thermal transport. The 50% accumulation point where one half of the total thermal conductivity is reached corresponds to MFPs of around one micrometer, implying that half of the heat is carried by phonons with MFPs exceeding a micron; in contrast, such phonons only contribute around 20% in pure Si.

3.2.3 Phonon flight lengths and the diffusion coefficient

Next, we plot the distance along the NW traveled by one simulated phonon through a sequence of free flights interrupted by scattering events. Each flight number in the plot corresponds to a single free-flight between successive scattering events for both Si (Fig. 3.4(a)) and $Si_{0.8}Ge_{0.2}$ (Fig. 3.4(c)). We focus on a Ge composition of 0.2 as that is typically found to be optimal for TE applications [189]. One phonon is chosen from the ensemble at random as a representative and plotted, having found all of the simulated phonons to exhibit qualitatively similar behavior. The scattering is predominantly elastic, arising in both cases from boundary roughness, while in alloy NWs there is a strong additional component due to mass disorder.

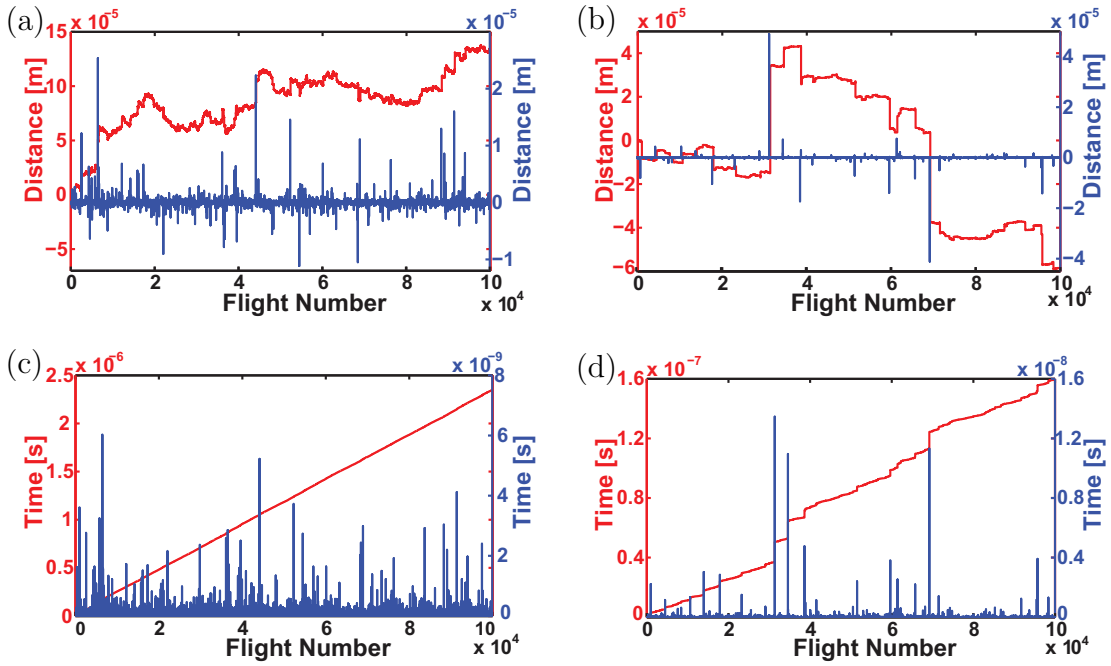

Figure 3.4. The distance traveled by one simulated phonon between successive scattering events (blue dotted line), and the cumulative distance (red line) vs. flight number is plotted for (a) a pure Si nanowire and (b) a $Si_{0.8}Ge_{0.2}$ nanowire. Also, the time between scattering events (blue dotted line) and the cumulative time (red line) is plotted vs. the flight number in (c) pure Si NW and (d) $Si_{0.8}Ge_{0.2}$ NW. Si NWs have a more uniform distribution of distance and flight time between scattering events, whereas in SiGe NWs we can see the short flights interrupted by long jumps. Taken from Ref. [181].

It is interspersed by less frequent inelastic (anharmonic phonon-phonon) events which mix the phonon modes. We find Si NWs to have a more continuous distribution of distances due to the series of relatively uniform flights characteristic of diffusive transport, leading to a white-noise-like appearance seen in Fig. 3.4(a), which is readily associated with Brownian motion and predominantly diffusive transport.

In contrast, phonon flights in SiGe NWs are comprised of sequences of many short flights interrupted by rare long leaps, as evidenced by the micron-sized jumps in the distance traveled by the phonon shown in Fig. 3.4(c). This behavior in the alloy is a consequence of the strong mass disorder scattering, which has a Rayleigh-like dependence on phonon frequency ($\tau_M^{-1} \propto \omega^4$) and affects the upper portion of the phonon spectrum far more than the low-frequency modes. Viewing the whole phonon ensemble collectively, the result is a heavy-tailed distribution of free-flight lengths, shown in Fig. 3.5(a). The difference is especially prominent when we compare alloy NWs to pure Si NWs, in which the tail of the phonon flight distribution decays faster. Phonons making long jumps exceeding 1μm are more than twice as frequent in SiGe NWs as they are in Si NWs, as seen in the distribution of flight lengths Δx as measured in the direction of heat flow along the NW. The difference alloy and non-alloy steadily increases for longer leaps, in spite of alloy scattering causing phonons in SiGe to have MFPs more than an order of magnitude shorter on average than pure Si. The heavy-tailed behavior is characteristic of Lévy walk dynamics [43, 212], which has already been linked to superdiffusive phonon transport in low-dimensional [37] and alloy systems [188].

We further study the non-diffusive behaviour of phonons in alloy NWs by examining the time-dependent phonon transport calculated from our pMC simulations. The time dependence of the mean square energy displacement (MSD) [41] is calculated from $\sigma^2(t) = \langle \Delta x^2(t) \rangle$ and related to an exponent $\sigma^2(t) \propto t^\beta$. Consequently, the diffusion coefficient $\sigma^2(t)/2t \propto t^{\beta-1}$. The exponent of length dependence α, shown

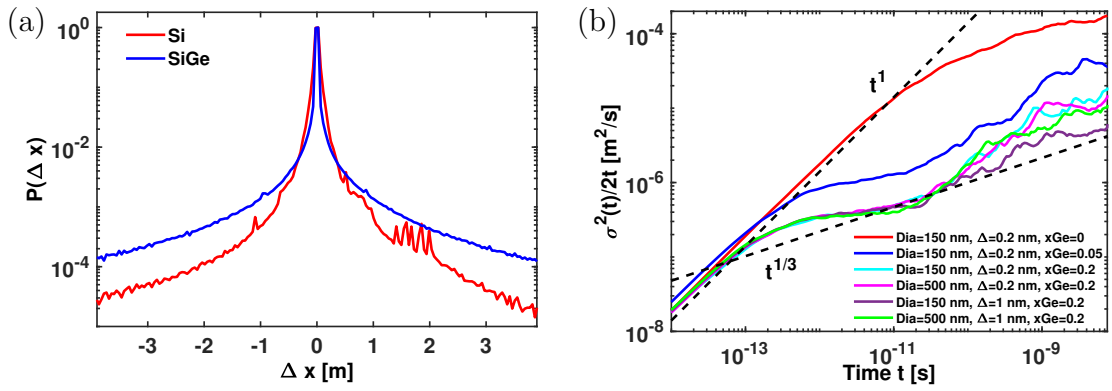

Figure 3.5. (a) Histogram of the individual free-flight lengths in Si (red) and $Si_{0.8}Ge_{0.2}$ NWs (blue). SiGe NWs show a larger proportion of long leaps, which leads to a heavy-tailed distribution. (b) Diffusion coefficient vs. time. In SiGe NWs we observe a broad intermediate regime in which the exponent of the diffusion coefficient is ≈ 0.33 over several orders of magnitude in time, whereas in Si NWs we observe $\alpha = 1$ in the ballistic regime followed by a smooth transition into the diffusive ($\alpha = 0$) regime. Taken from Ref. [181].

previously in Fig. 3.3(b), has also been related to the MSD through $\alpha = \beta - 1$ [109]. In normal diffusion, where Fourier's law remains valid, phonons undergo Brownian motion resulting in $\beta = 1$ (as $\sigma^2(t) \propto t$) [163], which also means the exponent of length dependence $\alpha = 0$ and the conductivity is constant, independent of length. In contrast, when the system size is smaller than the MFP, phonon flights are uninterrupted by scattering and their distance from origin grows in proportion with time; hence, ballistic MSD is quadratic in time ($\beta = 2$), implying that $\alpha = 1$ and the conductivity is linearly proportional to length [105].

Our observed $\alpha = 1/3$ scaling is attributed to an intermediate regime of superdiffusion: when $1 < \beta < 2$ transport is neither entirely ballistic nor diffusive. Instead, it is collectively characterized by a mix of long quasi-ballistic leaps, interrupted by bursts of short, diffusive steps. Consequently, the diffusion coefficient $\sigma^2(t)/2t \propto t^\alpha$ should also imply a length exponent $0 < \alpha < 1$ in the superdiffusive regime. We plot the diffusion coefficient $\sigma^2(t)/2t$ as a function of simulation time in Fig. 3.5(b), and observe that $\alpha = 1/3$ (and $\beta = 4/3$) over a wide range of time scales in SiGe NWs.

In bulk SiGe alloys and SiGe thin films in the cross-plane direction, Vermeersch et al. [188, 187] have shown that β=1.34, in close agreement with our findings, confirming that our length scaling is a consequence of superdiffusion.

The range of lengths over which we observe superdiffusion ($\alpha \approx 1/3$ over 10 nm$< L <$ 10 μm) far exceeds the average phonon MFP in the system; instead, it maps directly to the wide range of timescales over which superdiffusion is observed here in SiGe NWs (2 ps$< t <$2 ns in Fig. 3.5(b)) using the simple cut-off $t_s \approx L/v_s$ for superdiffusion in finite systems [101, 109], with v_s being the speed of sound ($v_s \approx 5000$ m/s in SiGe, depending on alloy composition). We observe that diameter and roughness do not alter the exponent of the diffusion coefficient; instead, they affect only the onset of the transition from superdiffusion ($0 < \alpha < 1$) into purely diffusive regime ($\alpha = 0$), thus reducing the resulting conductivity in the steady-state analogously to its length dependence in Fig. 3.3(a).

3.3 Thermal Conductivity in SiGe Nanocomposites

Nanocomposites (NCs) offer a tremendous advantage in their ease of manufacturing compared to SL structures that have to be grown layer-by-layer from the ground up and have high cost. NCs are made by relatively simple and cheap mechanical processing of materials, such as ball milling the bulk material into a fine powder of nanoscale grains, followed by spark plasma sintering into a nanostructured bulk composite [112], thereby making such "nano-bulk" materials much more amenable to scaling and commercialization [95]. However, the resulting NCs have a very heterogenous structure with grains ranging in size from a few nanometers to hundreds of nanometers, typically following an exponential distribution [96]. The grain properties, including atomic-scale grain-boundary roughness (GBR), orientation, and composition, will also substantially affect thermal transport in NCs, offering numerous ways of adjusting their thermal conductivity by manipulation of grain size, shape, and

crystalline angle distributions. Hence NCs can be designed to improve ZT by reducing lattice thermal conductivity by a combination of approaches including additional scattering of phonons from the interfaces between nanoscale grains of dissimilar materials, alloys of different composition, or grains with different crystal orientation [83].

3.3.1 PBTE model based on Voronoi tessellation

Our model for NCs is based on solving the phonon Boltzmannn transport equation with partially diffuse boundary conditions at the grain boundaries, similar to the model described previously in Sec. 2.2, but modified to capture fully the complex heterogenous structure of the NC [5]. Voronoi tesselation (VT) is employed to discretize the material into grains which resemble closely the complex random grain structure of real NCs [146, 15]. A cubic region, typically several micrometers in each direction, is discretized using the VT technique, which starts with a set of seed points and determines the division of the simulation domain into distinct and non-overlapping polyhedra. Each cell grows from its seed point until reaching its nearest neighbors at which point a grain boundary forms. The grain boundary always bisects the line connecting adjacent seed points [9]. Once the VT is complete, it provides critical information about the morphology of the NC, including the size of each individual grain, the grain size distribution, their interconnectivity (who the neighbors of each grain are), as well as the area of the contact region between neighboring grains (see Fig. 3.6). The grain-size distribution is typically log-normal when starting from seed points uniformly distributed at random [50], but can be modified to follow other prescribed size distributions [49].

When grain boundaries are introduced, the pBTE solution becomes position-dependent along the direction of propagation of the phonon mode $(\mathrm{b}, \vec{q})$ because of scattering at the grain boundaries, which partially randomizes the direction of

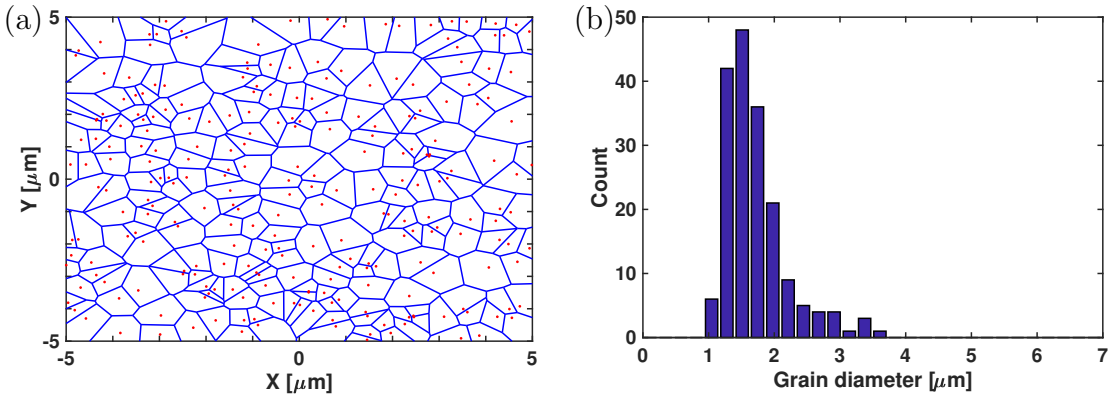

Figure 3.6. (a) A Voronoi diagram showing a 2-D slice of the constructed polyhedra and the grain boundaries. (b) The resulting grain size distribution.

propagation of the incoming phonons, and scattering inside the grain. At the grain boundary, phonons will interact with the atomic-scale roughness, and a fraction $p_{\vec{q}}$ of the incoming phonons will pass through unchanged (coherent or specular part) while the rest $(1 - p_{\vec{q}})$ will be absorbed by the boundary and re-emitted in a random direction (diffuse part). An effective scattering rate Γ_i^{GBR} due to the interactions of phonons with the GBR in the i-th grain can be defined by averaging the pBTE solution over the volume of each grain [30, 196] to obtain the final expression for the effective GBR scattering rate

$$\frac{1}{\tau_{\mathrm{b},i}^{\mathrm{GBR}}(\vec{q})} = \frac{\upsilon_{\mathrm{b}}(\vec{q})}{D_i} F_{\mathrm{b},i}(\vec{q}) \Bigg/ \left[1 - \frac{\Lambda_{\mathrm{b}}^{int.}(\vec{q})}{D_i} F_{\mathrm{b},i}(\vec{q})\right], \tag{3.3}$$

with D_i being the average distance a phonon travels inside the i-th grain. D_i can be related to the cubic root of the volume of the grain V_i, calculated for each grain from the VT, as $D_i = f_i S_i^{1/3}$, where f_i is the dimensionless form factor which captures the peculiarities of the specific geometry of each grain. For grains roughly approximated as disks, $f = \frac{8}{3\pi^{3/2}} \approx 0.48$. The parameter $F_{\mathrm{b},i}(\vec{q})$ fully captures the competition between GBR scattering at the boundaries of the grain and internal scattering inside the grain and is completely analogous to the one given previously for thin films,

with D_i replacing the film thickness L. The GBR scattering rate $1/\tau_{\mathrm{b},i}^{\mathrm{GBR}}(\vec{q})$ in Eq. (3.3) can be added to the rates due to intrinsic scattering processes internal to the grain to obtain the total scattering rate of mode $(\mathrm{b}, \vec{q})$ in grain i as $1/\tau_{\mathrm{b},i}(\vec{q}) = 1/\tau_{\mathrm{b}}^{int.}(\vec{q}) + 1/\tau_{\mathrm{b},i}^{\mathrm{GBR}}(\vec{q})$.

In the steady state, the net heat flux through the boundaries of each grain must be zero. Therefore, fluxes in and out of its neighbors and any external heating source Q_i applied to i-th grain must add up to zero. This assertion allows us to calculate the temperature T_i inside the i-th grain from

$$\sum_{j=\mathrm{n.n.}} G_{ij}\left(T_i - T_j\right) + S_i Q_i = 0, \tag{3.4}$$

with the summation index j running over all the grains that neighbor grain i. The thermal conductance G_{ij} between neighboring grains i and j is given by the usual expression

$$G_{ij} = \frac{\left[d_i \kappa_i(T_i) + d_j \kappa_j(T_j)\right] A_{ij}}{d_{ij}^2}. \tag{3.5}$$

with κ_i being the thermal conductivity of the i-th grain including the corresponding GBR scattering rate. Here, $d_{ij} = d_i + d_j$ is the distance between the centers of the two grains, i.e. the length of the straight line connecting the two centers, while d_i and d_j are the lengths of the line's segments inside the i-th and j-th grains, respectively. A_{ij} is the surface area of the grain contact region separating the two grains. This way, thermal resistor network is obtained, which can be solved iteratively [23], repeatedly updating the temperature of each grain based on the past values of the temperatures of its neighbors until convergence [23].

A heat sink is applied to the outer grains in the simulation domain so that the boundary condition on temperature outside of radius r_2 is kept constant. A heat source Q is applied to the grains inside a radius r_1 =1 μm around the center and is

allowed to diffuse. Q is determined, upon iteration of the temperature, to ensure the peak temperature in the center to be a few Kelvin ($\approx 1\%$) above the temperature of the heat sink. Convergence is reached when the total flux entering each grain equals the flux leaving it and the temperatures of all grains reach a constant value. After the temperature throughout the simulation domain reaches steady state (measured by the relative change in the temperature from one iteration to the next), the effective thermal conductivity is extracted using the below equation

$$\kappa_{\text{eff}} = \frac{Q \log(\frac{r_2}{r_1})}{2\pi(T_1 - T_2)}. \tag{3.6}$$

Effective thermal conductivity depends on the direction of heat propagation inside the NC, leading to strong directional anisotropy which arises from the local morphology of the grains, their sizes, and interconnections.

3.3.2 Results

We find that the lattice thermal conductivity decreases with average grain size, as shown in Fig. 3.7(b), analogous to the thickness dependence in thin films and SLs discussed in previous sections. The dependence is gradual and begins at grain sizes of several micrometers, and saturates towards the amorphous limit as grain size approaches the nanometer scale. Further reduction in thermal conductivity can be achieved by making a NC with grains comprising of different material/composition due to increased mass difference scattering. This trend is observed when a NC is made of intermixed Si and SiGe grains as shown in Fig. 3.7(a). The size dependence is gradual and begins at grain sizes of several micrometers, and saturates towards the amorphous limit as grain size approaches the nanometer scale, as seen in Fig. 3.7(c).

It is interesting to note that despite the heterogeneity and disorder in the NC structure, the crossover to purely diffusive transport occurs only when average grain diameter exceeds 10 μm, similar to what we observed in SiGe NWs. The conductivity

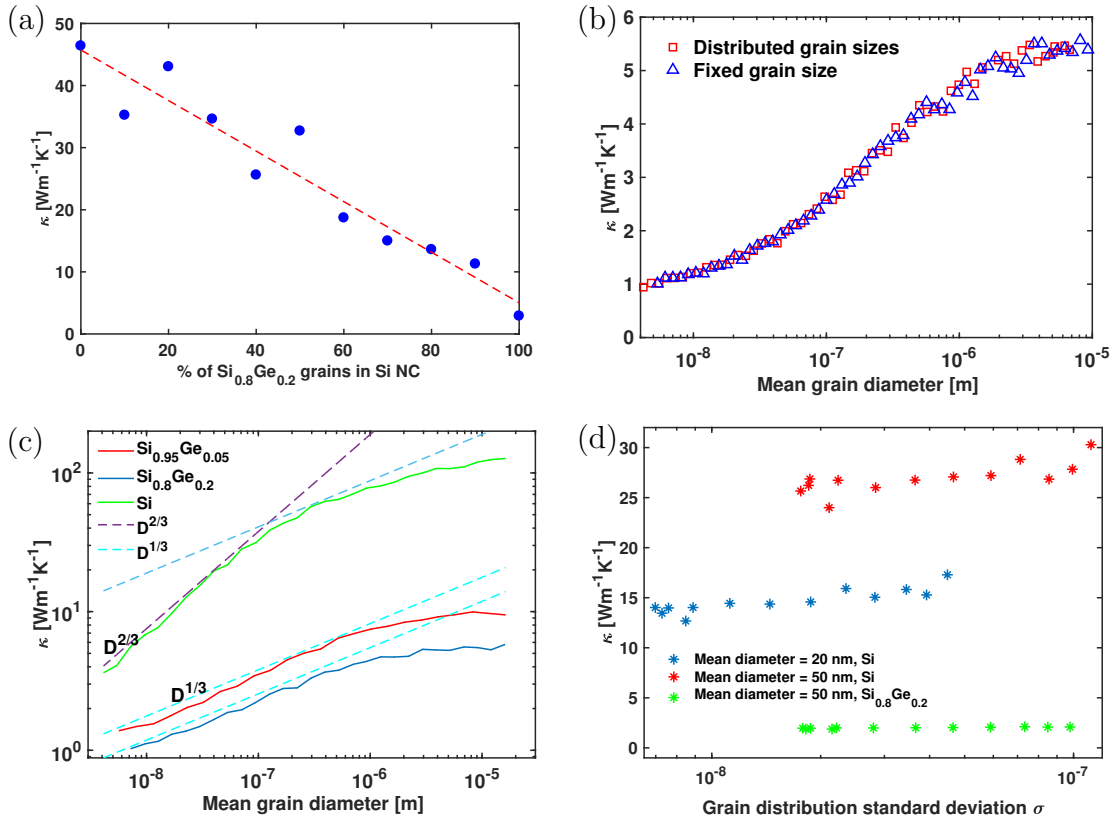

Figure 3.7. (a) Thermal conductivity of a $Si/Si_{0.8}Ge_{0.2}$ NC is plotted vs. the percentage of $Si_{0.8}Ge_{0.2}$ grains. (b) Thermal conductivity of a $Si_{0.8}Ge_{0.2}$ NC is plotted vs. average grain size for both uniform and randomly distributed grains. (c) Thermal conductivity of a $Si_{1-x}Ge_x$ NC with Ge composition of x=0, 0.05 and 0.2 is plotted vs. average grain size. Conductivity scales as $D^{2/3}$ in Si NC and $D^{1/3}$ in SiGe NCs indicating superdiffusive transport. (d) Thermal conductivity vs. standard deviation of the grain size distribution showing negligible effect of size distribution on conductivity. Adapted from Ref. [184, 182].

scales as $D^{2/3}$ in Si NC and $D^{1/3}$ in SiGe NCs, indicating a breakdown of Fourier's law and superdiffusive transport in both these systems. Even in the absence of alloy scattering, phonon transport in Si NCs is never predominantly ballistic due to the strong GBR scattering at the interface of each grain. However, the wide distribution of grain sizes (Fig. 3.6(b)), coupled with momentum-dependent GBR scattering that is more specular for long-wavelengths, suppresses mid- and high-frequency phonons while allowing low-frequency (long-wavelength) phonons with long MFPs to travel

several microns before being scattered internally, somewhat analogous to alloy scattering. This leads to superdiffusive transport even in non-alloy NCs.

On the other hand, the shape of the grain size distribution appears to have little effect, at least in alloy NCs, as both uniform and randomly distributed grain sizes lead to the same thermal conductivity for a given average grain size. We study the dependence on the grain size distribution in more detail by starting with a uniform distribution of seed points, which leads to a VT with uniform grains and a tight distribution of grain sizes. Next we increasingly perturb the initial seed points to reach a broader size distribution and compute the standard deviation of grain sizes from the mean and its corresponding thermal conductivity. Our finding that the shape of the distribution has modest effect is further confirmed by Fig. 3.7(d), which shows that varying the standard deviation of the grain size distribution in SiGe NCs has no effect on the thermal conductivity, after averaging over all transport directions. This trend is explained by the gradual dependence of the thermal conductivity of each grain on its size, caused by the competing alloy scattering in their interior. On the other hand, in Si NCs where the size dependence is more pronounced, we observe a gradual increase with as much as 20-30% variation, in agreement with a recent study [70].

Temperature dependent thermal conductivity in polycrystalline Si and SiGe

Phonon scattering at grain boundaries is the dominant mechanism for thermal conductivity reduction in polycrystalline materials. The most commonly used phenomenological Gray model approximates the phonon MFP to be independent of frequency and equates it to the average sample grain size ($\lambda_B \approx D_{avg}$) [18]. It has been observed that thermal conductivity in polycrystalline Si follows a T^2 trend at low temperatures [197] instead of the Debye T^3 trend seen in single crystal Si. Considering a frequency dependent MFP as described in Ref. [92], Wang et al. [197] show that

$\lambda_B \propto \omega^{-1}$ can explain the T^2 trend at low temperatures. This frequency dependence has been attributed to dislocation strain and a dislocation scattering model has been shown to be more fitting alternative in the low temperature limit.

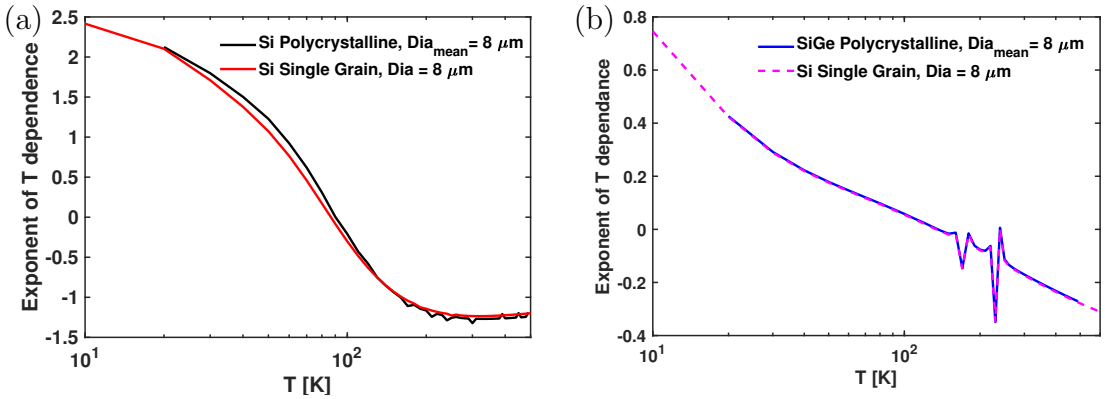

Figure 3.8. The exponent of temperature dependence vs. temperature for single and polycrystalline (a) Si and (b) SiGe with mean diameter of 8 μm.

Even in Si NWs the exponent of the temperature dependence of thermal conductivity has been observed to reduce with the width of the diameter [102] indicating that the T^2 trend is not specific to polycrystalline Si. This leads us to hypothesize that dislocation strain may not be an adequate explanation. As seen in the preliminary results (see Fig. 3.8), at low T the exponent of temperature depandance in Si is close to 2 and 1 in SiGe. Since conductivity scales as $D^{2/3}$ in Si NC $\lambda_B \approx D_{avg}^{2/3}$ and $\lambda_B \approx D_{avg}^{1/3}$ in SiGe, perhaps the exponent of length is affecting the temperature scaling and remains to be seen.

3.4 Conclusion

We employ the phonon Monte Carlo method to study thermal transport in SiGe NWs, and find that thermal conductivity scales as $L^{1/3}$ over a broad range of lengths and conclude that in SiGe NWs the direct ballistic-to-diffusive crossover picture is incomplete and should be augmented by superdiffusion in the broad intermediate

range of NW length from 10 nm to 10 μm. Alloy nanostructures exhibit novel heat dynamics and can be used as a unique fundamental platform to study the breakdown of Fourier's law. The superdiffusive transport is brought on by Lévy-like heavy-tailed distribution of phonon flights, and causes a length dependent thermal conductivity with $\kappa \propto L^{1/3}$ over a broad range of lengths extending from 10 nm all the way to 10 μm, far exceeding phonon MFP or NW diameter. Thus, lattice conductivity is length-tunable even in NWs several microns long, with potential applications to reducing thermal conductivity and thus increasing TE figure-of-merit in alloy NWs with sub-ten-micron lengths.

We use a Voronoi tessellation model to treat the complex heterogenous structure of nanocomposites and find that reducing grain size into the nanometer regime or adding nanoscale grains into the bulk matrix is the most effective way to reduce thermal conductivity, with the additional benefit of lower cost and simpler fabrication than SLs. At such scales, energy filtering effects are expected to lead to a boost, rather than a reduction, in the electronic PF [213]. In addition, our detailed model based on the Vorronoi tesselation and the pBTE solution in each grain captures the grain structure of the nanocomposite and its impact on the thermal conductivity much more directly than empirical approaches such as the effective medium approximation (EMA) [5]. We show that NCs can be optimized to improve ZT by reducing the thermal conductivity by a combination of approaches including scattering of phonons from the interfaces between nanoscale grains, alloys of varying composition, and roughness. Thermal conductivity decreases with average grain size, similar to the thickness dependence in superlattices and scales as $D^{2/3}$ in Si NC and $D^{1/3}$ in SiGe NCs, indicating a breakdown of Fourier's law in both these systems. The wide distribution of grain sizes coupled with momentum-dependent GBR scattering, suppresses mid- and high-frequency phonons while allowing low-frequency phonons with long MFPs to travel several microns before being scattered internally, somewhat

analogous to alloy scattering which leads to superdiffusive transport even in non-alloy NCs.

CHAPTER 4

THERMOELECTRIC PROPERTIES OF SEMICONDUCTING POLYMERS

Doping polymers in order to improve the electrical conductivity has the undesirable effect of significantly reducing their Seebeck coefficient to a range in the order of tens of μVK^{-1} [170]. Therefore, a long-standing problem in TEs has been to effectively decouple electrical conductivity from the Seebeck coefficient and control them independently. Polymer systems do not possess the continuous order found in their inorganic counterparts; they are inherently disordered and charge transport can be described as a hopping process [142, 21, 172]. One of the most prominent phenomenological models is based on variable-range hopping (VRH) of electrons between the polymer chains and called the Gaussian Disorder Model (GDM) [21]. This model has been widely used to study charge transport in polymers and polymer based devices [16, 141, 65, 52, 185]. More recently, charge transport in organic systems have also been analyzed by combining ab initio calculations with classical molecular dynamics (MD) and kinetic Monte Carlo techniques [90, 119, 191]. However, the TE performance of these materials and the combined effects of disorder and correlation on TE transport, especially within a hopping model, has not been fully explored. In the work by Mendels and Tessler [132], positional disorder was implemented as spatial variations without including the variation in orbital overlap. Most studies based on the GDM and its variants compute the hopping rate between adjacent sites using the Miller-Abrahams rate equation. We present a comparison of the Miller-Abrahams hopping rate with the Marcus hopping rate, which considers the additional energy penalty to hopping due to polaronic binding. Also, there have been few studies to

determine the Lorenz number and its relationship with Seebeck coefficient in semiconducting polymers. Experimental studies on iodine-doped polyacetylene [133] and PEDOT:PSS [108] have shown that the Wiedemann-Franz law holds and the Lorenz number is close to the Sommerfeld value. However, Weathers et al. [199] showed the electronic contribution to thermal conductivity was higher than previously reported, consistent with a large Lorenz number, while Lu et al. [117] reported a large deviation from the Wiedemann-Franz law under the effect of temperature, carrier concentration, energetic disorder, and electric field. In this chapter We explore the effect of various manifestations of disorder, including positional disorder, energetic disorder, as well as correlation in both energy and wave-function overlap distributions, on the electrical conductivity, Seebeck coefficient and Lorenz number.

4.1 Polymer theory

Conjugated polymers are positionally disordered systems in which the polymer chains typically interact through weak van der Waals (vdW) interactions. The charge transport within a chain occurs through the covalent framework, and between chains the interactions is through the pi-pi orbitals orthogonal to the chain axis. The displacement of the states about the lattice points causes disruption in the overlap of the pi orbital wave functions termed 'positional disorder' [16]. The interactions between orbitals of adjacent segments are very weak, and the strong electron-phonon coupling in these materials can destroy the coherence between neighboring sites, which causes electrons to become localized to that region and reduces the delocalization range. The decay parameter γ^{-1} of the localized electron wave function, or the localization length, is typically 1 Å$<a\gamma^{-1}<$5 Å[154]. The vdW and dipole-dipole interactions cause variation in the electrostatic environment [21]; furthermore, the dopant molecules Coulombically interact with the carriers localized to a site, thus broadening the density of states (DOS) [11]; this is called 'energetic disorder' and shown on the

left of Fig. 4.1. The site energies are described by a Gaussian distribution of width Γ_E [21, 16], and the DOS is given as

$$g(E) = \frac{1}{\sqrt{2\pi\Gamma_E^2}} exp\left(-\frac{E^2}{2\Gamma_E^2}\right), \tag{4.1}$$

where Γ_E accounts for the degree of energetic disorder in the structure. Positional disorder is modeled as random variations in the wave function overlap parameter γ between two sites, as depicted schematically in Fig. 4.1. Hence, $\gamma_{ij} = \gamma_i + \gamma_j$, where γ_i and γ_j are the site specific contributions obtained from a Gaussian distribution of width Σ_{ij}, where the width Σ_{ij} accounts for the variation in the electronic wave function coupling due to variation of both the intersite distance and mutual orientation of molecules [21].

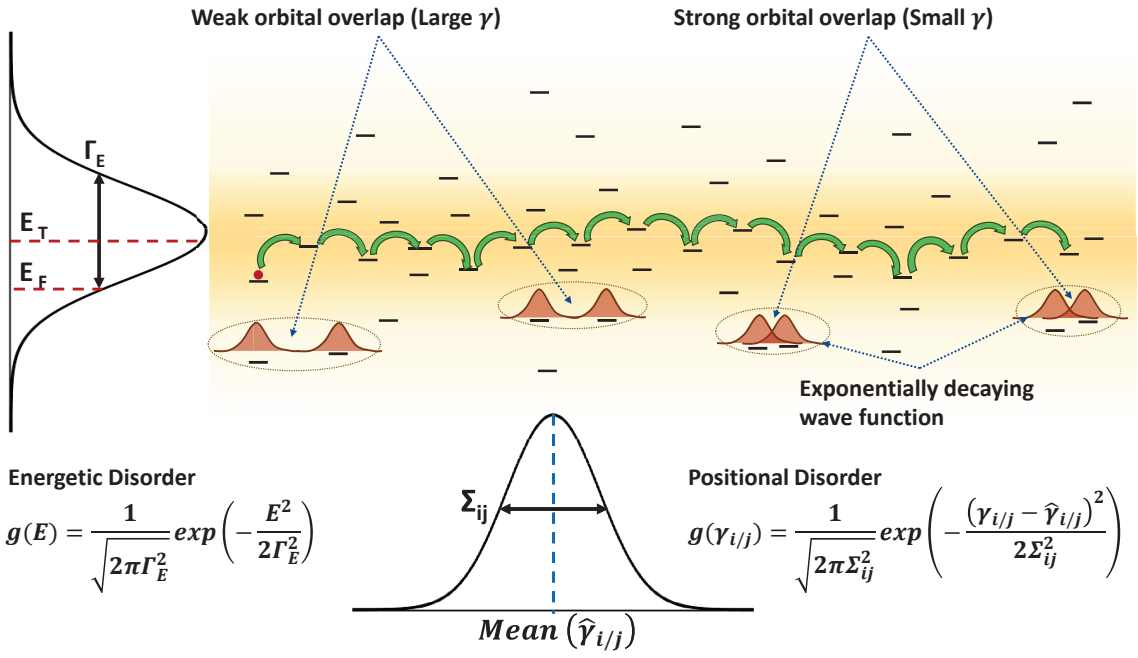

Figure 4.1. Schematic representation of the carrier hopping process, showing overlap, energetic, and positional disorder. Taken from Ref. [183].

4.2 Phonon-assisted hopping model

In inorganic semiconductors, ordered crystal lattice with relatively weak electron-phonon coupling leads to a band transport where the interaction between electrons and lattice vibrations (phonons) can be described by perturbation theory. In contrast, polymers do not have long-range periodicity of the atomic structure; electrons are localized and transport is described as a hopping process. The hopping transport process is dependent on temperature [118], molecular structure, and inter-molecular packing of the material [150]. Carriers hop from one localized state to another through three possibilities: the electron hops to another state of equal energy by a tunneling process, it hops to a lower energy site while the difference in energy is compensated by the emission of a phonon, or it hops to a state of higher energy and the additional energy required is provided by absorbing a phonon, as illustrated by the green arrows in Fig. 4.1.

Our model describes the probability that a site is occupied by an electron in terms of Pauli's master equation (PME), which is a differential equation that describes the time rate of change of each site occupation probability due to electrons hopping into and out of it. In the steady-state, the time rate of change of occupation probability will go to zero and PME is given as a sum over all possible transitions into and out of a site

$$\frac{dp_i}{dt} = 0 = \sum_j [W_{ij} p_i (1 - p_j) - W_{ji} p_j (1 - p_i)], \tag{4.2}$$

where p_i is the occupation probability of a site i and W_{ij} is the hopping transition rate from site i to j, summed over the neighboring sites j. The PME is solved for the site occupations using a non-linear iterative solver as described in Methods, after which relevant quantities like mobility and current can be calculated [185]. The initial site occupation is given by the equilibrium Fermi-Dirac distribution $p_i^0 = \left[\exp\left(\frac{E_i - E_F}{k_B T}\right) + 1\right]^{-1}$.

The general hopping rate from site i to site j is given as [53]

$$\begin{aligned} W_{ij} =& \frac{\pi}{\hbar} \sum_{q} \mid M_{ij,q} \mid^2 \left[\left(N\left(\omega_q\right) + 1 \right) \rho_{FCWT}\left(\Delta E_{ij} + \hbar\omega_q \right) \right] \\ &+ N\left[\left(\omega_q\right) \rho_{FCWT}\left(\Delta E_{ij} - \hbar\omega_q \right) \right], \end{aligned} \tag{4.3}$$

where $\rho_{FCTW}\left(\Delta E\right)$ is a function that depends on the Franck-Condon factors, $\omega_q$is the energy of the phonon mode q, N_q is the number of phonons in that mode, given by the Bose-Einstein distribution $N(\omega_q) = \left[\exp\left(\frac{\hbar\omega_q}{k_B T}\right) - 1\right]^{-1}$ where T is the absolute temperature. The $M_{ij,q}$ is the phonon-electron coupling constant between sites i and j due to phonon mode q, $\Delta E_{ij} = E_j - E_i - eF\Delta R_{ij,x}$ where E_i and E_j are the energies of sites i and j and F is the externally applied electric field. In the limit where there are no phonons with different equilibrium positions in sites i and j, such that only transitions $q = q'$ can take place, the function ρ_{FCTW} becomes a Dirac delta function and we obtain [191]

$$W_{ij} = \frac{\pi}{\hbar} \sum_{q} \mid M_{ij,q} \mid^2 \left[\left(N\left(\omega_q\right) + 1 \right) \delta\left(\Delta E_{ij} + \hbar\omega_q \right) + N\left(\omega_q\right) \delta\left(\Delta E_{ij} - \hbar\omega_q \right) \right]. \tag{4.4}$$

Calculation of these rates can be computationally challenging as it requires that we first calculate the electronic wave functions, phonon modes, and the electron-phonon coupling constants. We can simplify them further by approximating M_i to be proportional to the overlap of the wave functions $\gamma_{ij} = \int d^3r \mid \psi_i(r) \mid \dot{\mid}\psi_j(r) \mid$, which then yields [137]

$$W_{ij} = \beta^2 \gamma_{ij}^2 \left[N\left(\Delta E_{ij}\right) + \frac{1}{2} \pm \frac{1}{2} \right] D_{ph}\left(\Delta E_{ij}\right) / \Delta E_{ij} \tag{4.5}$$

where β is the coupling constant between electron-phonon coupling constants and wave function overlap, and $D_{ph}(E)$ is the phonon DOS normalized such that $\int_0^\infty D_{ph}(E)dE = 1$. For hops upwards in energy ($E_j > E_i$) by absorption of a phonon, it is $-\frac{1}{2}$ and

for downward hops with the emission of a phonon, it is $+\frac{1}{2}$ in the rate equation. Further simplification can be made by assuming that the wave function overlap decays exponentially with distance, and if we ignore the energy dependence we get the Miller-Abrahams rate equation [134],

$$W_{ij} = v_0 exp(-2\gamma_{ij} R_{ij}) \left[N\left(\Delta E_{ij}\right) + \frac{1}{2} \pm \frac{1}{2} \right] \tag{4.6}$$

where v_0 is the attempt-to-escape frequency and ΔR_{ij} is the distance between the sites.

The Miller-Abrahams rate equation considers only bare charge transport. Since the phonon-electron coupling is strong in organic polymers, it is important to consider the affect of polaron transport, and analyze its effect on TE properties. As a polaron moves through different states, there is deformation of the molecule as the polaron arrives and leaves, and the energy associated with the relaxation of the molecule upon charge transfer is called the binding or reorganization energy. Using $\rho_{FCTW}\left(\Delta E\right) = \sqrt{\frac{1}{4\pi E_0 k_B T}} exp\left[-\frac{(\Delta E + E_0)^2}{4E_0 k_B T}\right]$ [53], where E_0 is the reorganization energy in Eq. 4.3, and further simplifying we get

$$W_{ij} = v_0 \sqrt{\frac{1}{4\pi E_0 k_B T}} exp\left(-2\gamma_{ij} R_{ij}\right) exp\left[-\frac{\left(-\Delta E_{ij} + E_0\right)^2}{4E_0 k_b T}\right], \tag{4.7}$$

which is the Marcus rate equation [123]. It is important to note that we can also obtain the Miller-Abrahams rate by taking the limit $E_0 \to 0$ in the Marcus rate.

The non-linear PME is solved using these rates on a 35×25×25 lattice of sites with an average distance between adjacent lattice points a=1 nm. The number of 'neighbors'depends on the hopping distance and lattice described; we have a cubic lattice and consider up to the third-nearest neighbor, which implies hopping to the nearest 26 sites and maximum hopping distance of $\sqrt{3a}$. The electronic wavefunctions

are localized so their overlap has an exponential decay with distance; hence the probability of hopping to neighbors further than the third-nearest neighbor is very small and does not contribute as significantly to transport. The $(1 - p_{i/j})$ factor accounts for the exclusion principle requiring that only one carrier is occupying a particular site, due to the high Coulomb penalty for the presence of two charges on one site. All simulations are run under low-field conditions with field F=10^6 Vm^{-1}, attempt to jump frequency v_0=10^{12} s^{-1}, energy distribution width Γ_E=3k_BT, overlap γ=3 and T=300 K unless stated otherwise. We obtain the current density J by a summation over all the carriers in the direction of the applied field [141] (here the x direction)

$$J = \frac{e}{a^3 N} \sum_{i,j} W_{ij} p_i (1 - p_j) R_{ij,x} \tag{4.8}$$

where e is the electron charge, and then for electrical conductivity we take $\sigma = J/F$.

The Seebeck coefficient (or thermopower) is the voltage built up in response to an applied temperature gradient, given by $\alpha = -\frac{\Delta V}{\Delta T}|_{I=0}$, as carriers that respond to an electric field can also be elicited by a temperature gradient. While each carrier carries a charge e, it also carries an 'excess' energy $E - E_F$ [217, 81], and the Seebeck coefficient can be calculated as the average carrier energy

$$\alpha = \frac{(E_F - E_T)}{eT} \tag{4.9}$$

where E_T is the average transport energy, calculated from [132]

$$E_T = < E_i > = \frac{\sum_{i,j} E_i W_{ij} p_i (1 - p_j) R_{ij,x}}{\sum_{i,j} W_{ij} p_i (1 - p_j) R_{ij,x}}, \tag{4.10}$$

where the brackets $< . >$ denote an average over the sites. The Lorenz number is related to the open-circuit electronic thermal conductivity [194]

$$\kappa_o = \frac{\sum_{i,j} (E_i - E_F)^2 W_{ij} p_i (1 - p_j) R_{ij,x}}{eT^2} \tag{4.11}$$

through $L = \kappa_o/\sigma T - \alpha^2$ and thus can be analogously obtained from the variance of the excess energy [194]

$$L = \left\langle \left(\frac{E_i - E_F}{eT} \right)^2 \right\rangle - \left\langle \left(\frac{E_i - E_F}{eT} \right) \right\rangle^2 . \tag{4.12}$$

4.2.1 Solving the non-linear PME

We solve the non-linear PME using a standard iterative non-linear solver. First, we cast the PME as zero-finding for a system of equations $F_i(\mathbf{p}) = \sum_j [W_{ij} p_i (1 - p_j) - W_{ji} p_j (1 - p_i)] = 0$, which can be written in terms of the in- and out-scattering as $F_i(\mathbf{p}) = p_i S_{out}(\mathbf{p}) - (1 - p_i) S_{in}(\mathbf{p})$ with $S_{out}(\mathbf{p}) = \sum_j W_{ij}(1 - p_j)$ being the out-scattering term and $S_{in}(\mathbf{p}) = \sum_j W_{ji} p_j$ being the in-scattering. The expression for $F_i(\mathbf{p})$ is nonlinear because both in- and out-scattering terms depend on the unknown $\mathbf{p}$. Previous studies typically rearranged this equation to obtain a fixed point iteration for the p_i such as $p_i^{n+1} = S_{in}(\mathbf{p}^n) / [S_{in}(\mathbf{p}^n) + S_{out}(\mathbf{p}^n)]$ with the initial condition p_i^0 being the equilibrium Fermi-Dirac distribution given earlier. However, a fixed point iteration can stall, resulting in poor convergence for some cases. For this reason, we follow the same fixed-point iteration procedure here for the first few iterations and then use the resulting estimate of p_i as an initial guess in the next step where we numerically solve for the zero of $F_i(\mathbf{p})$. Rather than solving for the site occupancies p_i, we solve for their deviation away from equilibrium $\Delta p_i = p_i - p_i^0$. Combining this with Eq. 4.2 and simplifying for Δp_i, we get $F_i(\mathbf{p}) = \Delta p_i S_{out}(\mathbf{p}) - (1 - p_i^0) S_{in}(\mathbf{p}) = 0$. We arrange the $35 \times 25 \times 25$ array of Δp_i's into a column vector $\mathbf{p}$ and compute the Jacobian matrix of derivatives of F_i with respect to p_j as $J_{ij} = dF_i/dp_j = -W_{ij} p_i - W_{ji}(1 - p_i)$. Then we apply the Levenberg-Marquardt algorithm [145], as implemented in MATLAB's fsolve function, with the known Jacobian matrix, which requires a linear solve at each iteration but typically converges in a few iterations due to its high rate of convergence. The linear solver is a preconditioned Conjugate Gradients algorithm with a banded preconditioner based on an incomplete Cholesky factorization.

4.3 Results and discussion

First, we consider the impact of doping and overlap between neighboring sites on TE properties. Fig. 4.2(a) shows the dependence of electrical conductivity and Seebeck coefficient on the carrier density. We increase the carrier density by moving the Fermi level E_F closer to the center of the Gaussian energy distribution, analogous to electrochemical doping of polymers. We can clearly see the inverse relation that exists between these parameters and the charge density, and the challenge it poses to obtaining high PF values. At low concentration, the Seebeck is in the range of

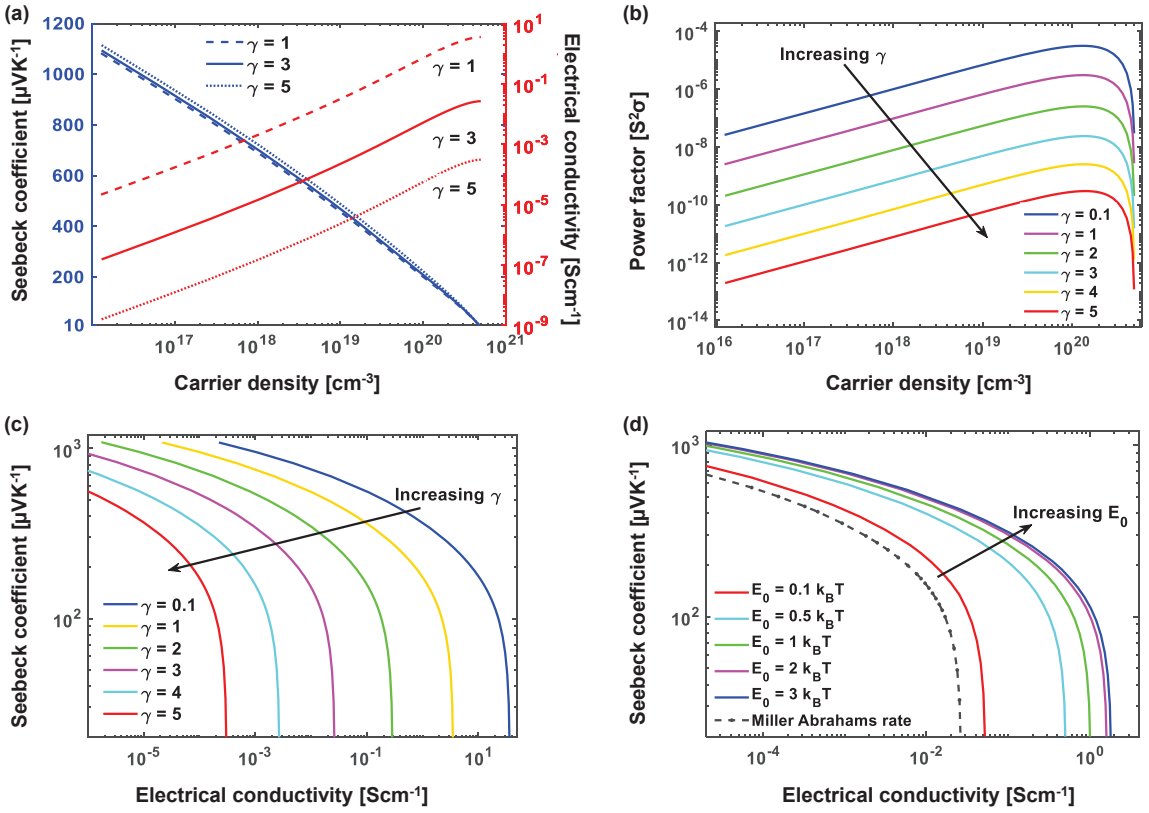

Figure 4.2. (a) Seebeck coefficient, electrical conductivity and (b) PF as a function of carrier density at different overlap parameter values. We note than the highest PF is obtained at a carrier density of 2×10^{20} cm^{-3}, corresponding to 20% of sites being occupied. (c) α vs. σ showing the increase in electrical conductivity and Seebeck coefficient with stronger electronic orbital overlap. (d) Comparison of the α vs. σ for hopping rates computed using Miller-Abrahams and Marcus rate equations. Taken from Ref. [183].

hundreds of μVK^{-1}, but increasing the carrier concentration causes it to decrease to a few tens of μVK^{-1}. However, the electrical conductivity has an appreciable value only at high concentrations and the highest PF is achieved at a carrier concentration of 2×10^{20} cm^{-3}, shown in Fig. 4.2(b), which corresponds to 20% of sites being occupied by carriers.

We plot α vs. σ for different values of the overlap parameter in Fig. 4.2(c), where each point on the curve represents the parameters computed at different carrier densities. The advantage of such a plot is that one can readily see the effect of both carrier density and overlap parameter on Seebeck and electrical conductivity, wherein a curve bulging more towards the top right indicates higher PF. We find that electrical conductivity is strongly dependent on the overlap parameter whereas it has negligible effect on the Seebeck coefficient, as seen in Fig. 4.2(a). A smaller value of the overlap parameter, which implies stronger electronic orbital overlap between adjacent sites, is favorable for the hopping process, and thus increases the electrical conductivity. In Fig. 4.2(d) we compare the Seebeck and electrical conductivity computed from Miller-Abrahams and Marcus rate equations. The curve shifts right for higher values of reorganization energy E_0, showing improved electrical conductivity with increasing polaronic binding, while as we decrease E_0 and approach the limit $E_0 \to 0$, it falls back to the curve obtained from Miller-Abrahams rate.

4.3.1 Energetic and positional disorder

Next, we explore the effect of varying degrees of energetic and positional disorder in the system on its TE performance. A larger variation of the Gaussian energy distribution (Γ_E), leads to a decrease in electrical conductivity and small increase in Seebeck (see Fig. 4.3(a)). Decreasing the width of the energy distribution, meaning a more sharply peaked DOS, lowers the spread in the site energies, leading to a smaller difference ΔE_{ij} between energies of neighboring sites. A favorable network of

nearly equal energy sites thus forms, alleviating the required thermal assistance by absorption of phonons. It is widely thought, based on the work on Mahan and Sofo [120] that a narrower DOS leads to a higher TE figure-of-merit, with a delta-function DOS being ideal.

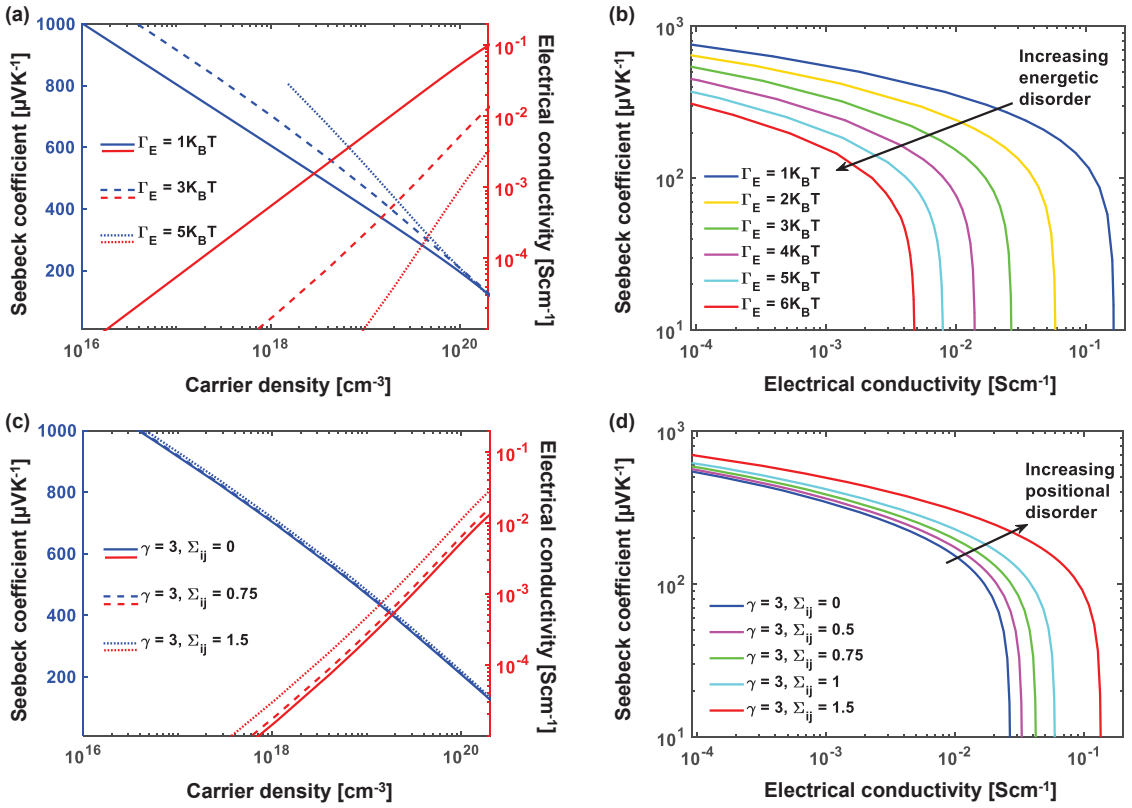

Figure 4.3. Seebeck coefficient and electrical conductivity vs. carrier density for varying widths of (a) Gaussian energy distribution (energetic disorder), and (c) distribution of the overlap parameter (positional disorder). α vs. σ with varying (b) energetic and (d) positional disorder. We find that smaller energetic disorder and larger positional disorder lead to better TE performance of a material. Taken from Ref. [183].

Combining Eqns. 4.9 and 4.10 we see that the Seebeck coefficient can be viewed as the average "excess" (away from the Fermi level) entropy per carrier $\alpha =< E_F - E_i > /eT$. Increasing energetic disorder broadens the DOS and makes it flatter but does not affect the shape of the Fermi-Dirac distribution function. Consequently, there are

nearly as many states near the DOS peak as there are away from it, which pushes the average E_i away from the center of the DOS. Reducing energetic disorder has the opposite effect: the DOS becomes more sharply peaked with many more states near the peak, resulting in an average E_i closer to the middle of the DOS. If we fix the Fermi level E_F and compare, then larger energetic disorder would imply smaller Seebeck and vice versa. However, if we compare while keeping the carrier concentration $n(E_F, T) = \int g(E)p_i^0(E,T)dE$ constant, then the opposite trend emerges: increasing energetic disorder pushes the Fermi level away from the center of the DOS, countering the change in E_i and thus slightly increasing the Seebeck, shown on the left axis in Fig. 4.3(a). Based on the Mott formula for Seebeck coefficient we have [77, 74]

$$\alpha = -(\pi^2/3)(k^2T/q)\frac{\partial}{\partial E} ln[\sigma(E)]|_{E=E_F}, \tag{4.13}$$

using the Einstein relation for $\sigma(T, E)$ we get [74],

$$\alpha \propto \frac{dln[g(E)]}{dE} + g\frac{d[\mu(E)]}{dn}. \tag{4.14}$$

When $\mu(E)$ is only weakly varying, the second term is small and in case of GDM and Gaussian DOS, the first term becomes $-E_F/\Gamma_E^2$. Overall, Fig. 4.3(b) shows that the effect of disorder on electrical conductivity is more pronounced and reducing energetic disorder leads to higher TE PFs.

Next, we vary the amount of positional disorder in the system by varying the width of the Gaussian overlap distribution (Σ_{ij}). Positional disorder primarily affects the electrical conductivity, while the Seebeck is mostly sensitive to the distribution of energies (DOS) and less on their relative positions (Fig. 4.3(c)). The electrical conductivity increases with increasing positional disorder, and shifts the curves right in Fig. 4.3(d), signifying higher PF values. This is due to the increase in overlap of approximately half the near-neighboring sites in the system, which aids the for-

mation of conduction paths, consequently increasing the probability of hopping into higher-energy sites. Thus, larger positional disorder but smaller energetic disorder are desirable for polymer TEs.

4.3.2 Energetic and positional correlation

In the GDM, site energies are distributed independently with no correlations occurring over any length scale. Nonetheless, spatial fluctuations and corresponding correlation of energy arising from charge dipole interactions and molecular density fluctuations should affect transport [140]. It has been shown that energy correlation leads to Poole-Frenkel field dependence of mobility over a wide range of fields [57, 140]. Spatial correlation in the energetic landscape, modeled by averaging energy over neighboring sites, was also shown to lower the transport energy and decrease the Seebeck coefficient [132]. However, the impact of correlation length has not been firmly established in the context of TE properties, nor has the effect of correlation on positional disorder through the overlap parameter been studied.

To further explore the effect of long-range correlation on TE parameters, we use an inverse fast Fourier transform (IFFT) method [203, 26, 148] to generate autocorrelated distributions of energy and overlap parameter with a specific correlation length. We start from the standard exponential form of the autocorrelation function of the site energies $\mathcal{C}(R_{ij}) =< E(R_i)E(R_j) >= \Gamma_E^2 \exp\left(-\sqrt{2}R_{ij}/L_{corr}\right)$ where $R_{i/j}$ are the positions of the i/j'th sites, R_{ij} is the distance between the two sites, and L_{corr} is the correlation length. The spectral density is Fourier transform of the autocorrelation function $|\mathcal{S}|^2 = \mathcal{F}(\mathcal{C})$. The autocorrelated distribution is obtained by multiplying a random phase ($e^{i\phi}$), having angle ϕ uniformly distributed between (0, 2π), with the square root of spectral density and then taking the inverse Fourier transform [127]

$$E = \mathcal{F}^{-1}\left(|\mathcal{S}|e^{i\phi}\right). \tag{4.15}$$

The same procedure is applied to obtain a spatially-correlated distribution of overlap parameters γ. This method allows us to vary the correlation length independently of the variance. Fig. 4.4(a) shows the α vs. σ for uncorrelated and correlated energy distribution with different correlation lengths and fixed Γ_E=3 and 6 k_BT. The same is shown in Fig. 4.4(b) for correlation in overlap distribution. We find that energy correlation has virtually no effect on the TE parameters, while the curve shifts left with increasing correlation length for the overlap distribution. We conclude that smaller correlation between sites leads to better electrical conductivity but the Seebeck remains largely unaffected, thus effectively decoupling these parameters.

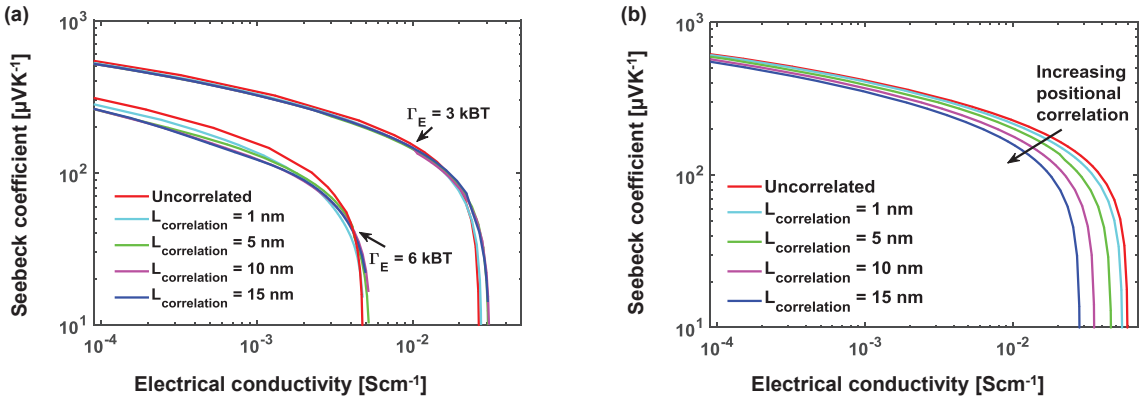

Figure 4.4. α vs. σ for different degrees of correlation in the (a) Gaussian energy distribution, (b) distribution of the overlap parameter. We find that correlation in energy distribution has negligible affect, whereas a modest improvement in electrical conductivity is observed with smaller correlation in the orbital overlap distribution. Taken from Ref. [183].

4.3.3 Comparison to experimental data

We compare our model to experimental data from several measurements, including three PDPP4T samples (Fig. 4.5(a)) chemically doped with iodine and measured by our collaborators in the Chemistry department and described in Ref. [183]. The PEDOT:Tos data was obtained from Ref. [25] (Fig. 4.5(b)) and P3HT data from

Ref. [79] (Fig. 4.5(c)). Our results are in good agreement with the data and the fit is obtained by varying relevant parameters including overlap, average distance between adjacent lattice points, energetic, and positional disorder. The data for PEDOT:Tos reported to have a ZT$\sim$0.25 obtained from Ref. [25], is a close fit to the γ=0.1 and Γ_E=2.25 k_BT curve, implying stronger electronic orbital overlap between adjacent sites and small energetic disorder, which explains the exceptional electrical conductivity observed in these samples beyond what is obtained from γ=3, a value commonly used in calculations.

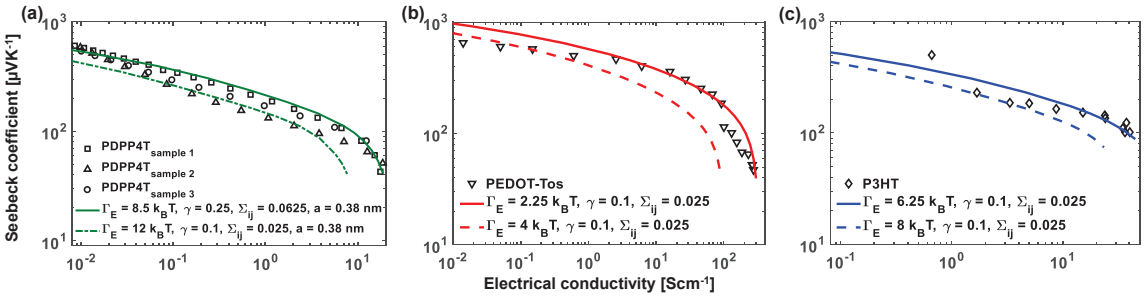

Figure 4.5. Comparison of our model to experimental data from (a) PDPP4T samples from Ref. [183], (b) PEDOT:Tos from Ref. [25], and (c) P3HT sample from Ref. [79], showing good agreement across multiple data sets. We plot two curves (solid and dashed lines) on the top and botton of the experimental data to show that the values would fall between these two extremes and account for possible error bars. Taken from Ref. [183].

4.3.4 Diverging Lorenz number

Lastly, we turn our attention to the Lorenz number. In most materials, the Lorenz number ranges from a value close to the Sommerfeld value found in metals and degenerate semiconductors $L_0 = \pi^2/3(k_B/e)^2 = 2.44 \times 10^{-8}$ WΩ K^{-2} [168] decreasing to the value $L_0 = 2(k_B/e)^2 = 1.49 \times 10^{-8}$ WΩ K^{-2} found in single-parabolic-band materials when acoustic phonon scattering is dominant [173]. It has been shown that a first-order correction to the degenerate limit $L = 1.45 + exp(-|\alpha|/116)$ (where L

is in 10^{-8} WΩK^{-2} and α in μVK^{-1}) is a good approximation and holds across all known band semiconductors [89]. In contrast, we see an opposite trend in organic semiconductors, where L increases with Seebeck coefficient as shown in Fig. 4.6. Increasing the overlap, positional disorder and polaronic binding energy increases the value of Lorenz number further, but the largest impact is seen with energetic disorder when Γ_E is increased from 3 to 5 k$_B$T. Experimental data also confirm L is significantly larger than L_0 in PEDOT:Tos [25].In the limit when electronic thermal conductivity dominates ($\kappa_e > \kappa_l$), the ZT goes to $ZT = \alpha^2/L$; therefore, a simultaneous increase in α and L could have a negative impact on ZT and hence design of effective TE materials with polymers requires consideration of the Lorentz number as well, carefully balancing the roles of disorder and correlation.

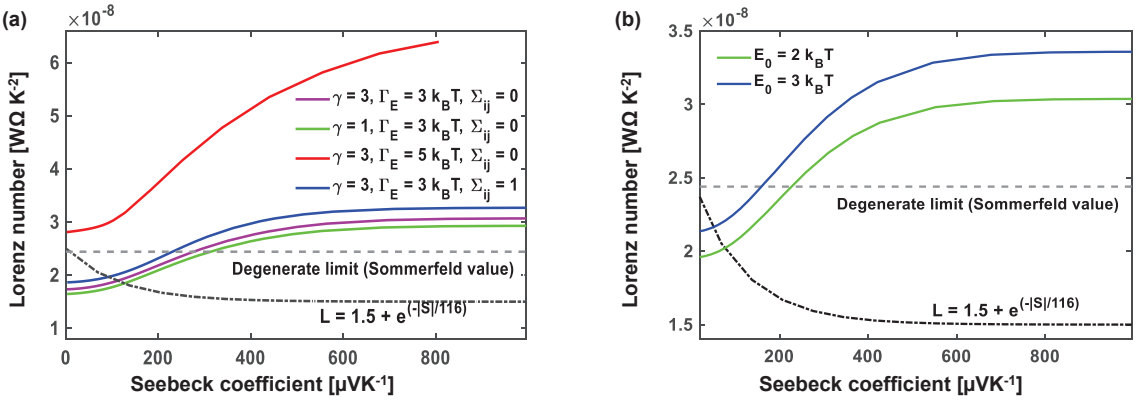

Figure 4.6. Lorentz number vs. Seebeck coefficient showing the increasing deviation from the Sommerfeld value with increasing (a) overlap parameter, energetic and positional disorder, and (b) polaronic binding energy (E_0). Taken from Ref. [183].

4.4 Conclusion

Polymers, with their inherently low thermal conductivity and low cost of manufacturing, are a promising choice for TE applications. However, for commercial success the ZT of these materials needs to be improved further. We study the ef-

fects of disorder and correlation on their TE properties using a hopping transport model. We find that positional disorder leads to a moderate increase in the electrical conductivity whereas the Seebeck remains unaffected. Energetic disorder has an adverse affect on electrical conductivity but leads to a moderate increase in Seebeck coefficient at lower doping concentrations. Consequently, positional correlation primarily affects electrical conductivity, while correlating the nearby site energies has no effect on the TE properties. We conclude that controlling energetic and positional disorder would allow us to decouple electrical conductivity and the Seebeck coefficient. Minimizing energetic disorder and correlation while increasing positional disorder results in a higher TE PF. Our results also show that the Lorenz number increases with the Seebeck coefficient, more so with increasing disorder, in contrast to the universal trend observed across all materials exhibiting band transport. We find that numerical transport models can play a key role in predicting the optimum structural characteristics and aid the design and development of novel materials for TE applications.

CHAPTER 5

CHARGE TRANSPORT DYNAMICS IN DOPED POLYMERS

As we saw in the previous chapter, doping polymers to improve the electrical conductivity negatively impacts the Seebeck coefficient which requires a trade-off between the two, which implies that precise control of doping along with minimizing energetic disorder and correlation while increasing positional disorder is critical for obtaining the maximum PF. A right shift in the α vs. σ curve signifies higher PF, however, it is of vital importance to understand the shape of the curve or the relationship between Seebeck and electrical conductivity for effective design of organic TEs. Previous studies have shown empirical relationships between Seebeck and electrical conductivity ($\alpha \propto \sigma^{-1/4}, \alpha \propto \ln \sigma$) [80, 62, 206], but their origin and physical implications are still uncertain. Recently, Kang and Snyder proposed a generalized two-parameter charge transport model for conducting polymers [81]. They fit the variation in Seebeck coefficient as a function of electrical conductivity to their model to obtain a value for a transport parameter, s, and found most polymers to follow a shallow α vs. σ trend. The exception was PEDOT:Tos, which exhibited a sharper curvature, leading Kang and Snyder to conclude that the shape of the α vs. σ curve is unique to the polymer.

The Kang and Snyder charge transport model is based on Fritzsche's general equation [55]

$$\alpha = \left(\frac{k_B}{q}\right) \int \left(\frac{E - E_F}{k_B T}\right) \frac{\sigma(E)}{\sigma} \tag{5.1}$$

and

$$\sigma = \int \sigma(E)dE = q \int g(E)\mu(E)f(E)[1 - f(E)]dE \tag{5.2}$$

where f(E) is the fermi distribution and $\mu(E)$ is the charge carrier mobility. This approach is more widely applicable than the simpler Mott formula (Eq. 4.14) and has the advantage of connecting α to the average entropy per carrier. Since these expressions are valid (neglecting correlation effects) across all doping levels regardless of the conduction mechanism or the semiconductor's crystalline, semi-crystalline, or amorphous nature, they support numerous mechanisms of conduction in disordered semiconductors [118, 162, 139], including hopping models based on the Miller-Abrahams and Marcus jump rates discussed in Ch. 4, that add to our physical explanation of charge transport in conjugated polymers and provide structural design criteria for improving their performance.

Generally, Seebeck and electrical conductivity depend on the carrier concentration as $n = \int g(E)f(E)dE$ via Fermi level, and from this we can clearly see the reason behind their interdependency; increasing carrier concentration via doping fills more states and increases electrical conductivity but at the same time this brings E_F closer to the average E which negatively impacts Seebeck (see Eq. 4.9 and 4.10). Thus, there is a narrow range of doping that optimizes the thermoelectric power factor, which typically occurs when 10-20% of the states are occupied by a charge carrier. The DOS affects the trade-off between n, σ and α —a sharp DOS separates the E_F from the densely-spaced states, increasing the average energy per carrier (E–E_F) and with it the Seebeck, while a broad DOS implies that E_F moves further to fill the scattered states, flattening the α vs. σ curve, signifying the impact of the shape of the DOS on the α vs. σ curve.

In the Kang-Snyder model, they substitute for g(E)μ(E) and obtain a empirical fitting transport function,

$$\sigma(E,T) = \sigma_{E_0}(T)\left(\frac{E-E_t}{k_BT}\right)^s, \sigma = \int \sigma(E)dE \tag{5.3}$$

where σ_{E_0} is a temperature-dependent but energy-independent parameter called the transport coefficient which iscomparable to the mobility of the material. Using different values of σ_{E_0} and$s$ values, they fit this model with the α vs. σ curves from a variety of organic SCs, and deduce that different$s$ parameter stems from different types of charge transport. They observed that most polymers have a shallow α vs. σ curve (s=3 trend), whereas, PEDOT:Tos exhibits a sharper curvature (s=1 trend), which they conclude is unique to this Polymer. However, the factors that determine the transport parameter$s$ in the Synder-Kang model are still unclear.

5.1 Effect of dopant clustering on the density of states

As we saw in Ch. 4, using a Gaussian distribution to describe the DOS, where the width of the DOS accounts for the degree of energetic disorder in the structure, varying the energetic disorder simply shifts the α vs. σ on the log-log curve with minimal difference in its shape (Fig. 4.3) and cannot fully account for a significant difference in the slope.

Arkhipov et al. [11] found that the long-range Coulombic interaction between the ionized dopant molecules and the localized carriers further increases energetic disorder and broadens the deep tail of the DOS. The dopant-induced DOS distribution is given as

$$g(E) = \frac{4\pi q^6 N_d}{(4\pi\epsilon_0\epsilon_r)^3}\int_{-\infty}^{0}\frac{dE_c}{E_c^4}exp\left[\frac{4\pi N_d}{3}\frac{q^6}{(4\pi\epsilon_0\epsilon_r E_c)^3}\right]g_i(E-E_c), \tag{5.4}$$

where N_i and N_d are the intrinsic and dopant concentration respectively, E_c is the potential energy of the Coulomb interaction and g_i is the intrinsic Gaussian DOS given in Eq. 4.1 and depicted by the solid black line in Fig. 5.1(a). However, they do not consider the impact of dopants clustering. In the presence of dopant clustering, the probability density $w(r)$ of the minimum distance at which a dopant cluster is

present can be modeled by a Poisson distribution $w(r) = 4\pi r^2 N_s e^{\left(\frac{4\pi}{3} N_s r^3\right)}$, where N_s is the cluster density. The potential energy of the Coulomb interaction between the localized charge carrier and dopant cluster is now $E_c = -C_s e^2/4\pi\epsilon_0\epsilon_r r$, where C_s is the number of dopants in each cluster. Combining these equations to obtain the energy distribution of localized states over the intrinsic energy E_i and E_c we get

$$g(E) = \frac{4\pi q^6 N_s C_s^3}{(4\pi\epsilon_0\epsilon_r)^3} \int_{-\infty}^{0} \frac{dE_c}{E_c^4} exp\left[\frac{4\pi N_s C_s^3}{3} \frac{q^6}{(4\pi\epsilon_0\epsilon_r E_c)^3}\right] g_i(E - E_c), \tag{5.5}$$

where $N_s = N_d/C_s$. We use the rejection sampling technique to generate an energy distribution from the calculated DOS; and then randomly assign an energy to each site from the distribution. We simulate a 35×25×25 lattice of sites with an average distance between adjacent sites a=0.38 nm using the modified Gaussian DOS calculated as described above and the model described in Sec. 4.2. We use overlap factor γ=1 and Σ_{ij}=0.25, unless noted otherwise.

5.2 Results and discussion

5.2.1 Gaussian vs. heavy-tailed distribution

We calculate the DOS resulting from doping concentration N_d in clusters having size C_s, according to Eq. 5.5, and find that doping and clustering result in a heavy-tailed distribution with a Gaussian core and a wide quasi-exponential tail [11], as shown in Fig. 5.1(a). Firstly, to look at the effect of an exponential tail in the DOS on the TE properties, we compare the α vs. σ plot for a Gaussian and a purely exponential DOS (Fig. 5.1(b)), and find that the exponential DOS results in a much flatter curve. This can be understood from the Mott formula given in Eq. 4.14. When mobility is only weakly dependent on carrier concentration, the second term is small and an exponential DOS $g(E) \propto exp(-E/\Gamma_E)$ leads to a nearly constant Seebeck independent of doping or electrical conductivity but inversely proportional to the

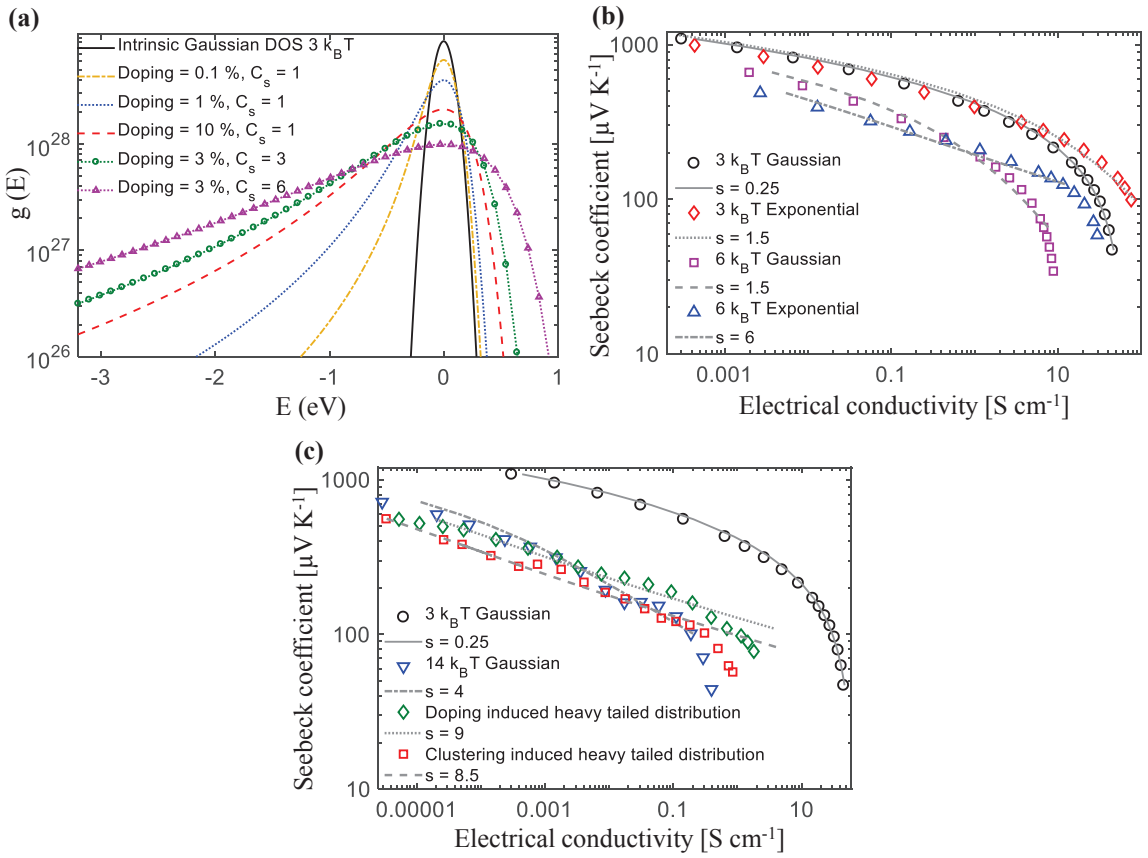

Figure 5.1. (a) The effect of doping and clustering on the DOS distribution with intrinsic Gaussian width of 3 k_BT. The charge carriers interact coulombically with the ionized dopants creating additional deep trap states, resulting in a heavy-tailed DOS. Log-log plot of α vs. σ showing the change in slope due to (b) Gaussian and exponential DOS, and (c) doping and clustering induced heavy-tailed DOS. The doping induced distribution is computed with N_d=10% and C_s=1, and the clustering induced distribution with N_d=3% and C_s=3. We have fit our simulated results (symbols) to Snyder and Kang's charge transport model (gray lines) and the corresponding transport parameter 's' values are shown. Taken from Ref. [22].

energetic disorder that dictates the width of the DOS. This 'change in shape' of the DOS results in a change in slope in the α vs. σ plot. In Fig. 5.1(c) we compare the effect of a purely Gaussian vs. a heavy-tailed DOS for different values of N_d and C_s. We compare our simulated results to Snyder and Kang's charge transport model [81] and find that a Gaussian distribution results in significantly lower trans-

port parameter$s \leq 1.5$ compared to the exponential case which has$s \geq 1.5$, and this difference increases further with increasing energetic disorder (Fig. 5.1(b)).

5.2.2 Hopping simulation and the transport parameter

In Fig. 5.2 we present a more detailed comparison to Kang and Snyder's charge transport model. Using Eq. 5.1, 5.3 and reduced Fermi level $\eta = (E_F - E_t)/k_BT^2$, a reduced Fermi level is initially found for each simulated α using a root finding algorithm. Next, σ_{E_0} is determined using a least squares regression fit to the charge transport model of simulated σ vs. calculated η. At high energetic disorder in the presence of a heavy-tail the curve cannot be fit by transport parameter values of s=1 or s=3, indicating the limitations of a band model in predicting transport in highly disordered systems. A narrow Gaussian DOS (<6k$_B$T) fits s=0.5 very closely (see Fig. 5.2(a)), however, with increasing energetic disorder (wide Gaussian) and with dopant clustering (heavy-tailed distribution), it is not possible to fit the entire curve with a single value of$s$ (Fig. 5.2(b) and (c)). Parts of the α vs. σ curve can be fit with different$s$ values and we find the best fit for the flat part of the curve (nearly constant Seebeck) to show the effect of the exponentially decaying tail of the DOS leading to high values of s.

5.2.3 Impact of dopant morphology on the Seebeck and conductivity trade-off curve

To further elucidate the relationship of the shape of the curve to the shape of the DOS, we compare schematically the Gaussian and the heavy-tailed DOS in Fig. 5.3. We show states filled up to the Fermi level using different colors, while Fig. 5.3(c) shows the Seebeck coefficients corresponding to those colors. For a given α vs. σ curve, as E$_F$ approaches the center of the DOS and states are filled the average energy per carrier (E – E$_F$) decreases, which in turn leads to a decrease in the Seebeck. Considering the first term in Eq. 4.14 which is typically dominant, a larger slope in the

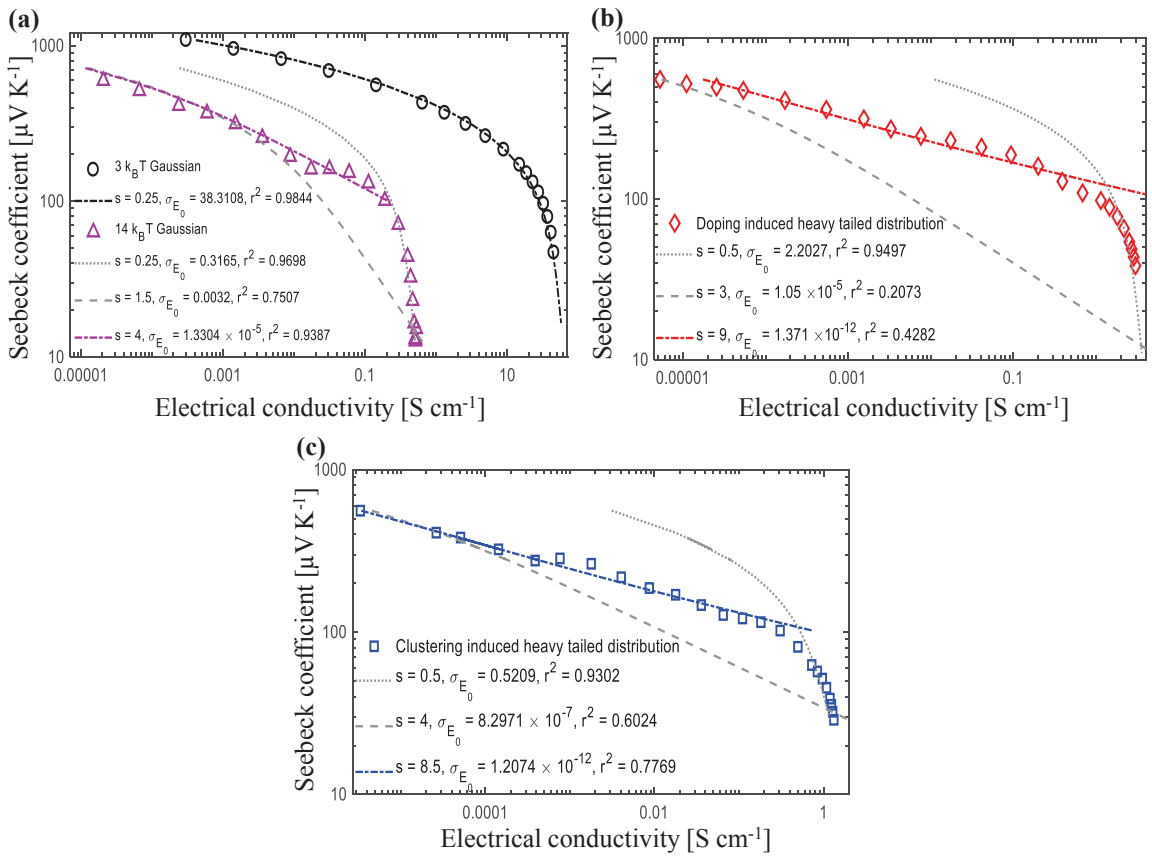

Figure 5.2. Log-log plot of α vs. σ computed for (a) Gaussian, (b) doping induced heavy-tailed and (c) clustering induced heavy-tailed DOS is fit with Snyder and Kang's charge transport model. The doping induced distribution is computed with N_d=10% and C_s=1, and the clustering induced distribution with N_d=3% and C_s=3. Taken from Ref. [22].

logarithm of the DOS g(E) implies a larger Seebeck coefficient; this can be observed in the pink region "1" in Figs. 5.3 (a) and (b). As the Fermi level approaches the middle of the DOS (region 4 in Fig. 5.3(c)), represented by E=0 in our calculations, the slope approaches zero as does the Seebeck coefficient. We find that this part of the curve is always fit by$s \leq 0.5$ as the center of the DOS is symmetric inside the Fermi window $(-\partial f/\partial E)$ irrespective of the presence of a heavy-tail. We compare or hopping model simulations to experimental data from PDPP4T and P3HT samples doped at 25 and 75 °C made by our collaborators in the Chemistry department. These samples

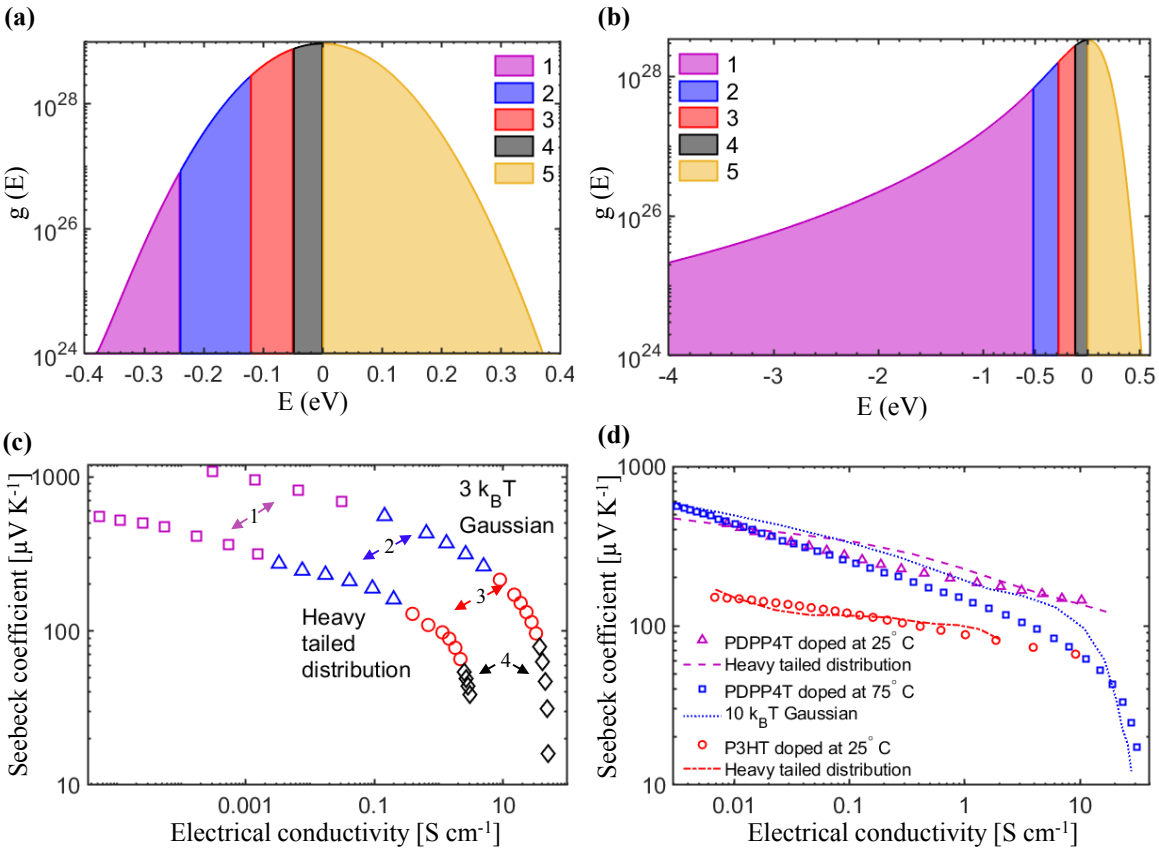

Figure 5.3. Schematic showing the filling up of the (a) Gaussian and (b) heavy-tailed DOS with increasing doping, by varying the Fermi level E_F further and closer to the center of the energy distribution and (c) the corresponding effect on the log-log plot of α vs. σ. (d) Comparison of our model to experimental data. (N_d=4% and C_s=1 for pink dashed line, N_d=0.9% and C_s=9 for red dot-dashed line, γ=0.01 and Σ_{ij}=0.0025 for all three cases). Taken from Ref. [22].

were doped with iodine, and the Seebeck coefficient and electrical conductivity were measured as the sample spontaneously de-doped. Surface potential contrast (SPC) mapping by Kelvin probe force microscopy (KPFM) was performed to gain insight into the distribution of dopants within the sample (see Ref. [22] for details of sample preparation and measurement). PDPP4T exhibited two very distinct shapes of the α vs. σ curve, depending only on the temperature at which doping was performed. KPFM measurements uncovered that room-temperature doping resulted in dopant inhomogeneity and clustering. PDPP4T doped at 75 °C had a very narrow distribu-

tion of SPC and PDPP4T doped at 25 °C had a comparatively wider distribution. Whereas, P3HT doped at 25 and 75 °C had an even wider distribution of SPCs with the appearance of a exponential tail in the SPC distribution of the P3HT sample doped at 25 °C. This is consistent with results from our simulation. As shown in Fig. 5.3(d) PDPP4T doped at 75 °C is most closely fit with α vs. σ computed from a purely Gaussian distribution with a width of 10 k_BT, whereas PDPP4T doped at 25 °C and P3HT is best fit with a dopant-induced heavy-tailed DOS that gives the required change in slope. Thus, it is the 'change in shape' of the DOS from spatial distribution and clustering of dopants that instigates the change in slope in the α vs. σ plot. Although the presence of a heavy tail leads to a constant α and a flatter α vs. σ curve advantageous for thermoelectrics, the Coulomb interaction causing the heavy tail also increases the energetic disorder, which has an adverse effect on α (see comparison of a 3 k_BT Gaussian and heavy-tailed DOS in Fig. 5.3(c)).

5.3 Conclusion

We find that dopant distribution affects the carrier DOS, with dopant clustering dramatically increasing the energetic disorder and causing a heavy-tail, which in turn affects the charge transport properties. A heavy-tailed DOS, depresses the Seebeck coefficient, resulting in a flattened α vs. σ curve and the Coulomb interaction causing the heavy tail also increases the energetic disorder, which has an adverse effect on α. Hence, a narrower DOS and a smaller transport parameter*s* is more advantageous for thermoelectric applications. This impact of an energetically disordered, heavy-tailed DOS on the thermoelectric properties is consistent with that recently reported by Kemerink and co-workers [1]. While Kemerink and co-workers assumed a homogenous distribution of the dopants and use this to capture the experimentally determined α vs. σ curve, we find that the spatial heterogeneity of dopants is necessary to describe the impact of doping on the shape of the DOS. The way the semiconductor has been

doped is fundamentally important to its thermoelectric performance across all carrier concentrations. Tuning the energetic disorder by controlling the dopant counterion distribution within the doped film of the organic semiconductor can lead to substantial improvements in the thermoelectric performance of organic semiconductors and controlling dopant clustering will be necessary to improve the existing and designing the next generation of organic electronic applications.

CHAPTER 6

MITIGATING DOPANT-INDUCED DISORDER IN CONJUGATED POLYMERS

The simple process of doping introduces complexities in the electronic structure because of the charge-charge Coulomb interactions between the dopant and the polymer. This long-range interaction is much more pronounced in polymers than in inorganic semiconductors because of their low dielectric permittivity (<3) [192]. Inadequate screening of the dopant-polymer interactions increases energetic disorder as it increases the width and alters the shape of the distribution of density of states (DOS). These factors suppress the density of free charge carriers by electrostatically binding the charge carriers to their conjugate dopant counterions, making doping less efficient. They also create deep traps, which adversely affect charge transport and thus the electronic and optoelectronic properties of the polymer. A flattened α-σ curve limits the maximum power factor and thus the thermoelectric conversion efficiency. Even in organic photovoltaics, energetic disorder limits efficiency [110] through open-circuit voltage loss [19].

We hypothesized that dopant-induced energetic order can be mitigated by screening the Coulomb interaction between the dopant and the polymer by raising the dielectric constant. Several experimental results support this approach. Leo and coworkers attributed the larger conductivity in n-doped fullerenes to a reduction in the activation energy of charge carriers from a large dielectric constant [158]. Takeya and coworkers reported that organic semiconductors 'in proximity to the ionic polymer dielectric can be electrostatically doped with a significantly high carrier density' [82]. In organic photovoltaics literature, studies show that increasing the dielectric

constant of the hole-transporting polymer or electron-transporting molecules by appending polar side chains [179] or by addition of salts [114] improves the efficiency of exciton splitting. Also, studies have noted the effect of dopant shape and size on Coulombic disorder and conductivity in ionic-doped polymers [106, 75]. Although some studies [174, 75] have noted the negligible impact of dopant ion size on transport, this was only at very high doping concentrations in paracrystalline polymers and not applicable in the moderate doing regime (<50%) of our interest, as the TE power-factor typically peaks around 10-20% doping. In this chapter, we explore the effect of both dopant size and dielectric permittivity in controlling the dopant-induced energetic disorder and TE properties of polymers.

6.1 Density of States model including dopant size and carrier-dopant electrostatic interactions

In the DOS equation in Eq. 5.5 for the contributions arising from energies satisfying $E_c >> \Gamma_E$, which correspond to instances where carriers are close to the ionized dopants, the integral can be further simplified. This condition is primarily satisfied by states in the heavy tail of the DOS, representing deep traps. The intrinsic DOS can then be approximated by a delta function $g_i(E - E_c) \approxeq N_i\delta(E - E_c)$ so that the whole integral can be evaluated analytically

$$\begin{aligned} g(E) &= 4\pi E_{Coulomb}^3 \int_{-\infty}^{0} \frac{dE_c}{E_c^4} exp\left[\frac{4\pi E_{Coulomb}^3}{3E_c^3}\right] N_i\delta(E - E_c) \\ &= 4\pi N_i \frac{E_{Coulomb}^3}{E^4}\left[\frac{4\pi E_{Coulomb}^3}{3E^3}\right] \end{aligned} \tag{6.1}$$

where the pre-factor groups together all the constants into

$$E_{Coulomb} = \frac{q^2 C_s}{4\pi\epsilon_0\epsilon_r} N_S^{1/3}, \tag{6.2}$$

which is the average coulombic energy of interaction between two dopants. This heavy tail of the DOS exhibits a combination of exponential and power-law dependence on energy, departing from the intrinsic Gaussian shape. The E^4 term in the denominator of the DOS gives the tail a polynomial shape when doping is low and the exponential term is close to 1.

However, the model in Eq. 5.5 produces a tail with very deep traps because it allows $E_C(r)$ to diverge to $-\infty$ as $r \to 0$, equivalent to treating dopants as point charges. Such infinitely deep traps have a dramatic impact on conductivity [11, 215] which is further enhanced with dopant clustering shown in Fig. 6.1. Since conductivity, is dictated by the expression $\sigma = nq\mu$, where n is the concentration of charge carriers, q is the carrier charge, and μ is the charge carrier mobility, conductivity is expected to scale linearly with the concentration of free carriers or carrier mobility. However, as seen in Fig. 6.1 at low dopant concentrations, the mobility and thus conductivity decreases as the dopant concentration increases. Then, as the dopant concentration increases further, the mobility first increases and plateaus at high dopant concentra-

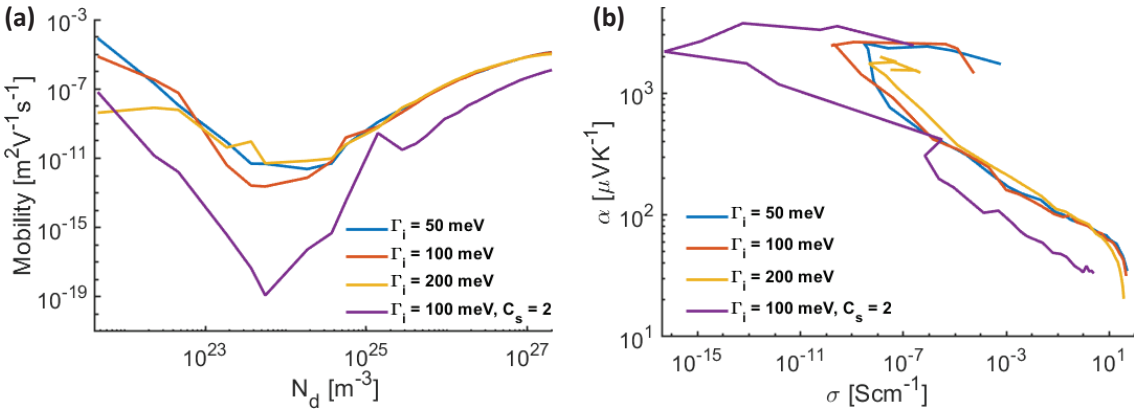

Figure 6.1. (a) Mobility vs. doping concentration —at low dopant concentrations, mobility decreases as the dopant concentration increases, then, as the dopant concentration increases further, the conductivity first increases and plateaus at high dopant concentration. (b) The corresponding effect of mobility on the conductivity which causes a loop in the α vs. σ curve.

tion which has also been noted in the literature [210, 64, 136]. This is because charge carriers get 'stuck' in the Coulomb trap states deep in the tail and do not contribute to transport [10]. Transport improves dramatically at higher doping concentrations as the tail states are filled.

The infinitely deep traps can be resolved by limiting the most negative value of $E_c(r)$, and thus the lower limit of the integral in Eq. 5.5, to the on-site energy of the dopant, typically -0.5 to -1 eV [11, 215]. Doing so is equivalent to limiting the distance to the nearest dopant to be no smaller than a dopant radius R_S obtained by setting $E_c(R_S)$ equal to the on-site energy, with the radius of 4-8 Å, corresponding to on-site energy of -0.5 to -1 eV. More generally, a finite-sized dopant can be modelled by a charge distribution instead of a point charge. For a Gaussian charge distribution, the potential energy becomes

$$E_c(r) = -\frac{C_s q^2}{4\pi\epsilon_0\epsilon_r r} erf\left(\frac{r}{R_s}\right). \tag{6.3}$$

Then the integral for the DOS must be performed with respect to nearest dopant distance r rather than energy because E_c (r) is no longer invertible, resulting in

$$g(E) = 4\pi N_s \int_0^\infty r^2 exp\left(\frac{4\pi}{3} N_s r^3\right) g_i\left[E - E_c(r)\right] dr \tag{6.4}$$

This approach is also useful in capturing the finite size of dopant clusters, which can be assigned a radius R_S instead of being treated as being point charges. Other formulations are possible, such as treating the ionized dopant's charge distribution as a shell of radius R_S, in which case the Coulomb potential inside $r < R_S$ becomes constant $E_c(r) = -\frac{C_s q^2}{4\pi\epsilon_0\epsilon_r R_s}$; coincidentally, this is also the maximum value reached by the potential from a Gaussian charge distribution. We implemented all of the above and found the Gaussian distribution to produce the smoothest DOS tail (Fig.

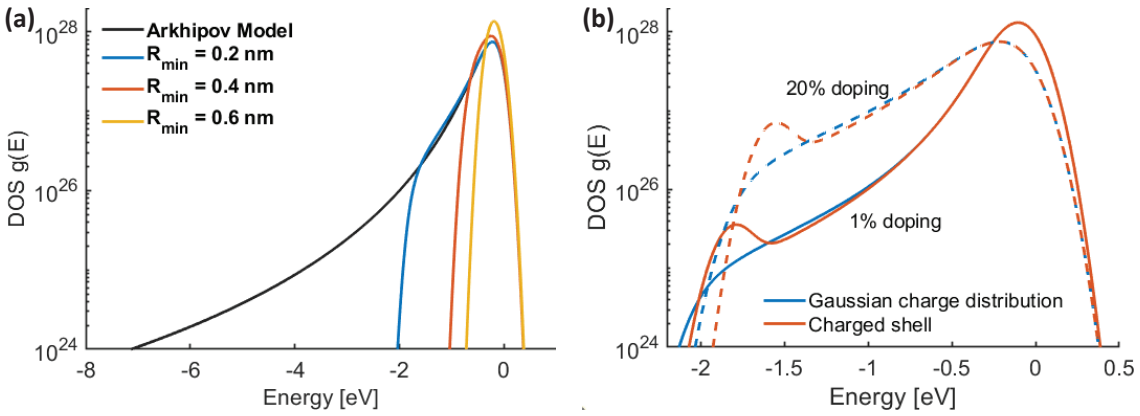

Figure 6.2. (a) Comparision of the DOS modeled using the Arkhipov model in which dopants are treated as point-charges vs. modeling it as a finite sized-dopant, which limits the Coulomb energy E_c and prevents the formation of very deep trap states. (b) Modeling a finite-sized dopant by a Gaussian vs. shell charge distribution. The Gaussian distribution produces the smoothest DOS tail.

6.2(b)), while the choice of dopant size/radius has far more impact on the DOS than how the dopant distribution is modeled (Fig. 6.2(a)).

We simulate a 35×35×50 lattice of sites with an average distance between adjacent sites a=0.6 nm using the modified DOS as described above (with Γ_i=100 meV and $\epsilon_r = 3.7$ unless noted otherwise) and the model described in Sec. 4.2 (with γ=0.75 and $\Sigma_{ij} = \gamma/4$). We no longer assign a fixed DOS and move the Fermi level to increase the carrier density, but calculate the DOS at each doping concentration and then use the bisection method to iteratively find the corresponding Fermi level for the given carrier density. The iteration typically converges to sufficient precision within 20 iterations. We also iterate the entire simulation at each dopant concentration 10 times, to reduce the sampling error from the randomly assigned site energies.

The impact of the dopant radius on the mobility and the α vs. σ curve is shown in Fig. 6.3. Increasing the dopant size limits the formation of deep traps and the 'nose-dive' in mobility at low dopant concentrations, which improves with increasing dopant size. We use r=2 Å which would correspond to on-site energy of -1.9 eV in

the rest of the simulations to keep the impact of dopant size to a minimum so as to independently study the impact of dielectric permittivity on transport.

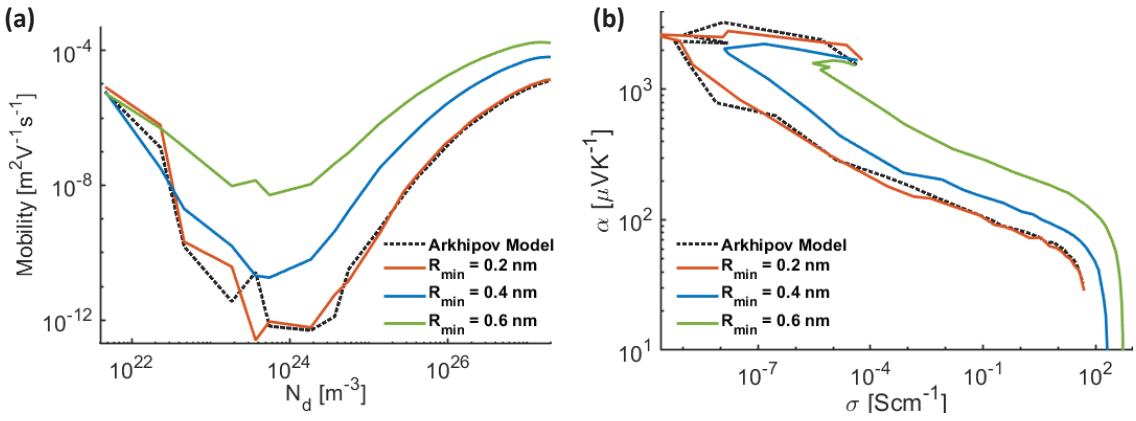

Figure 6.3. (a) Mobility vs. doping concentration —a finite-sized dopant limits the formation of deep traps and the plunge in mobility at low dopant concentrations, which improves with increasing dopant size. (b) The corresponding α vs. σ curve showing the limited conductivity looping with increasing dopant size.

6.2 Factors determining the Seebeck and conductivity trade-off curve

We show the calculated DOS for doping concentration N_d in clusters having size C_s. As seen earlier doping resulted in a heavy-tailed distribution with a Gaussian core and a wide quasi-exponential tail (Fig. 6.4(a)). Increasing dopant concentration lifted the long quasi-exponential tail at the expense of the central Gaussian DOS; clustering of dopants further amplified this effect, as seen from the similarity between the DOS curves with cluster size C_s=3 at 2% and C_s=1 at 20% doping. Increasing the effective dielectric permittivity dramatically reduced the Coulomb interactions and minimized the tail (Fig. 6.4(b)). A more general way to capture the impact of dopants is to extract the effective energetic disorder from each DOS curve. Energetic disorder is the standard deviation of the DOS g(E): $\Gamma_E^2 = \int Eg(E)dE / \int g(E)dE$,

which can be determined regardless of the shape of the DOS. The additional energetic disorder is caused by doping as it closely follows the Coulomb interaction energy with the nearest dopant (Fig. 6.4(c)). Here N_d=N_s as C_s=1 for all cases. Raising the dielectric permittivity lowered this additional dopant-induced energetic disorder even at high doping concentrations, nearly restoring the intrinsic Gaussian DOS.

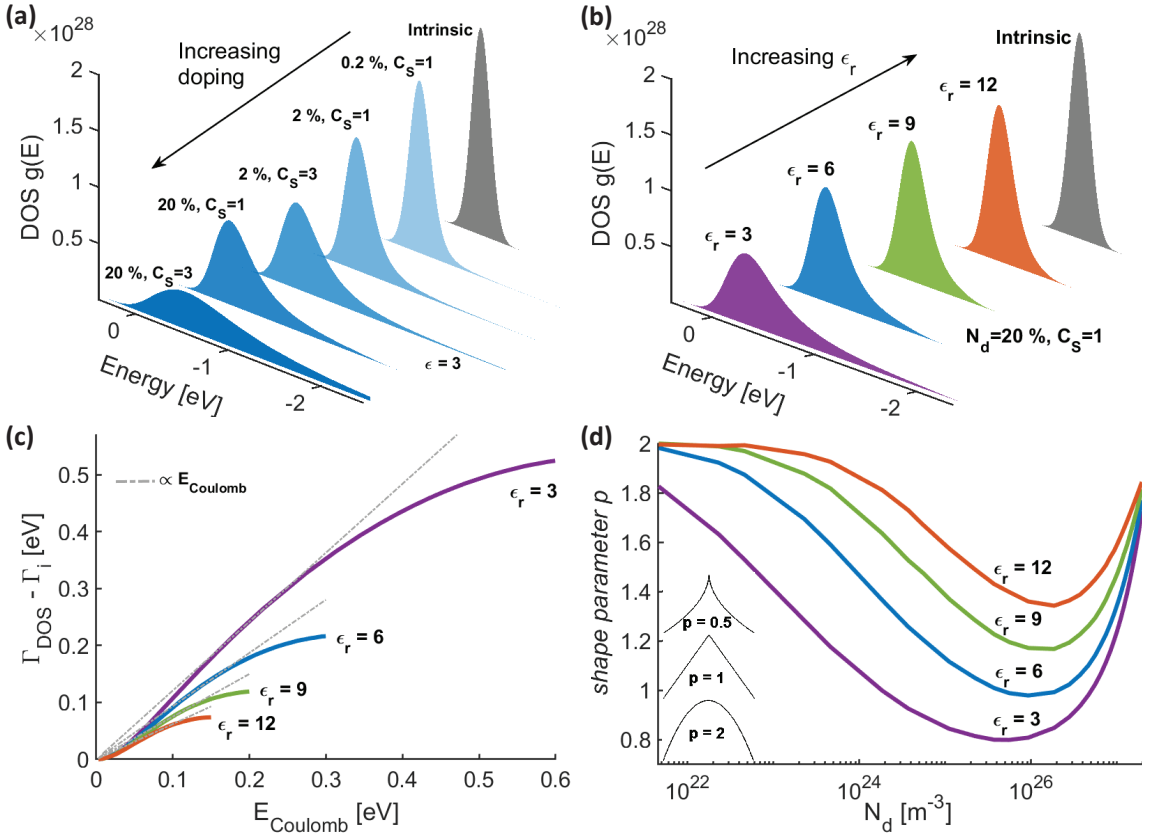

Figure 6.4. Increasing the dielectric permittivity counteracts the broadening of the DOS. (a) The effect of doping and clustering on the DOS distribution with intrinsic Gaussian width of 100 meV. (b) Increasing the dielectric constant counters the broadening of the DOS by mitigating the Coulomb carrier-dopant interactions (c) Additional energetic disorder caused by doping as a function of Coulomb energy for the standard (ϵ_r = 3) and elevated dielectric constants. The grey dashed lines are linear fits showing that the amount of energetic disorder closely follows the coulomb interaction energy. (d) Generalized Gaussian shape parameter p vs. doping concentration showing that increasing the dielectric constant keeps the shape parameter more Gaussian (p≈2) even at higher doping concentrations.

To capture the impact of doping and dielectric constant on the shape of the DOS, we liken it to a generalized Gaussian distribution (GGD), a parametric classification of symmetric distributions given by

$$G(E) = \frac{pA(p,\Gamma_E)}{2\Gamma_E\gamma(1/p)} exp\left[-\left(A(p)|E|/\Gamma_E\right)^p\right] \tag{6.5}$$

where $A(p) = \sqrt{\gamma(3/p)/\gamma(1/p)}$, γ denotes the gamma function, Γ_E is the standard deviation, and p is the shape parameter. A p value of 2 corresponds to a Gaussian distribution and smaller the p value is, the heavier the tail of the distribution, as illustrated in the inset of Fig. 6.4(d) and Fig. 6.5(a). For a given distribution, p can be estimated by finding the root of $M_{2p}/(M_p^2) - (1+p) = 0$ using a secant method, where M_r is the r-th absolute moment of the GGD [152]. We find that at low doping the shape parameter p is 2, indicating the DOS is more Gaussian and as we increase doping p decreases indicating that the tail gets heavier, with p reaching as low as 0.8 at very high doping values (6.4(d)). However, increasing the dielectric constant shifts the p values closer to 2 even at high doping concentrations, keeping the DOS more Gaussian.

Since doping affects both the width (Γ_E) and shape (p) of the DOS distribution, we studied their individual impact on the α vs. σ curve. We plot the α vs. σ curve with constant width Γ_E=Γ_i=100 meV and p values ranging from 0.8 to 2. We find that at constant width a lower p value has the effect of flattening the α vs. σ curve leading to a higher power factor (Fig. 6.5(b)). To study the impact of energetic disorder, first, we used a fixed Gaussian DOS (p=2 in Eq. 6.5, keeping its width Γ_E constant across doping concentrations, and obtained the α and σ at various carrier densities by moving E_F closer to the center. In this case, larger Γ_E shifted the α vs. σ curve down (lower α) and left (lower σ) (grey lines in Fig. 6.6(a)), with minimal changes to its slope. However, if we let the Γ_E increase with doping concentration by extracting it from the DOS (Eq. 6.4) but keep the shape Gaussian

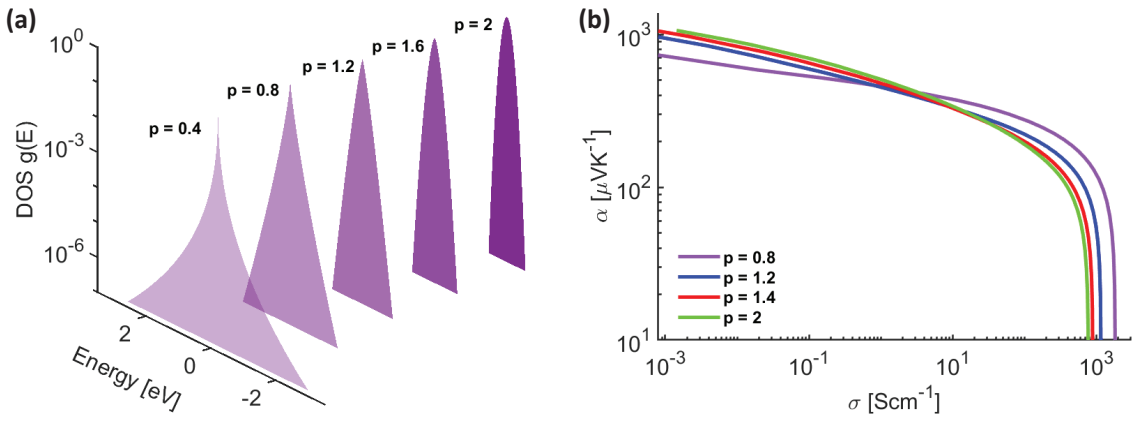

Figure 6.5. (a) Generalized Gaussian distribution with shape parameter p values ranging from 0.4 to 2, showing the increasing heavy tail as p decreases. (b) The effect of shape parameter p on the α vs. σ curve with constant width Γ_E=Γ_i=100 meV. At constant width a lower p value has the effect of flattening the α vs. σ curve leading to a higher power factor.

(p=2), the resulting α vs. σ exhibited a much higher slope ($\propto \sigma^{-1/2.5}$), indicating that the doping-induced Γ_E, while detrimental to transport in general, had a net effect of lowering α at higher doping concentrations. This can be understood from the Mott formula in Eq. 4.14. When $\mu(E)$ is only weakly varying, the second term is small, resulting in $\alpha \propto -(E_F/\Gamma_E)^{p-1}$. A broader Gaussian DOS results in a smaller Seebeck coefficient while a value of p closer to 1 produces a flatter α curve. The point E_F=0 where α vanishes coincides with 50% doping. Intrinsic disorder plays a complementary role and dictates an upper bound on the trade-off curve —larger Γ_i depresses the α even at low doping and flattens the curve, typically from $\alpha \propto \sigma^{-1/2.5}$ to $\sigma^{-1/4}$.

Taking the dopant-induced Γ_E while fixing the shape parameter to different values, however, produced a significant difference in theα vs. σ curve, whose slope decreased with p (black lines in Fig. 6.6(b)). The difference is largest at low-to-moderate doping when carriers are predominantly in the tail of the DOS. In the presence of the heavy tail, doping moved E_F closer to the center of the DOS while the transport energy

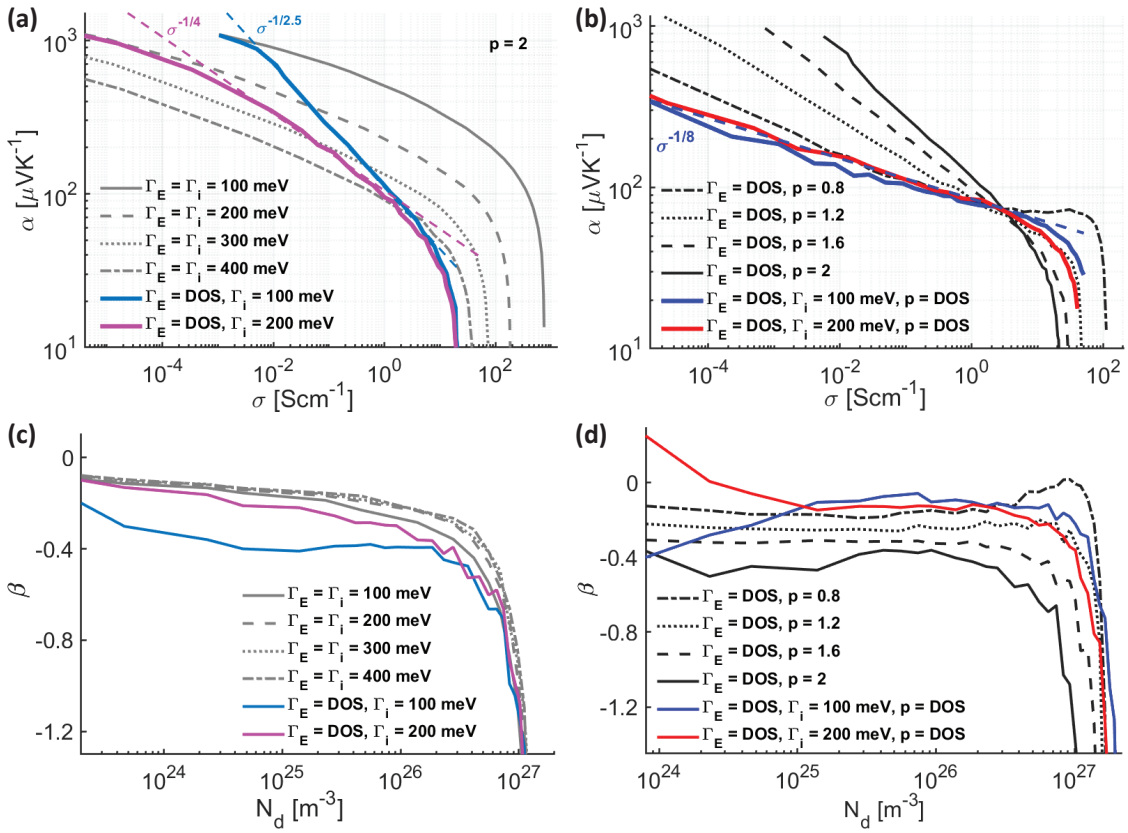

Figure 6.6. Effect of the width (Γ_E) and shape parameter p of the DOS on the trend of the α vs. σ curve. (a) The α vs. σ curves for GGD with fixed Γ_E (gray lines) and the α vs. σ curve with Γ_E increasing with doping (pink and cyan lines). p is fixed to 2 for all the cases. (b) The α vs. σ curves for a DOS with shape parameter fixed to 0.8, 1.2, 1.6 and 2, and Γ_E increasing with doping (black lines). The blue and red lines show the standard case with DOS computed from Eq. 6.4, where Γ_E and shape parameter p are both changing for Γ_i values of 100 and 200 meV, respectively.The exponent β of the power law scaling $\alpha = \sigma^{\beta}$ vs. doping concentration. (c) β values extracted from α vs. σ curves from (a). (d) β values of α vs. σ curves from (b).

$E_T = \langle E_i \rangle$ initially decreased as the trap-like states in the tail, which do not contribute significantly to transport, are filled first. This results in a lower $\alpha \propto E_F - E_T$, decreasing the Seebeck along with the conductivity. The α vs. σ curve with the DOS computed from Eq. 6.4, where both Γ_E and p are varying with doping (solid line in Fig. 6.6(b)), scales as $\alpha \propto \sigma^{-1/8}$. To precisely examine the slope across the entire range of doping concentration, we plot the running exponent $\beta = d(ln\ \alpha)/d(ln\ \sigma)$ vs.

doping concentration and find that the average exponent values in the flat part of the α vs. σ curve match well with the slope of the fit lines (Fig. 6.6(c) and (d)).

Previous works have developed empirical relationships between α and σ that scale as $\alpha \propto ln\ \sigma,\ \alpha \propto \sigma^{-1/4}$ [206, 62] and more generally $\alpha \propto \sigma^{-1/s}$ in the Kang-Snyder model [81],where s is the transport parameter, without establishing a connection to a specific material property as shown in Ch. 5. Here we have connected the transport parameter s to the shape of the DOS as it evolves in the presence of dopant-induced energetic disorder. We fit the α vs. σ curves of P3HT and PDPP4T from Ch. 5 where we showed that different slopes of theα vs. σ curve stems from a different shape of the DOS due to the morphological difference in the distribution of dopants in the polymer. Polymers that retain a more Gaussian DOS due to homogenous distribution of dopants (PDPP4T doped at 75 °C) exhibit $\alpha \propto \sigma^{-1/4}$ behavior whereas polymers with a heterogenous distribution of dopants that have a more heavy-tailed DOS exhibit $\alpha \propto \sigma^{-1/6\ -1/8}$ (Fig. 6.7(a)).

We obtained experimental data of iodine-doped P3HT and composite of P3HT with 2% w/w barium titanate ($BaTiO_3$) nanoparticles from our collaborators in the Chemistry department. The particles are ∼10 nm in size and have a narrow size distribution, as characterized with Transmission Electron Microscopy and X-ray Diffraction. Our collaborators also imaged the elemental composition of the films with Scanning Electron Microscopy with Energy Dispersive Spectroscopy (SEM-EDS) and found to have an adequate dispersion of the nanocrystal across the polymer film. They confirmed that with lower wt%, the $BaTiO_3$ nanocrystals did not interfere with the crystal packing or orientation of the crystalline domains of P3HT with wide-angle x-ray scattering and razing-incidence wide angle x-ray scattering studies. The measured dielectric permittivity of the polymer-nanocrystal composite films with electrochemical impedance spectroscopy, exhibited a significant increase in dielectric permitivitty when compared to pristine polymer.

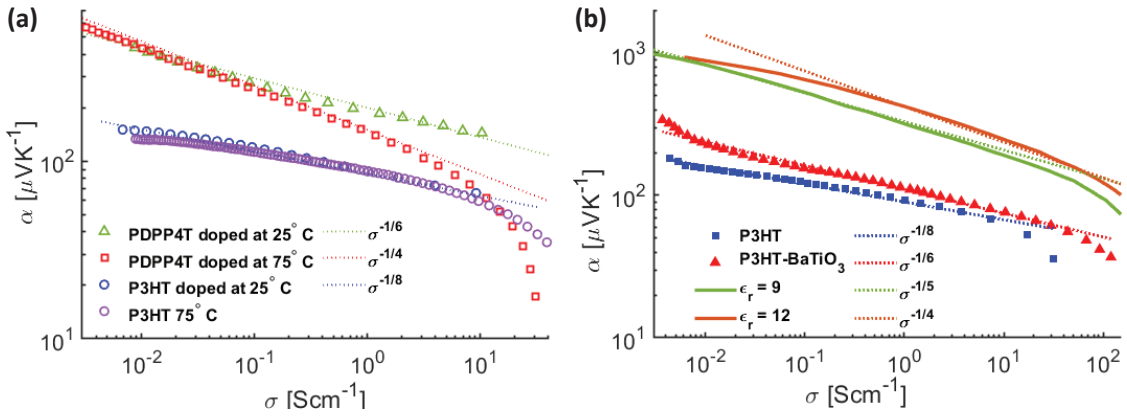

Figure 6.7. (a) α vs. σ curves of P3HT and PDPP4T from Ch. 5 showing that polymers that retain a more Gaussian DOS (homogenous distribution of dopants in PDPP4T doped at 75 °C exhibit $\sigma^{-1/4}$ behavior whereas polymers with a more heavy-tailed DOS (heterogenous distribution of dopants) have $\sigma^{-1/6 \sim -1/8}$. (b) P3HT samples closely fit $\sigma^{-1/8}$, whereas, P3HT/$BaTiO_3$ sample that has a higher ϵ_r is best fit with $\sigma^{-1/6}$. The simulated data for ϵ_r=9 and 12 is included to shown that the slope further increases to $\sigma^{-1/5 \sim -1/4}$ as the DOS becomes more Gaussian with increasing ϵ_r.

Fitting α vs. σ curves of P3HT and P3HT/$BaTiO_3$ samples that have different ϵ_r values (Fig. 6.7(b)), we find that P3HT samples closely fit $\sigma^{-1/8}$, whereas, P3HT/$BaTiO_3$ sample that has a higher ϵ_r and therefore a more Gaussian DOS is best fit with $\sigma^{-1/6}$. We further include the simulated data for ϵ_r=9 and 12 to show that the slope increases to $\sigma^{-1/5 \sim -1/4}$ as the DOS becomes more Gaussian in the absence of long-range Coulomb interactions with increasing ϵ_r. Hence, the shape of the α vs. σ curve is determined by the evolving size (Γ_E) and shape (p) of the DOS. We find that polymers that retain a more Gaussian DOS, stemming from a higher ϵ_r, larger on-site energy, or a more homogenous distribution of dopants, exhibit the $\alpha \propto \sigma^{-1/2.5 \sim -1/4}$ behavior, while polymers that encounter significant long-range Coulomb interactions have $\alpha \propto \sigma^{-1/6 \sim -1/8}$. It is interesting to note that, at comparable values of Γ_E, smaller p values have the effect of flattening the α vs. σ (Fig. 6.5(b)), indicating that the ideal DOS for TE applications would be a sharp nar-

row Gaussian with an exponential tail (small p and Γ_E). However, the presence of an exponential tail due to the dopants is always correlated with an increase in Γ_E, indicating that the path forward is by mitigating the dopant-induced disorder.

6.3 Maximizing power factor with dielectric screening

We fit the experimental data obtained from our collaborators with our simulations and found that the α vs. σ curve for pristine P3HT can be fit with ϵ_r=3.7 whereas $BaTiO_3$-P3HT composite with ϵ_r=5, shown in Fig. 6.8(a). This is consistent with our expectation that a higher dielectric permittivity will counteract the effect of dopant-induced Coulomb interactions on the polymer DOS, leading to better charge transport properties. The simultaneous increase in the Seebeck coefficient and conductivity results in a tremendous increase in the thermoelectric power factor (PF), as shown in Fig. 6.8(b). With ϵ_r=3.7, we observed a peak PF of 4.8 $\mu W m^{-1} K^{-1}$ in pristine

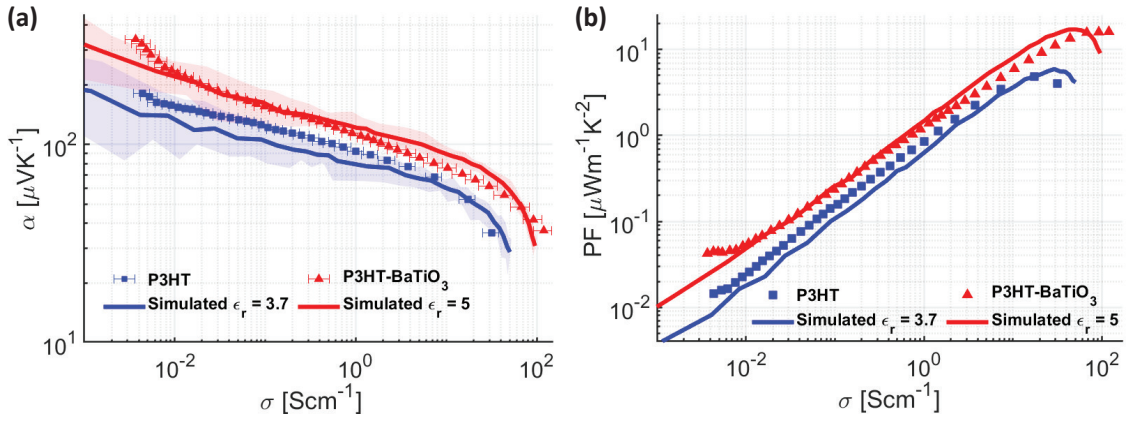

Figure 6.8. Higher dielectric permittivity leads to a higher power factor in OSCs. (a) Plot of simulated α vs. σ values and experimental values of $BaTiO_3$-P3HT composite and pristine P3HT. $BaTiO_3$-P3HT composite shows a fit to ϵ_r=5 while pristine P3HT fits ϵ_r=3.7. The simulations were iterated 25 times; the solid lines represent averaged values and the shaded region represents the minimum and maximum values. The horizontal error bars represent the error in the experimental electrical conductivity due to the variation in film thicknesses. (b) Power factor as a function of carrier density. There is a ∼4-fold increase in power factor from 4.8 to 16.2 as ϵ_r is increased.

P3HT, which increased to 16.2 $\mu W m^{-1} K^{-1}$ with the addition of $BaTiO_3$. Although the measured ϵ_r of P3HT is close to the value used in simulation, there is a discrepancy between the measured ϵ_r and the value needed to fit the curve for the $BaTiO_3$ composites. We posit that the value needed to fit the curve may be an effective dielectric permittivity experienced by the electric fields between charge carriers and dopant ions, which depends on their average distance from the nanocrystal.

We examine conductivity and Seebeck vs. doping in Fig. 6.9(a). Increasing ϵ_r mitigates dopant-induced disorder and produces a more sharply peaked DOS, boosting Seebeck at high doping due to the increased separation between the transport energy and the Fermi level (Fig. 6.9(b)). To elucidate the trend of the conductivity vs. N_d curve and its relation to ϵ_r and energetic disorder Γ_E we plot the running exponent $\zeta = d(ln\ \sigma)/d(ln\ N_d)$ vs. Γ_E for ϵ_r ranging from 3 to 12. At lower ϵ_r there is more long-range Coulomb interactions creating deeper traps or heavy tail in the DOS with increasing doping resulting in the higher range of Γ_E in Fig. 6.9(c). Charge carriers get 'stuck' in these trap-like states deep in the tail and do not contribute to transport. Transport improves at higher doping concentrations when the tail states are filled, discerned by the steeper conductivity curves in Fig. 6.9(a). Hence the slope increases with decreasing ϵ_r due to an increase in Γ_E. Conductivity increases super-linearly with doping [177], following a power-law [24] trend $\sigma \propto N_d^{\zeta}$, with the average exponent related to disorder $\zeta \propto \Gamma_E$ (Fig. 6.9(c)).

A narrower DOS reduces the difference Δ_{ij} between energies of neighbouring sites, which increases the probability of favorable hopping pathways by alleviating the required thermal assistance by absorption of phonons, resulting in much higher conductivity for the higher ϵ_r case. While both Seebeck and conductivity depend on the complex interplay between doping and energetic disorder, the peaks in the PF exhibit an inverse trend with energetic disorder, shown in Fig. 6.9(d). Increasing the ϵ_r from 3 to 12 mitigates dopant-induced energetic disorder, pushing the curves to lower Γ_E

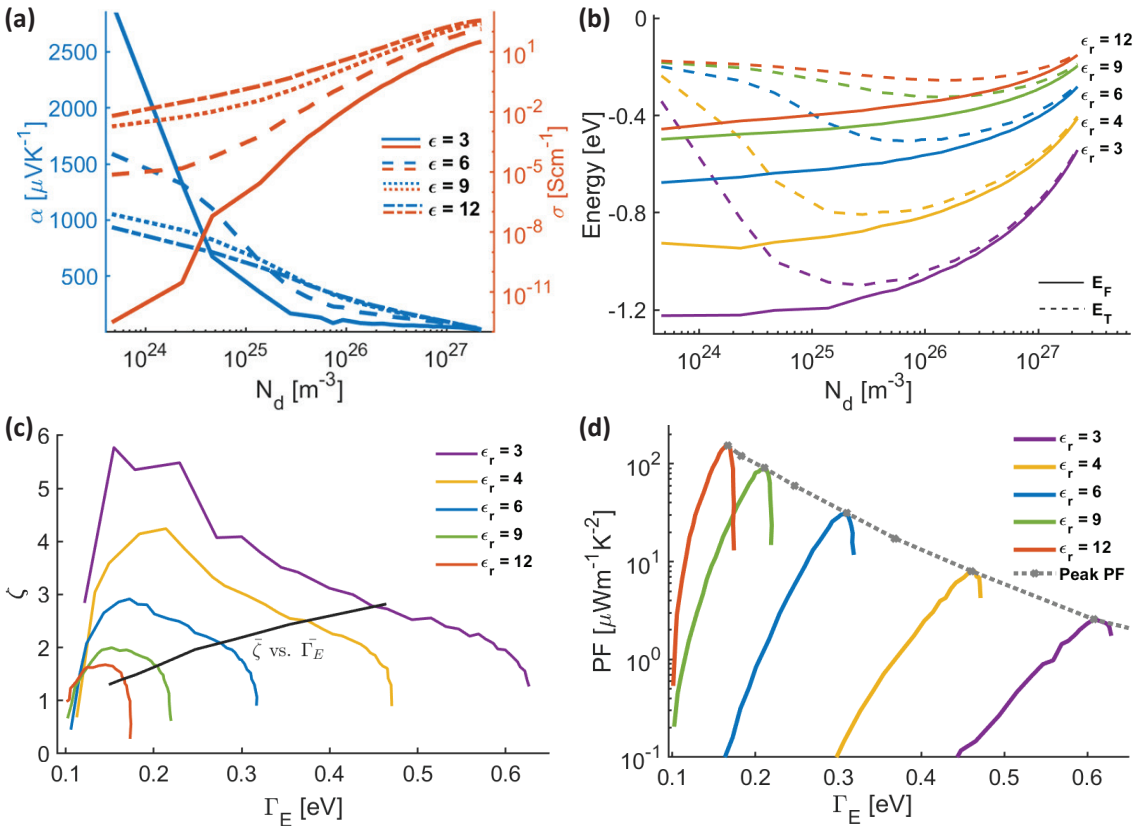

Figure 6.9. Power factor enhancement and the role of energetic disorder. (a) α and σ as a function of carrier density showing the respective increase with increasing ϵ_r at medium to high doping concentrations. (b) Fermi level E_F and transport energy E_T as a function of doping concentration showing the increase in separation between the transport energy and the Fermi level at higher doping concentration at higher ϵ_r values. (c) The exponent ζ of the power law scaling $\sigma \propto N_d^{\zeta}$ vs. width of the DOS (Γ_E). The average exponent ($\bar{\zeta}$) is proportional to the average energetic disorder $\bar{\Gamma_E}$. (d) Power factor vs. energetic disorder showing that increasing the dielectric constant reduces the energetic disorder at all doping concentrations and leads to higher power factor.

while increasing the height of the peak in the PF. Doping is more effective at higher ϵ_r as carriers contribute more readily to transport in the absence of the deep Coulombic tail. Consequently, we achieve higher power factors at lower doping concentrations (Fig. 6.10). While there is a modest increase in Seebeck with higher ϵ_r at a fixed

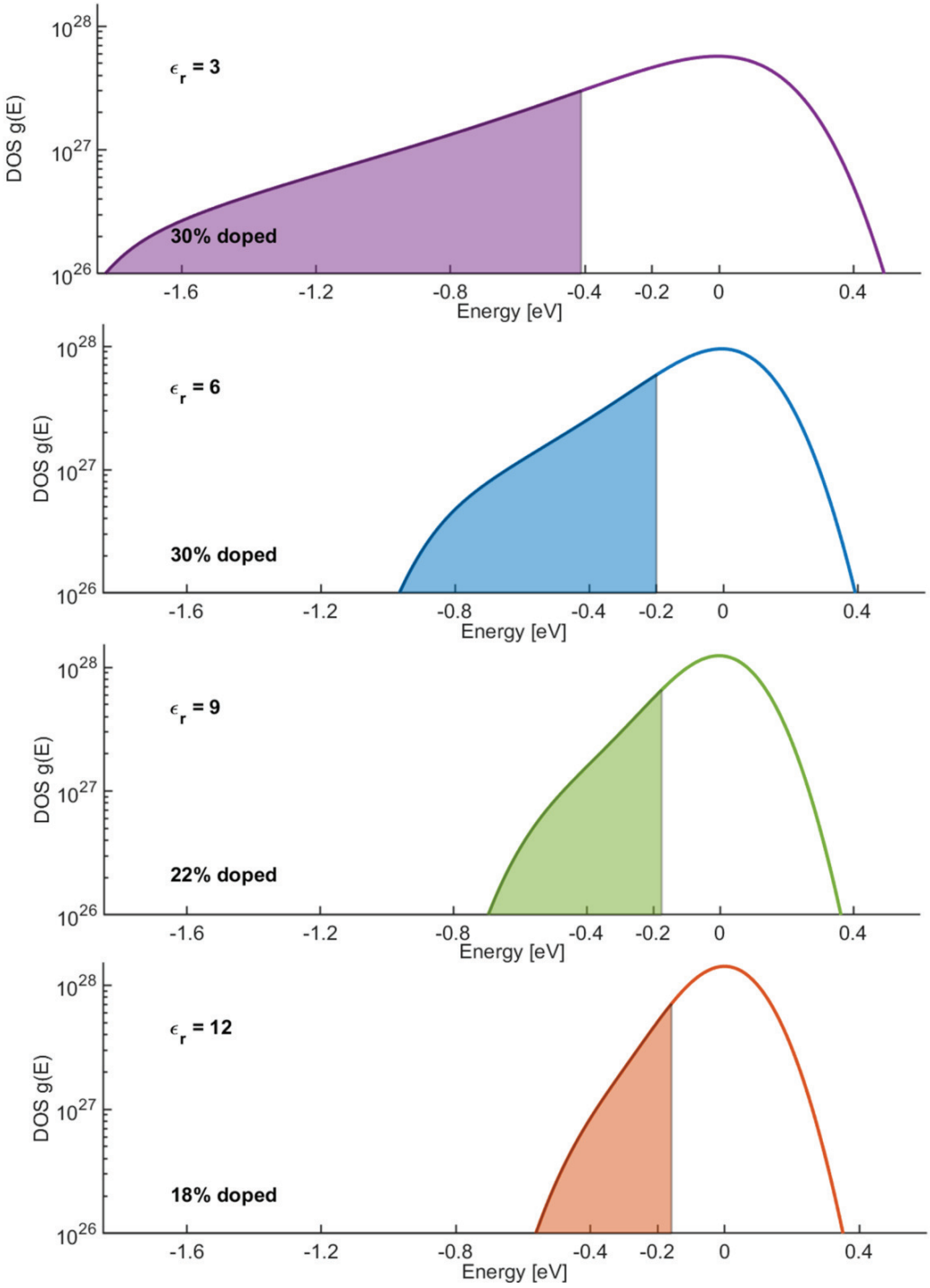

Figure 6.10. DOS with states filled up to the fermi level E_F corresponding to the doping at which the power factor is maximized at ϵ_r of 3, 6, 9 and 12. At higher ϵ_r values the peak power factor is achieved at lower doping values.

doping concentration, reaching the peak PF requires less doping, which effectively raises the Seebeck at the peak (Fig. 6.11(a)). However, the maximum attainable PF saturates for $\epsilon_r > 12$. Beyond this value, the polymer's intrinsic energetic disorder acts a limiting factor in the highest attainable PF. Dielectric screening can only

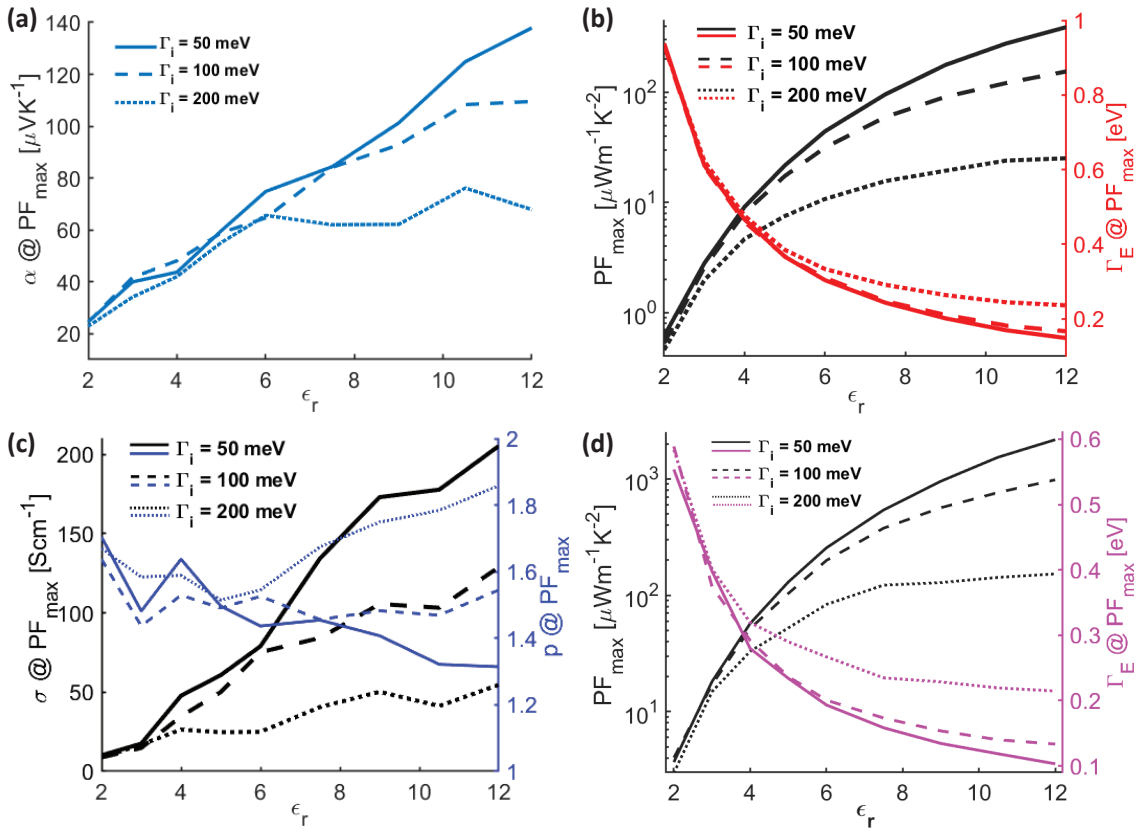

Figure 6.11. (a) Seebeck coefficient corresponding to the maximum power factor vs. ϵ_r for three different intrinsic disorder width Γ_i. We get an increase in Seebeck due to both the reduction in energetic disorder and the peak power factor achieved at lower doping concentration with increasing ϵ_r. (b) Maximum power factor and the energetic disorder vs. ϵ_r, showing that gains in the power factor saturate beyond $\epsilon_r > 12$, when they are limited by intrinsic disorder. (c) Conductivity σ and shape parameter p as a function of ϵ_r, plotted at the doping concentration corresponding to maximum power factor, showing increasing conductivity with decreasing intrinsic disorder, particularly when low intrinsic disorder and small p value produce a narrow main DOS with a heavy tail. (d) Maximum power factor and the energetic disorder vs. ϵ_r, showing the gain in power factor by changing the material parameters in the simulation (average distance between adjacent sites a=0.5 nm, overlap factor γ=0.5 and dopant radius r=3 Å) to values within the expected range in polymers.

mitigate the broadening of the DOS by carrier-dopant Coulomb interactions but not the intrinsic disorder within the polymer, which is related to structural disorder and depends on the polymer's morphology [4]. In Fig. 6.11(b), we plot the peak PF (left) and the energetic disorder (right), both as functions of the dielectric permittivity, for several values of intrinsic disorder Γ_i (50, 100, and 200 meV), echoing the inverse relationship between peak PF and Γ_E. The p value plays a complimentary role (Fig. 6.11(c)) as smaller intrinsic disorder makes the DOS tail more pronounced, leading to smaller p. There is a synergy between screening and morphology—when dopant-induced disorder is minimized by dielectric screening, conductivity, shown by black lines in Fig. 6.11(c), becomes inversely proportional to the remaining intrinsic disorder. At lower intrinsic disorder, the PFmax reached 391 $\mu\mathrm{Wm}^{-1}\mathrm{K}^{-1}$, which corresponds to a TE figure-of-merit of 0.6 at room temperature, assuming a typical thermal conductivity $\kappa \cong 0.2$ $\mathrm{Wm}^{-1}\mathrm{K}^{-1}$ [47]. However, this was calculated with the same parameters we used to fit the P3HT measured data. Changing parameters in the simulation to values within the range encountered in polymers, additional improvements with dielectric screening were observed (Fig. 6.11(d)), with the PF reaching 2170 $\mu\mathrm{Wm}^{-1}\mathrm{K}^{-1}$ at ϵ_r=12, which would correspond to a room temperature ZT of 3.2.

6.4 Conclusion

We find that the shape of the α vs. σ curve is determined by the evolving size and shape of the DOS and a sharp narrow Gaussian with an exponential tail would be the ideal DOS for TE applications. However, the presence of an exponential tail due to the dopants is always correlated with an increase in the energetic disorder and mitigating the dopant-induced disorder is key for development of organic TEs. We conclude that increasing both the dopant size and dielectric screening can mitigate dopant-induced traps and have a positive impact on the transport properties of doped

polymers with an intrinsically low dielectric constant. Doping is also more effective at higher dielectric values as carriers contribute more readily to transport and reaching the peak PF requires less doping. This study opens avenues towards developing more effective strategies to use dielectric screening for mitigating the effect of dopants in the DOS. Our results indicate that polymers with high dielectric permittivity and large dopant ions are a fertile new avenue of research in organic TEs and a path forward to obtain ZT values well over the highest reported 0.4 so far [87]. Beyond improving TE performance, we note that most of the improvement we observed in the PF comes from increases in the conductivity, particularly at low to medium doping concentrations, which is broadly useful in organic electronics. Long-range Coulomb interactions also impact other systems such as photogenerated carriers in organic photovoltaics. Raising the dielectric permittivity of the active layer could increase exciton dissociation, enhancing photovoltaic performance and improving carrier mobility in field effect transistors as well.

BIBLIOGRAPHY

[1] Abdalla, Hassan, Zuo, Guangzheng, and Kemerink, Martijn. Range and energetics of charge hopping in organic semiconductors. *Phys. Rev. B 96* (2017), 241202.

[2] Abeles, B. Lattice thermal conductivity of disordered semiconductor alloys at high temperatures. *Phys. Rev. 131* (1963), 1906–1911.

[3] Abeles, B., Beers, D. S., Cody, G. D., and Dismukes, J. P. Thermal conductivity of Ge-Si alloys at high temperatures. *Phys. Rev. 125*, 1 (1962), 44–46.

[4] Abutaha, Anas, Kumar, Pawan, Yildirim, Erol, Shi, Wen, Yang, Shuo-Wang, Wu, Gang, and Hippalgaonkar, Kedar. Correlating charge and thermoelectric transport to paracrystallinity in conducting polymers. *Nat. Commun. 11* (2020), 1737.

[5] Aksamija, Z. Lattice thermal transport in Si-based nanocomposites for thermoelectric applications. *J. Electron. Mater. 44* (2014), 1644.

[6] Aksamija, Z., and Knezevic, I. Anisotropy and boundary scattering in the lattice thermal conductivity of silicon nanomembranes. *Phys. Rev. B 82* (2010), 045319.

[7] Aksamija, Z., and Knezevic, I. Thermoelectric properties of silicon nanostructures. *J. Comput. Electron. 9* (2010), 173.

[8] Aksamija, Z., and Knezevic, I. Thermal conductivity of $Si_{1-x}Ge_x/Si_{1-y}Ge_y$ superlattices: Competition between interfacial and internal scattering. *Phys. Rev. B 88* (2013), 155318.

[9] Aksamija, Z., and Knezevic, I. Lattice thermal transport in large-scale polycrystalline graphene. *Phys. Rev. B 90* (2014), 035419.

[10] Arkhipov, V. I., Emelianova, E. V., Heremans, P., and Bässler, H. Analytic model of carrier mobility in doped disordered organic semiconductors. *Phys. Rev. B 72* (Dec 2005), 235202.

[11] Arkhipov, V. I., Heremans, P., Emelianova, E. V., and Bässler, H. Effect of doping on the density-of-states distribution and carrier hopping in disordered organic semiconductors. *Phys. Rev. B 71* (2005), 045214.

[12] Bae, Myung-Ho, Li, Zuanyi, Aksamija, Zlatan, Martin, Pierre N, Xiong, Feng, Ong, Zhun-Yong, Knezevic, Irena, and Pop, Eric. Ballistic to diffusive crossover of heat flow in graphene ribbons. *Nat. Commun. 4* (2013), 1734.

[13] Bao, Y., Liu, W. L., Shamsa, M., Alim, K., Balandin, A. A., and Liu, J. L. Electrical and thermal conductivity of Ge/Si quantum dot superlattices. *J. Electrochem. Soc. 152*, 6 (2005), G432.

[14] Barthelemy, Pierre, Bertolotti, Jacopo, and Wiersma, Diederik S. A lévy flight for light. *Nature 453* (2008), 495–498b.

[15] Bartkowiak, M., and Mahan, G. D. Nonlinear currents in voronoi networks. *Phys. Rev. B 51*, 16 (1995), 10825–10832.

[16] Bässler, H. Charge transport in disordered organic photoconductors a Monte Carlo simulation study. *phys. stat. sol. (b) 175*, 1 (1993), 15–56.

[17] Bera, Chandan, Soulier, M., Navone, C., Roux, Guilhem, Simon, J., Volz, S., and Mingo, Natalio. Thermoelectric properties of nanostructured $Si_{1-x}Ge_x$ and potential for further improvement. *J. Appl. Phys. 108*, 12 (2010), 124306.

[18] Berman, R. The thermal conductivity of some polycrystalline solids at low temperatures. *Proc. Phys. Soc. A 65*, 12 (dec 1952), 1029–1040.

[19] Blakesley, James C., and Neher, Dieter. Relationship between energetic disorder and open-circuit voltage in bulk heterojunction organic solar cells. *Phys. Rev. B 84* (2011), 075210.

[20] Blumen, A., Zumofen, G., and Klafter, J. Transport aspects in anomalous diffusion: Lévy walks. *Phys. Rev. A 40* (1989), 3964–3973.

[21] Borsenberger, P. M., Pautmeier, L., and Bässler, H. Charge transport in disordered molecular solids. *J. Chem. Phys. 94*, 8 (1991), 5447–5454.

[22] Boyle, Connor, Upadhyaya, Meenakshi, Wang, Peijian, Renna, Lawrence A., Korugic-Karasz, Ljiljana, Barnes, Michael D., Aksamija, Zlatan, and Venkataraman, Dhandapani. Tuning charge transport dynamics via clustering of doping in organic semiconductor thin films. *Nat. Commun. 10* (2019), 2827.

[23] Braginsky, L., Lukzen, N., Shklover, V., and Hofmann, H. High-temperature phonon thermal conductivity of nanostructures. *Phys. Rev. B 66*, 13 (2002), 134203.

[24] Brondijk, J. J., Roelofs, W. S. C., Mathijssen, S. G. J., Shehu, A., Cramer, T., Biscarini, F., Blom, P. W. M., and de Leeuw, D. M. Two-dimensional charge transport in disordered organic semiconductors. *Phys. Rev. Lett. 109* (2012), 056601.

[25] Bubnova, Olga, Khan, Zia Ullah, Malti, Abdellah, Braun, Slawomir, Fahlman, Mats, Berggren, Magnus, and Crispin, Xavier. Optimization of the thermoelectric figure of merit in the conducting polymer poly(3,4-ethylenedioxythiophene). *Nature Mater. 10*, 6 (2011), 429–433.

[26] Buran, C., Pala, M. G., Bescond, M., Dubois, M., and Mouis, M. Three-dimensional real-space simulation of surface roughness in silicon nanowire FETs. *IEEE Trans. Electron Devices 56*, 10 (2009), 2186–2192.

[27] Cahill, D. G., Ford, W. K., Goodson, K. E., Mahan, G. D., Majumdar, A., Maris, H. J., Merlin, R., and Phillipot, S. R. Nanoscale thermal transport. *J. Appl. Phys. 93* (2003), 793–818.

[28] Cahill, David G., Braun, Paul V., Chen, Gang, Clarke, David R., Fan, Shanhui, Goodson, Kenneth E., Keblinski, Pawel, King, William P., Mahan, Gerald D., Majumdar, Arun, Maris, Humphrey J., Phillpot, Simon R., Pop, Eric, and Shi, Li. Nanoscale thermal transport. ii. 2003-2012. *Apr. 1*, 1 (2014), 011305.

[29] Cahill, David G., Watson, S. K., and Pohl, R. O. Lower limit to the thermal conductivity of disordered crystals. *Phys. Rev. B 46*, 10 (1992), 6131–6140.

[30] Carruthers, Peter. Theory of thermal conductivity of solids at low temperatures. *Rev. Mod. Phys. 33*, 1 (1961), 92.

[31] Cheaito, Ramez, Duda, John C., Beechem, Thomas E., Hattar, Khalid, Ihlefeld, Jon F., Medlin, Douglas L., Rodriguez, Mark A., Campion, Michael J., Piekos, Edward S., and Hopkins, Patrick E. Experimental investigation of size effects on the thermal conductivity of silicon-germanium alloy thin films. *Phys. Rev. Lett. 109* (2012), 195901.

[32] Chen, G. Thermal conductivity and ballistic-phonon transport in the cross-plane direction of superlattices. *Phys. Rev. B 57*, 23 (1998), 14958–14973.

[33] Chen, Jie, Zhang, Gang, and Li, Baowen. Tunable thermal conductivity of $Si_{1-x}Ge_x$ nanowires. *Appl. Phys. Lett. 95*, 7 (2009), 073117.

[34] Chen, Yunfei, Li, Deyu, Lukes, Jennifer R., and Majumdar, Arun. Monte Carlo simulation of silicon nanowire thermal conductivity. *J. Heat Transf. 127*, 10 (2005), 1129–1137.

[35] Chiang, C. K., Fincher, C. R., Park, Y. W., Heeger, A. J., Shirakawa, H., Louis, E. J., Gau, S. C., and MacDiarmid, Alan G. Electrical conductivity in doped polyacetylene. *Phys. Rev. Lett. 39* (Oct 1977), 1098–1101.

[36] Chowdhury, Ihtesham, Prasher, Ravi, Lofgreen, Kelly, Chrysler, Gregory, Narasimhan, Sridhar, Mahajan, Ravi, Koester, David, Alley, Randall, and Venkatasubramanian, Rama. On-chip cooling by superlattice-based thin-film thermoelectrics. *Nature Nano. 4* (2009), 235–238.

[37] Cipriani, P., Denisov, S., and Politi, A. From anomalous energy diffusion to levy walks and heat conductivity in one-dimensional systems. *Phys. Rev. Lett. 94* (2005), 244301.

[38] Colombo, L., and Giannozzi, P. A first-principles derived prametrization of the adiabatic bond charge model. *Solid State Commun. 96* (1995), 49.

[39] Culebras, M., Gomez, C. M., and Cantarero, A. Enhanced thermoelectric performance of pedot with different counter-ions optimized by chemical reduction. *J. Mater. Chem. A 2* (2014), 10109–10115.

[40] Culebras, M., Gómez, C. M., and Cantarero, A. Review on polymers for thermoelectric application. *Materials 7* (2014), 6701–6732.

[41] Denisov, S., Klafter, J., and Urbakh, M. Dynamical heat channels. *Phys. Rev. Lett. 91* (2003), 194301.

[42] Dhar, Abhishek. Heat transport in low-dimensional systems. *Adv. Phys. 57*, 5 (2008), 457–537.

[43] Dhar, Abhishek, Saito, Keiji, and Derrida, Bernard. Exact solution of a lévy walk model for anomalous heat transport. *Phys. Rev. E 87* (2013), 010103.

[44] Dismukes, J. P., Ekstrom, L., Steigmeier, E. F., Kudman, I., and Beers, D. S. Thermal and electrical properties of heavily doped Ge-Si alloys up to 1300 °K. *J. Appl. Phys. 35*, 10 (1964), 2899–2907.

[45] Dresselhaus, M. S., Chen, G., Tang, M. Y., Yang, R. G., Lee, H., Wang, D. Z., Ren, Z. F., Fleurial, J.-P., and Gogna, P. New directions for low-dimensional thermoelectric materials. *Adv. Mater. 19* (2007), 1043–1053.

[46] Dubey, Nidhi, and Leclerc, Mario. Conducting polymers: Efficient thermoelectric materials. *J. Polym. Sci., Part B: Polym. Phys. 49*, 7 (2011), 467–475.

[47] Duda, John C., Hopkins, Patrick E., Shen, Yang, and Gupta, Mool C. Thermal transport in organic semiconducting polymers. *Appl. Phys. Lett. 102*, 25 (2013), 251912.

[48] Esfarjani, Keivan, Chen, Gang, and Stokes, Harold T. Heat transport in silicon from first-principles calculations. *Phys. Rev. B 84* (2011), 085204.

[49] Fan, Zhigang, Wu, Yugong, Zhao, Xuanhe, and Lu, Yuzhu. Simulation of polycrystalline structure with voronoi diagram in laguerre geometry based on random closed packing of spheres. *Comp. Mat. Sci. 29*, 3 (2004), 301 – 308.

[50] Ferenc, Járai-Szabó, and Néda, Zoltán. On the size distribution of Poisson Voronoi cells. *Physica A 385*, 2 (2007), 518 – 526.

[51] Feser, Joseph P., Chan, Emory M., Majumdar, Arun, Segalman, Rachel A., and Urban, Jeffrey J. Ultralow thermal conductivity in polycrystalline cdse thin films with controlled grain size. *Nano Lett. 13*, 5 (2013), 2122–2127.

[52] Fishchuk, I. I., Arkhipov, V. I., Kadashchuk, A., Heremans, P., and Bässler, H. Analytic model of hopping mobility at large charge carrier concentrations in disordered organic semiconductors: Polarons versus bare charge carriers. *Phys. Rev. B 76* (Jul 2007), 045210.

[53] Fornari, Rocco P., Aragó, Juan, and Troisi, Alessandro. A very general rate expression for charge hopping in semiconducting polymers. *J. Chem. Phys. 142*, 18 (2015), 184105.

[54] Franz, R., and Wiedemann, G. Ueber die wërme-leitungsfähigkeit der metalle. *Ann. Phys. 165*, 8 (1853), 497–531.

[55] Fritzsche, H. A general expression for the thermoelectric power. *Solid State Commun. 9*, 21 (1971), 1813 – 1815.

[56] Garg, Jivtesh, Bonini, Nicola, Kozinsky, Boris, and Marzari, Nicola. Role of disorder and anharmonicity in the thermal conductivity of silicon-germanium alloys: A first-principles study. *Phys. Rev. Lett. 106* (Jan 2011), 045901.

[57] Gartstein, Yu.N., and Conwell, E.M. High-field hopping mobility in molecular systems with spatially correlated energetic disorder. *Chem. Phys. Lett. 245*, 4 (1995), 351 – 358.

[58] Gilat, G. Analysis of methods for calculating spectral properties in solids. *J. of Comp. Phys. 10*, 3 (1972), 432–465.

[59] Gilat, G., and Kam, Z. High-resolution method for calculating spectra of solids. *Phys. Rev. Lett. 22*, 14 (1969), 715–717.

[60] Gilat, G., and Raubenheimer, L. J. Accurate numerical method for calculating frequency-distribution functions in solids. *Phys. Rev. 144*, 2 (1966), 390–395.

[61] Glassbrenner, C. J., and Slack, Glen A. Thermal conductivity of silicon and germanium from 3 K to the melting point. *Phys. Rev. 134*, 4A (1964), A1058–A1069.

[62] Glaudell, Anne M., Cochran, Justin E., Patel, Shrayesh N., and Chabinyc, Michael L. Impact of the doping method on conductivity and thermopower in semiconducting polythiophenes. *Adv. Energy Mater. 5*, 4 (2015), 1401072.

[63] Goodnick, S. M., Ferry, D. K., Wilmsen, C. W., Liliental, Z., Fathy, D., and Krivanek, O. L. Surface roughness at the Si(100)-$Si0_2$ interface. *Phys. Rev. B 32*, 12 (1985), 8171.

[64] Gregg, Brian A., Chen, Si-Guang, and Branz, Howard M. On the superlinear increase in conductivity with dopant concentration in excitonic semiconductors. *Appl. Phys. Lett. 84*, 10 (2004), 1707–1709.

[65] Groves, C., Marsh, R. A., and Greenham, N. C. Monte Carlo modeling of geminate recombination in polymer-polymer photovoltaic devices. *J. Chem. Phys. 129*, 11 (2008), 114903.

[66] He, Ming, Qiu, Feng, and Lin, Zhiqun. Towards high-performance polymer-based thermoelectric materials. *Energy Environ. Sci. 6* (2013), 1352–1361.

[67] Hicks, L.D., and Dresselhaus, M.S. Effect of quantum-well structures on the thermoelectric figure of merit. *Phys. Rev. B 47* (1993), 12727.

[68] Hicks, L.D., and Dresselhaus, M.S. Thermoelectric figure of merit of a one-dimensional conductor. *Phys. Rev. B 47* (1993), 16631.

[69] Hochbaum, A.I., Chen, R., Delgado, R.D., Liang, W., Garnett, E.C., Najarian, M., Majumdar, A., and Yang, P. Enhanced thermoelectric performance of rough silicon nanowires. *Nature 451* (2008), 163.

[70] Hori, Takuma, Shiomi, Junichiro, and Dames, Chris. Effective phonon mean free path in polycrystalline nanostructures. *Appl. Phys. Lett. 106*, 17 (2015), 171901.

[71] Hsiao, Tzu-Kan, Chang, Hsu-Kai, Liou, Sz-Chian, Chu, Ming-Wen, Lee, Si-Chen, and Chang, Chih-Wei. Observation of room-temperature ballistic thermal conduction persisting over 8.3 μm in SiGe nanowires. *Nat. Nanotechnol. 8*, 7 (2013), 534–538.

[72] Huxtable, Scott T., Abramson, Alexis R., Tien, Chang-Lin, Majumdar, Arun, LaBounty, Chris, Fan, Xiaofeng, Zeng, Gehong, Bowers, John E., Shakouri, Ali, and Croke, Edward T. Thermal conductivity of si/sige and sige/sige superlattices. *Appl. Phys. Lett. 80*, 10 (2002), 1737–1739.

[73] Hyldgaard, Per, and Mahan, G. D. Phonon superlattice transport. *Phys. Rev. B 56*, 17 (1997), 10754–10757.

[74] Ihnatsenka, S., Crispin, X., and Zozoulenko, I. V. Understanding hopping transport and thermoelectric properties of conducting polymers. *Phys. Rev. B 92* (2015), 035201.

[75] Jacobs, Ian E., D'Avino, Gabriele, Lin, Yue, Lemaur, Vincent, Huang, Yuxuan, Ren, Xinglong, Simatos, Dimitrios, Wood, William, Chen, Chen, Harrelson, Thomas, Mustafa, Tarig, O'Keefe, Christopher A., Spalek, Leszek, Tjhe, Dion, Statz, Martin, Lai, Lianglun, Finn, Peter A., Neal, William G., Strzalka, Joseph, Nielsen, Christian B., Lee, Jin-Kyun, Barlow, Stephen, Marder, Seth R., McCulloch, Iain, Fratini, Simone, Beljonne, David, and Sirringhaus,

Henning. Ion-exchange doped polymers at the degenerate limit: what limits conductivity at 100% doping efficiency? *arXiv:cond-mat.mtrl-sci* (2021), 2101.01714.

[76] Jeng, Ming-Shan, Yang, Ronggui, Song, David, and Chen, Gang. Modeling the thermal conductivity and phonon transport in nanoparticle composites using Monte Carlo simulation. *J. Heat Transf. 130* (2008), 042410.

[77] Jonson, M., and Mahan, G. D. Mott's formula for the thermopower and the Wiedemann-Franz law. *Phys. Rev. B 21*, 10 (1980), 4223–4229.

[78] Joshi, Giri, Lee, Hohyun, Lan, Yucheng, Wang, Xiaowei, Zhu, Gaohua, Wang, Dezhi, Gould, Ryan W., Cuff, Diana C., Tang, Ming Y., Dresselhaus, Mildred S., Chen, Gang, and Ren, Zhifeng. Enhanced thermoelectric figure-of-merit in nanostructured p-type silicon germanium bulk alloys. *Nano Lett. 8*, 12 (2008), 4670–4674.

[79] Jung, In Hwan, Hong, Cheon Taek, Lee, Un-Hak, Kang, Young Hun, Jang, Kwang-Suk, and Cho, Song Yun. High thermoelectric power factor of a diketopyrrolopyrrole-based low bandgap polymer via finely tuned doping engineering. *Sci. Rep. 7* (2017), 44704.

[80] Kaiser, A B. Electronic transport properties of conducting polymers and carbon nanotubes. *Rep. Prog. Phys. 64*, 1 (2000), 1–49.

[81] Kang, S. D., and Synder, G. J. Charge-transport model for conducting polymers. *Nature Mater. 16* (2017), 252–257.

[82] Kasuya, Naotaka, Imaizumi, Satoru, Lectard, Sylvain, Matsui, Hiroyuki, Watanabe, Shun, and Takeya, Jun. High carrier density, electrostatic doping in organic single crystal semiconductors using electret polymers. *Appl. Phys. Express 12*, 7 (2019), 071001.

[83] Kazan, M., and Volz, S. Calculation of the lattice thermal conductivity in granular crystals. *J. Appl. Phys. 115*, 7 (2014), 073509.

[84] Khatami, S. N., and Aksamija, Z. Lattice thermal conductivity of the binary and ternary group-IV alloys Si-Sn, Ge-Sn, and Si-Ge-Sn. *Phys. Rev. Appl. 6* (2016), 014015.

[85] Khitun, A., Balandin, A., Liu, J. L., and Wang, K. L. The effect of the long-range order in a quantum dot array on the in-plane lattice thermal conductivity. *Superlattices Microstruct 30*, 1 (2001), 1 – 8.

[86] Khitun, A., Balandin, A., and Wang, K. L. Modification of the lattice thermal conductivity in silicon quantum wires due to spatial confinement of acoustic phonons. *Superlatt. Microstruct. 26*, 3 (1999), 181.

[87] Kim, G-H., Shao, L., Zhang, K., and Pipe, K. P. Engineered doping of organic semiconductors for enhanced thermoelectric efficiency. *Nature Mater. 12* (2013), 719.

[88] Kim, Hyoungjoon, Kim, Ilsoo, jin Choi, Heon, and Kim, Woochul. Thermal conductivities of $Si_{1-x}Ge_x$ nanowires with different germanium concentrations and diameters. *Appl. Phys. Lett. 96* (2010), 233106.

[89] Kim, Hyun-Sik, Gibbs, Zachary M., Tang, Yinglu, Wang, Heng, and Snyder, G. Jeffrey. Characterization of Lorenz number with Seebeck coefficient measurement. *APL Mater. 3*, 4 (2015), 041506.

[90] Kirkpatrick, James, Marcon, Valentina, Nelson, Jenny, Kremer, Kurt, and Andrienko, Denis. Charge mobility of discotic mesophases: A multiscale quantum and classical study. *Phys. Rev. Lett. 98* (May 2007), 227402.

[91] Klemens, P. G. Thermal resistance due to point defects at high temperatures. *Phys. Rev. 119*, 2 (1960), 507–509.

[92] Klemens, P.G. *Solid state physics*. Academic Press, NY, 1958.

[93] Kukita, K., and Kamakura, Y. Monte Carlo simulation of phonon transport in silicon including a realistic dispersion relation. *J. Appl. Phys. 114*, 15 (2013), 154312.

[94] Lacroix, D., Joulain, K., Terris, D., and Lemonnier, D. Monte Carlo simulation of phonon confinement in silicon nanostructures: Application to the determination of the thermal conductivity of silicon nanowires. *Appl. Phys. Lett. 89*, 10 (2006), 103104.

[95] Lan, Yucheng, Minnich, Austin Jerome, Chen, Gang, and Ren, Zhifeng. Enhancement of thermoelectric Figure-of-Merit by a bulk nanostructuring approach. *Adv. Func. Mater. 20*, 3 (2010), 357–376.

[96] Lan, Yucheng, Poudel, Bed, Ma, Yi, Wang, Dezhi, Dresselhaus, Mildred S., Chen, Gang, and Ren, Zhifeng. Structure study of bulk nanograined thermoelectric bismuth antimony telluride. *Nano Lett. 9* (2009), 1419–1422.

[97] Larkin, Jason M., and McGaughey, Alan J. H. Predicting alloy vibrational mode properties using lattice dynamics calculations, molecular dynamics simulations, and the virtual crystal approximation. *J. Appl. Phys. 114*, 2 (2013), 023507.

[98] Lee, Eun Kyung, Yin, Liang, Lee, Yongjin, Lee, Jong Woon, Lee, Sang Jin, Lee, Junho, Cha, Seung Nam, Whang, Dongmok, Hwang, Gyeong S., Hippalgaonkar, Kedar, Majumdar, Arun, Yu, Choongho, Choi, Byoung Lyong, Kim, Jong Min, and Kim, Kinam. Large thermoelectric figure-of-merits from sige nanowires by simultaneously measuring electrical and thermal transport properties. *Nano Lett. 12* (2012), 2918–2923.

[99] Lee, Minjoo Larry, and Venkatasubramanian, Rama. Effect of nanodot areal density and period on thermal conductivity in SiGe/Si nanodot superlattices. *Appl. Phys. Lett. 92*, 5 (2008), 053112.

[100] Lee, S.-M., Cahill, David G., and Venkatasubramanian, Rama. Thermal conductivity of si–ge superlattices. *Appl. Phys. Lett. 70*, 22 (1997), 2957–2959.

[101] Lepri, Stefano, Livi, Roberto, and Politi, Antonio. Thermal conduction in classical low-dimensional lattices. *Phys. Reports 377*, 1 (2003), 1 – 80.

[102] Li, D., Wu, Y., Kim, P., Shi, L., Yang, P., and Majumdar, A. Thermal conductivity of individual silicon nanowires. *Appl. Phys. Lett. 83* (2003), 2934–2936.

[103] Li, Junjie, Tang, Xinfeng, Li, Han, Yan, Yonggao, and Zhang, Qingjie. Synthesis and thermoelectric properties of hydrochloric acid-doped polyaniline. *Synth. Met. 160*, 11–12 (2010), 1153 – 1158.

[104] Li, Wu, and Mingo, Natalio. Alloy enhanced anisotropy in the thermal conductivity of Si_xGe_{1x} nanowires. *J. Appl. Phys. 114*, 5 (2013), 054307.

[105] Li, Yunyun, Liu, Sha, Li, Nianbei, Hänggi, Peter, and Li, Baowen. 1d momentum-conserving systems: the conundrum of anomalous versus normal heat transport. *New J. Phys. 17*, 4 (2015), 043064.

[106] Liang, Zhiming, Zhang, Yadong, Souri, Maryam, Luo, Xuyi, Boehm, Alex M., Li, Ruipeng, Zhang, Yan, Wang, Tairan, Kim, Doo-Young, Mei, Jianguo, Marder, Seth R., and Graham, Kenneth R. Influence of dopant size and electron affinity on the electrical conductivity and thermoelectric properties of a series of conjugated polymers. *J. Mater. Chem. A 6* (2018), 16495–16505.

[107] Liao, C. N., Chen, C., and Tu, K. N. Thermoelectric characterization of si thin films in silicon-on-insulator wafers. *J. Appl. Phys. 86*, 6 (1999), 3204–3208.

[108] Liu, Jun, Wang, Xiaojia, Li, Dongyao, Coates, Nelson E., Segalman, Rachel A., and Cahill, David G. Thermal conductivity and elastic constants of PEDOT:PSS with high electrical conductivity. *Macromolecules 48*, 3 (2015), 585–591.

[109] Liu, Sha, Hänggi, Peter, Li, Nianbei, Ren, Jie, and Li, Baowen. Anomalous heat diffusion. *Phys. Rev. Lett. 112* (2014), 040601.

[110] Liu, Sha, Yuan, Jun, Deng, Wanyuan, Luo, Mei, Xie, Yuan, Liang, Quanbin, Zou, Yingping, He, Zhicai, Wu, Hongbin, and Cao, Yong. High-efficiency organic solar cells with low non-radiative recombination loss and low energetic disorder. *Nat. Photonics 14* (2020), 300–305.

[111] Liu, Weili, and Balandin, Alexander A. Thermal conduction in al$_x$ga$_{1-x}$n alloys and thin films. *J. Appl. Phys. 97*, 7 (2005), 073710.

[112] Liu, Weishu, Yan, Xiao, Chen, Gang, and Ren, Zhifeng. Recent advances in thermoelectric nanocomposites. *Nano Energy 1*, 1 (2012), 42 – 56.

[113] Liu, W.L., Borca-Tasciuc, T., Chen, G., Liu, J.L., and Wang, K.L. Anisotropic thermal conductivity of ge quantum-dot and symmetrically strained si/ge superlattices. *J. Nanosci. Nanotechnol. 1* (2001), 39–42(4).

[114] Liu, Xien, Jeong, Kwang S., Williams, Bryan P., Vakhshouri, Kiarash, Guo, Changhe, Han, Kuo, Gomez, Enrique D., Wang, Qing, and Asbury, John B. Tuning the dielectric properties of organic semiconductors via salt doping. *J. Phys. Chem. B 117*, 49 (2013), 15866–15874.

[115] (LLNL), Lawrence Livermore National Laboratory, and the U.S. Department of Energy. Energy flow charts. *¡https://flowcharts.llnl.gov/commodities/energy¿* (2019).

[116] Lodha, A., and Singh, R. Prospects of manufacturing organic semiconductor-based integrated circuits. *IEEE Trans. Semicond. Manuf. 14*, 3 (2001), 281–296.

[117] Lu, Nianduan, Li, Ling, Gao, Nan, and Liu, Ming. Understanding electrical-thermal transport characteristics of organic semiconductors: Violation of Wiedemann-Franz law. *J. Appl. Phys. 120*, 19 (2016), 195108.

[118] Lu, Nianduan, Li, Ling, and Liu, Ming. A review of carrier thermoelectric-transport theory in organic semiconductors. *Phys. Chem. Chem. Phys. 18* (2016), 19503–19525.

[119] MacKenzie, Roderick C. I., Frost, Jarvist M., and Nelson, Jenny. A numerical study of mobility in thin films of fullerene derivatives. *J. Chem. Phys. 132*, 6 (2010), 064904.

[120] Mahan, G D, and Sofo, J O. The best thermoelectric. *Proc. Natl. Acad. Sci. U. S. A. 93* (1996), 7436–7439.

[121] Mai, Trieu, Dhar, Abhishek, and Narayan, Onuttom. Equilibration and universal heat conduction in fermi-pasta-ulam chains. *Phys. Rev. Lett. 98* (2007), 184301.

[122] Majumdar, Arun. Thermoelectricity in semiconductor nanostructures. *Science 303*, 5659 (2004), 777–778.

[123] Marcus, R. A. Chemical and electrochemical electron-transfer theory. *Annu. Rev. Phys. Chem. 15*, 1 (1964), 155–196.

[124] Maris, Humphrey J. Phonon propagation with isotope scattering and spontaneous anharmonic decay. *Phys. Rev. B 41*, 14 (1990), 9736–9743.

[125] Martin, Pierre, Aksamija, Zlatan, Pop, Eric, and Ravaioli, Umberto. Impact of phonon-surface roughness scattering on thermal conductivity of thin si nanowires. *Phys. Rev. Lett. 102*, 12 (2009), 125503.

[126] Martín-González, Marisol, Caballero-Calero, O., and Díaz-Chao, P. Nanoengineering thermoelectrics for 21st century: Energy harvesting and other trends in the field. *Renew. Sustain. Energy Rev. 24* (2013), 288 – 305.

[127] Maurer, L. N., Aksamija, Z., Ramayya, E. B., Davoody, A. H., and Knezevic, I. Universal features of phonon transport in nanowires with correlated surface roughness. *Appl. Phys. Lett. 106*, 13 (2015), 133108.

[128] Maycock, P.D. Thermal conductivity of silicon, germanium, III–V compounds and III–V alloys. *Solid-State Electron. 10*, 3 (1967), 161–168.

[129] Mazumder, S., and Majumdar, A. Monte Carlo study of phonon transport in solid thin films including dispersion and polarization. *J. Heat Transf. 123*, 4 (2001), 749.

[130] McGaughey, Alan J. H., and Jain, Ankit. Nanostructure thermal conductivity prediction by Monte Carlo sampling of phonon free paths. *Appl. Phys. Lett. 100*, 6 (2012), 061911.

[131] Mei, S., Maurer, L. N., Aksamija, Z., and Knezevic, I. Full-dispersion Monte Carlo simulation of phonon transport in micron-sized graphene nanoribbons. *J. Appl. Phys. 116*, 16 (2014), 164307.

[132] Mendels, Dan, and Tessler, Nir. Thermoelectricity in disordered organic semiconductors under the premise of the Gaussian disorder model and its variants. *J. Phys. Chem. Lett. 5*, 18 (2014), 3247–3253.

[133] Mermilliod, N., Zuppiroli, L., and François, B. Thermal conductivity and specific heat of pure and iodine doped polyacetylene (CH)x. *J. Phys. France 41*, 12 (1980), 1453–1458.

[134] Miller, Allen, and Abrahams, Elihu. Impurity conduction at low concentrations. *Phys. Rev. 120* (Nov 1960), 745–755.

[135] Minnich, A. J., Lee, H., Wang, X. W., Joshi, G., Dresselhaus, M. S., Ren, Z. F., Chen, G., and Vashaee, D. Modeling study of thermoelectric SiGe nanocomposites. *Phys. Rev. B 80*, 15 (2009), 155327.

[136] Mityashin, Alexander, Olivier, Yoann, Van Regemorter, Tanguy, Rolin, Cedric, Verlaak, Stijn, Martinelli, Nicolas G., Beljonne, David, Cornil, Jérôme, Genoe, Jan, and Heremans, Paul. Unraveling the mechanism of molecular doping in organic semiconductors. *Adv. Mater. 24*, 12 (2012), 1535–1539.

[137] Mladenović, Marko, and Vukmirović, Nenad. Charge carrier localization and transport in organic semiconductors: Insights from atomistic multiscale simulations. *Adv. Func. Mater. 25*, 13 (2015), 1915–1932.

[138] Morelli, D. T., Heremans, J. P., and Slack, G. A. Estimation of the isotope effect on the lattice thermal conductivity of group IV and group III-V semiconductors. *Phys. Rev. B 66*, 19 (2002), 195304.

[139] Niu, Jiebin, Lu, Nianduan, Li, Ling, and Liu, Ming. Polaron effect dependence of thermopower in organic semiconductors. *Phys. Lett. A 378*, 48 (2014), 3579–3581.

[140] Novikov, S. V., Dunlap, D. H., Kenkre, V. M., Parris, P. E., and Vannikov, A. V. Essential role of correlations in governing charge transport in disordered organic materials. *Phys. Rev. Lett. 81* (1998), 4472–4475.

[141] Pasveer, W. F., Cottaar, J., Tanase, C., Coehoorn, R., Bobbert, P. A., Blom, P. W. M., de Leeuw, D. M., and Michels, M. A. J. Unified description of charge-carrier mobilities in disordered semiconducting polymers. *Phys. Rev. Lett. 94* (May 2005), 206601.

[142] Pautmeier, L, Richert, R, and Bässler, H. Poole-frenkel behavior of charge transport in organic solids with off-diagonal disorder studied by Monte Carlo simulation. *Synth. Met. 37*, 1 (1990), 271 – 281.

[143] Péraud, Jean-Philippe M., and Hadjiconstantinou, Nicolas G. Efficient simulation of multidimensional phonon transport using energy-based variance-reduced Monte Carlo formulations. *Phys. Rev. B 84* (2011), 205331.

[144] Pop, E. Energy dissipation and transport in nanoscale devices. *Nano Res. 3*, 3 (2010), 147–169.

[145] Press, William H., Teukolsky, Saul A., Vetterling, William T., and Flannery, Brian P. *Numerical Recipes in C (2Nd Ed.): The Art of Scientific Computing*. Cambridge University Press, New York, NY, USA, 1992.

[146] Priolo, A., Jaeger, H. M., Dammers, A. J., and Radelaar, S. Conductance of two-dimensional disordered Voronoi networks. *Phys. Rev. B 46*, 22 (1992), 14889–14892.

[147] Rajput, B. D., and Browne, D. A. Lattice dynamics of ii-vi materials using the adiabatic bond-charge model. *Phys. Rev. B 53*, 14 (1996), 9052–9058.

[148] Ramayya, E. B., Maurer, L. N., Davoody, A. H., and Knezevic, I. Thermoelectric properties of ultrathin silicon nanowires. *Phys. Rev. B 86* (2012), 115328.

[149] Randrianalisoa, J., and Baillis, D/. Monte Carlo simulation of steady–state microscale phonon heat transport. *J. Heat Transf. 130* (2008), 072404.

[150] Rehwald, Walther, and Kiess, Helmut G. Charge transport in polymers. In *Conjugated Conducting Polymers*, Helmut G. Kiess, Ed., vol. 102. Springer Berlin Heidelberg, 1992, pp. 135–173.

[151] Rieger, Martin M., and Vogl, P. Electronic-band parameters in strained $si_{1-x}ge_x$ alloys on $si_{1-y}ge_y$ substrates. *Phys. Rev. B 48*, 19 (1993), 14276–14287.

[152] Roenko, A. A., Lukin, V. V., Djurović, I., and Simeunović, M. Estimation of parameters for generalized Gaussian distribution. In *2014 6th International Symposium on Communications, Control and Signal Processing (ISCCSP), Athens, Greece*. 2014, pp. 376–379.

[153] Rogers, John A., Bao, Zhenan, Makhija, Anita, and Braun, Paul. Printing process suitable for reel-to-reel production of high-performance organic transistors and circuits. *Adv. Mater. 11*, 9 (1999), 741–745.

[154] Rubel, O., Baranovskii, S. D., Thomas, P., and Yamasaki, S. Concentration dependence of the hopping mobility in disordered organic solids. *Phys. Rev. B 69* (Jan 2004), 014206.

[155] Rustagi, K. C., and Weber, W. Adiabatic bond charge model for the phonons in A^3B^5 semiconductors. *Solid State Commun. 18*, 6 (1976), 673 – 675.

[156] Ryu, H. J., Aksamija, Z., Paskiewicz, D. M., Scott, S. A., Lagally, M. G., Knezevic, I., and Eriksson, M. A. Quantitative determination of contributions to the thermoelectric power factor in si nanostructures. *Phys. Rev. Lett. 105* (2010), 256601.

[157] Saito, Keiji, and Dhar, Abhishek. Heat conduction in a three dimensional anharmonic crystal. *Phys. Rev. Lett. 104* (2010), 040601.

[158] Schwarze, Martin, Gaul, Christopher, Scholz, Reinhard, Bussolotti, Fabio, Hofacker, Andreas, Schellhammer, Karl Sebastian, Nell, Bernhard, Naab, Benjamin D., Bao, Zhenan, Spoltore, Donato, Vandewal, Koen, Widmer, Johannes, Kera, Satoshi, Ueno, Nobuo, Ortmann, Frank, and Leo, Karl. Molecular parameters responsible for thermally activated transport in doped organic semiconductors. *Nat. Mater. 18*, 1476-4660 (2019), 242–248.

[159] Sellan, D. P., Turney, J. E., McGaughey, A. J. H., and Amon, C. H. Cross-plane phonon transport in thin films. *J. Appl. Phys. 108*, 11 (2010), 113524.

[160] Shamsa, Manu, Liu, Weili, Balandin, Alexander A., and Liu, Jianlin. Phonon-hopping thermal conduction in quantum dot superlattices. *Applied Physics Letters 87*, 20 (2005), 202105.

[161] Shi, Lihong, Yao, Donglai, Zhang, Gang, and Li, Baowen. Size dependent thermoelectric properties of silicon nanowires. *Appl. Phys. Lett. 95*, 6 (2009), 063102.

[162] Shi, X., and Sun, J. Dependence of seebeck coefficient on the density of states in organic semiconductors. *IEEE Electron Device Lett. 38*, 12 (2017), 1728–1731.

[163] Shlesinger, Michael F., Zaslavsky, George M., and Klafter, Joseph. Strange kinetics. *Nature 363* (1993), 31–37.

[164] Simkin, M. V., and Mahan, G. D. Minimum thermal conductivity of superlattices. *Phys. Rev. Lett. 84*, 5 (2000), 927–930.

[165] Slack, G. *Solid State Physics, vol. 34*. Academic Press, New York, NY, 1979.

[166] Snyder, G. Jeffrey, and Toberer, Eric S. Complex thermoelectric materials. *Nature Mater. 7* (2008), 105–114.

[167] Soffer, Stephen B. Statistical model for the size effect in electrical conduction. *J. Appl. Phys. 38*, 4 (1967), 1710–1715.

[168] Sommerfeld, A. Zur elektronentheorie der metalle. *Naturwissenschaften 15*, 41 (Oct 1927), 825–832.

[169] Strauch, D., and Dorner, B. Phonon dispersion in GaAs. *J. Phys.: Condens. Matter 2* (1990), 1457–1474.

[170] Sun, J., Yeh, M. L., Jung, B. J., Zhang, B., Feser, J., Majumdar, A., and Katz, H. E. Simultaneous increase in seebeck coefficient and conductivity in a doped poly(alkylthiophene) blend with defined density of states. *Macromolecules 43*, 6 (2010), 2897–2903.

[171] Tamura, Shin-Ichiro. Isotope scattering of dispersive phonons in Ge. *Phys. Rev. B 27*, 2 (1983), 858–866.

[172] Tessler, Nir, Preezant, Yevgeni, Rappaport, Noam, and Roichman, Yohai. Charge transport in disordered organic materials and its relevance to thin-film devices: A tutorial review. *Adv. Mater. 21*, 27 (7 2009), 2741–2761.

[173] Thesberg, Mischa, Kosina, Hans, and Neophytou, Neophytos. On the Lorenz number of multiband materials. *Phys. Rev. B 95* (2017), 125206.

[174] Thomas, Elayne M., Peterson, Kelly A., Balzer, Alex H., Rawlings, Dakota, Stingelin, Natalie, Segalman, Rachel A., and Chabinyc, Michael L. Effects of counter-ion size on delocalization of carriers and stability of doped semiconducting polymers. *Advanced Electronic Materials 6*, 12 (2020), 2000595.

[175] Thumfart, L, Carrete, J, Vermeersch, B, Ye, N, Truglas, T, Feser, J, Groiss, H, Mingo, N, and Rastelli, A. Thermal transport through Ge-rich Ge/Si superlattices grown on Ge(0 0 1). *J. Phys. D: Appl. Phys. 51*, 1 (2018), 014001.

[176] Tian, Zhiting et al. On the importance of optical phonons to thermal conductivity in nanostructures. *Appl. Phys. Lett. 99* (2011).

[177] Tietze, Max L., Benduhn, Johannes, Pahner, Paul, Nell, Bernhard, Schwarze, Martin, Kleemann, Hans, Krammer, Markus, Zojer, Karin, Vandewal, Koen, and Leo, Karl. Elementary steps in electrical doping of organic semiconductors. *Nat. Commun. 9* (2018), 1182.

[178] Tonga, Murat, Wei, Lang, Taylor, Patrick S., Wilusz, Eugene, Korugic-Karasz, Ljiljana, Karasz, Frank E., and Lahti, Paul M. Thermoelectric enhancement by compositing carbon nanotubes into iodine-doped poly[2-methoxy-5-(2-ethylhexyloxy)-1,4-phenylenevinylene]. *ACS Appl. Mater. & Inter. 9*, 10 (2017), 8975–8984.

[179] Torabi, Solmaz, Jahani, Fatemeh, Van Severen, Ineke, Kanimozhi, Catherine, Patil, Satish, Havenith, Remco W. A., Chiechi, Ryan C., Lutsen, Laurence, Vanderzande, Dirk J. M., Cleij, Thomas J., Hummelen, Jan C., and Koster, L. Jan Anton. Strategy for enhancing the dielectric constant of organic semiconductors without sacrificing charge carrier mobility and solubility. *Adv. Funct. Mater. 25*, 1 (2015), 150–157.

[180] Turney, J. E., McGaughey, A. J. H., and Amon, C. H. In-plane phonon transport in thin films. *J. Appl. Phys. 107*, 2 (2010), 024317.

[181] Upadhyaya, M., and Aksamija, Z. Nondiffusive lattice thermal transport in Si-Ge alloy nanowires. *Phys. Rev. B 94* (2016), 174303.

[182] Upadhyaya, Meenakshi, and Aksamija, Zlatan. Thermal conductivity of semiconductor nanostructures and alloys. In *Handbook of Materials Modeling, 2nd Ed., Applications: Current and Emerging Materials*, Davide Donadio, Ed., vol. 2. Springer, 2018.

[183] Upadhyaya, Meenakshi, Boyle, Connor, Venkataraman, Dhandapani, and Aksamija, Zlatan. Effects of disorder on thermoelectric properties of semiconducting polymers. *Sci. Rep. 9*, 2045-2322 (2019), 5820.

[184] Upadhyaya, Meenakshi, Khatami, Seyedeh Nazanin, and Aksamija, Zlatan. Engineering thermal transport in SiGe-based nanostructures for thermoelectric applications. *J. Mater. Res. 30* (2015), 2649–2662.

[185] Van Der Holst, Jeroen Johannes Maria. Three-dimensional modeling of charge transport, injection and recombination in organic light-emitting diodes. *Thesis// Dissertation ETD* (2010).

[186] Venkatasubramanian, R., Siivola, E., Colpitts, T., and O'Quinn, B. Thin-film thermoelectric devices with high room-temperature figures of merit. *Nature 413* (2001), 597.

[187] Vermeersch, Bjorn, Carrete, Jesús, and Mingo, Natalio. Cross-plane heat conduction in thin films with ab-initio phonon dispersions and scattering rates. *Appl. Phys. Lett. 108*, 19 (2016), 193104.

[188] Vermeersch, Bjorn, Carrete, Jesús, Mingo, Natalio, and Shakouri, Ali. Superdiffusive heat conduction in semiconductor alloys. i. theoretical foundations. *Phys. Rev. B 91* (2015), 085202.

[189] Vining, Cronin B. A model for the high-temperature transport properties of heavily doped n-type silicon-germanium alloys. *J. Appl. Phys. 69* (1991), 331–341.

[190] Vining, Cronin B. An inconvenient truth about thermoelectrics. *Nat. Mater. 8*, 2 (2009), 83–85.

[191] Vukmirović, Nenad, and Wang, Lin-Wang. Charge carrier motion in disordered conjugated polymers: A multiscale ab initio study. *Nano Letters 9*, 12 (2009), 3996–4000.

[192] Wang, Chunlai, Zhang, Zhongbo, Pejić, Sandra, Li, Ruipeng, Fukuto, Masafumi, Zhu, Lei, and Sauvé, Geneviève. High dielectric constant semiconducting poly(3-alkylthiophene)s from side chain modification with polar sulfinyl and sulfonyl groups. *Macromolecules 51*, 22 (2018), 9368–9381.

[193] Wang, X. W., Lee, H., Lan, Y. C., Zhu, G. H., Joshi, G., Wang, D. Z., Yang, J., Muto, A. J., Tang, M. Y., Klatsky, J., Song, S., Dresselhaus, M. S., Chen, G., and Ren, Z. F. Enhanced thermoelectric figure of merit in nanostructured n-type silicon germanium bulk alloy. *Appl. Phys. Lett. 93*, 19 (2008), 193121.

[194] Wang, Xufeng, Askarpour, Vahid, Maassen, Jesse, and Lundstrom, Mark. On the calculation of Lorenz numbers for complex thermoelectric materials. *J. Appl. Phys. 123*, 5 (2018), 055104.

[195] Wang, Zhao, and Mingo, Natalio. Diameter dependence of sige nanowire thermal conductivity. *Appl. Phys. Lett. 97*, 10 (2010), 101903.

[196] Wang, Zhao, and Mingo, Natalio. Absence of casimir regime in two-dimensional nanoribbon phonon conduction. *Appl. Phys. Lett. 99*, 10 (2011), 101903.

[197] Wang, Zhaojie, Alaniz, Joseph E., Jang, Wanyoung, Garay, Javier E., and Dames, Chris. Thermal conductivity of nanocrystalline silicon: Importance of grain size and frequency-dependent mean free paths. *Nano Lett. 11*, 6 (2011), 2206–2213.

[198] Ward, A., and Broido, D. A. Intrinsic phonon relaxation times from first-principles studies of the thermal conductivities of Si and Ge. *Phys. Rev. B 81*, 8 (2010), 085205.

[199] Weathers, Annie, Khan, Zia Ullah, Brooke, Robert, Evans, Drew, Pettes, Michael T., Andreasen, Jens Wenzel, Crispin, Xavier, and Shi, Li. Significant electronic thermal transport in the conducting polymer poly(3,4-ethylenedioxythiophene). *Adv. Mater. 27*, 12 (2015), 2101–2106.

[200] Weber, W. New bond-charge model for the lattice dynamics of diamond-type semiconductors. *Phys. Rev. Lett. 33*, 6 (1974), 371–373.

[201] Weber, W. Adiabatic bond charge model for the phonons in diamond, si, ge, and a-sn. *Phys. Rev. B 15*, 10 (1977), 4789.

[202] Weber, W. Adiabatic bond charge model for the phonons in diamond, Si, Ge, and α-Sn. *Phys. Rev. B 15* (1977), 4789–4803.

[203] Wu, Jiunn-Jong. Simulation of rough surfaces with FFT. *Tribology International 33*, 1 (2000), 47 – 58.

[204] Xie, Guofeng, Guo, Yuan, Li, Baohua, Yang, Liwen, Zhang, Kaiwang, Tang, Minghua, and Zhang, Gang. Phonon surface scattering controlled length dependence of thermal conductivity of silicon nanowires. *Phys. Chem. Chem. Phys. 15* (2013), 14647–14652.

[205] Xie, Guofeng, Guo, Yuan, Wei, Xiaolin, Zhang, Kaiwang, Sun, Lizhong, Zhong, Jianxin, Zhang, Gang, and Zhang, Yong-Wei. Phonon mean free path spectrum and thermal conductivity for $Si_{1-x}Ge_x$ nanowires. *Appl. Phys. Lett. 104*, 23 (2014), 233901.

[206] Xuan, Y., Liu, X., Desbief, S., Leclère, P., Fahlman, M., Lazzaroni, R., Berggren, M., Cornil, J., Emin, D., and Crispin, X. Thermoelectric properties of conducting polymers: The case of poly(3-hexylthiophene). *Phys. Rev. B 82* (2010), 115454.

[207] Yang, Bao, and Chen, Gang. Lattice dynamics study of anisotropic heat conduction in superlattices. *Microscale Thermophysical Engineering 5*, 2 (2001), 107 – 116.

[208] Yang, Nuo, Zhang, Gang, and Li, Baowen. Violation of fourier's law and anomalous heat diffusion in silicon nanowires. *Nano Today 5* (2010), 85–90.

[209] Yin, Liang, Kyung Lee, Eun, Woon Lee, Jong, Whang, Dongmok, Lyong Choi, Byoung, and Yu, Choongho. The influence of phonon scatterings on the thermal conductivity of sige nanowires. *Appl. Phys. Lett. 101*, 4 (2012), 043114.

[210] Yoo, Seung-Jun, and Kim, Jang-Joo. Charge transport in electrically doped amorphous organic semiconductors. *Macromol. Rapid Commun. 36*, 11 (2015), 984–1000.

[211] Yu, Choongho, Choi, Kyungwho, Yin, Liang, and Grunlan, Jaime C. Lightweight flexible carbon nanotube based organic composites with large thermoelectric power factors. *ACS Nano 5*, 10 (2011), 7885–7892.

[212] Zaburdaev, V., Denisov, S., and Klafter, J. Lévy walks. *Rev. Mod. Phys. 87* (2015), 483–530.

[213] Zebarjadi, Mona, Esfarjani, Keivan, Bian, Zhixi, and Shakouri, Ali. Low-temperature thermoelectric power factor enhancement by controlling nanoparticle size distribution. *Nano Lett. 11* (2011), 225–230.

[214] Zhu, G. H., Lee, H., Lan, Y. C., Wang, X. W., Joshi, G., Wang, D. Z., Yang, J., Vashaee, D., Guilbert, H., Pillitteri, A., Dresselhaus, M. S., Chen, G., and Ren, Z. F. Increased phonon scattering by nanograins and point defects in nanostructured silicon with a low concentration of germanium. *Phys. Rev. Lett. 102*, 19 (2009), 196803.

[215] Zuo, Guangzheng, Abdalla, Hassan, and Kemerink, Martijn. Impact of doping on the density of states and the mobility in organic semiconductors. *Phys. Rev. B 93* (2016), 235203.

[216] Zuzok, R., Kaiser, A. B., Pukacki, W., and Roth, S. Thermoelectric power and conductivity of iodine doped new polyacetylene. *J. Chem. Phys. 95*, 2 (1991), 1270–1275.

[217] Zvyagin, I. P. Quantum-statistical theory of transport by localized carriers in disordered semiconductors. *phys. stat. sol. (b) 101* (1980), 9–42.